VISER
www.viserdata.com

RESEARCH AND APPLICATION OF MATERIALS SCIENCE

ISSN:2661-4464(online) 2661-4456(print)
Volume 1 No. 1 2019

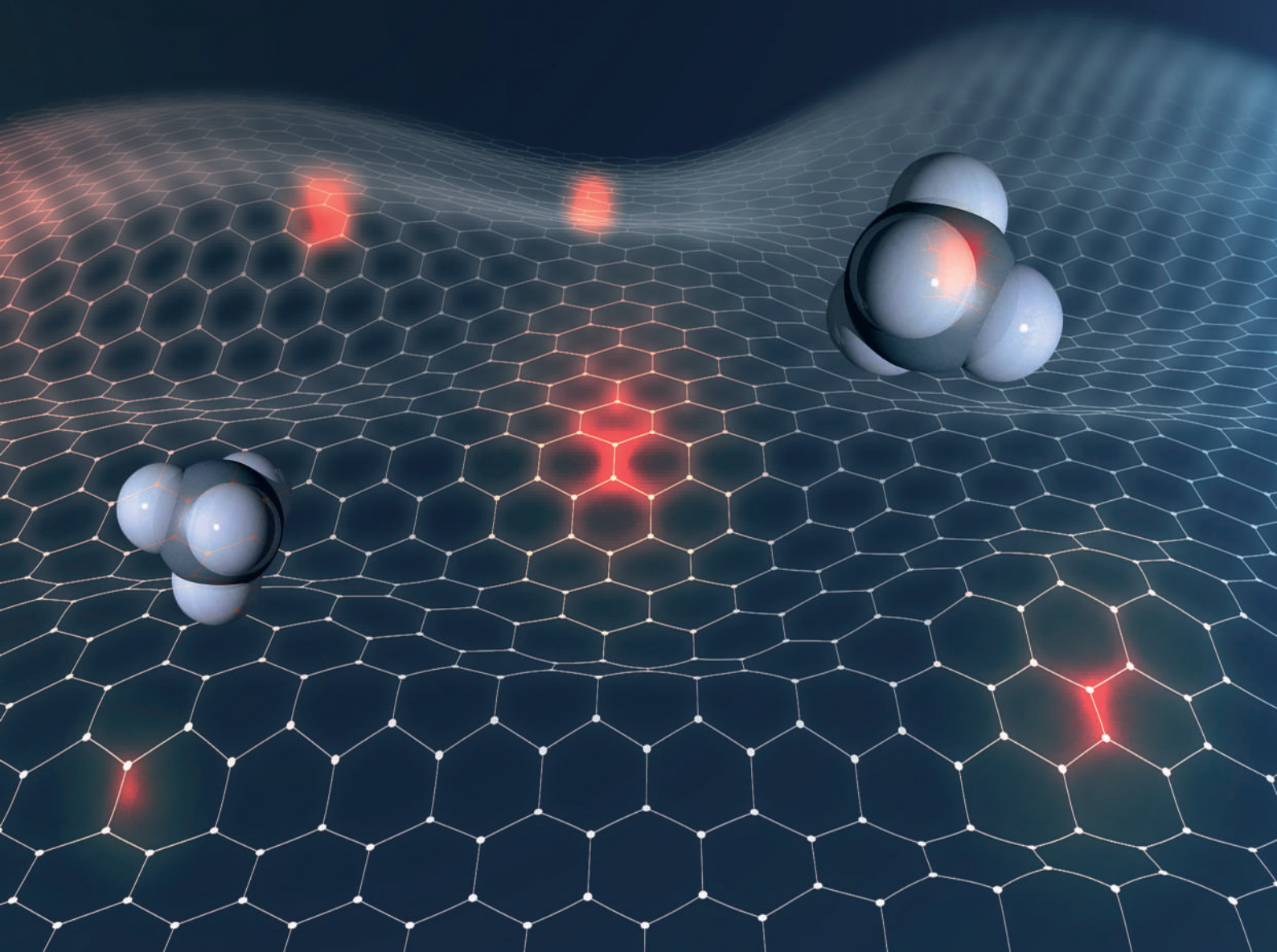

COMPANY INTRODUCTION

公司简介

维泽科技文化有限公司(Viser Technology Pte. Ltd.)成立于新加坡，是一家科技与文化高度融合的创新型企业。我们拥有一支具有较高文化素质、管理素质和业务素质的团队，聚焦于国际开源中英文期刊、体现文化含量与学术价值图书的出版发行。秉承“传播科技文化，促进学术交流”的理念，与国内外知名院校，科研院所及数据库建立了稳定的合作关系。坚持开拓创新，实施“跨越-融合”的发展战略，立足中国、新加坡两地，辐射全球，并于中国设立河北和重庆两个分部。我们将紧紧围绕专业化、特色化的发展道路，不断营造“有情怀，有视野，有梦想”的企业文化氛围，独树一帜，做一家“有血、有肉、有温度”的创新型出版企业。

Viser Technology Pte. Ltd. was founded in Singapore with branch offices in both Hebei and Chongqing, China. Viser focuses on publishing scientific and technological journals and books that promote the exchange of scientific and technological findings among the research community and around the globe. Despite being a young company, Viser is actively connecting with well-known universities, research institutes, and indexation database, and has already established a stable collaborative relationship with them. We also have a group of experienced editors and publishing experts who are dedicated to publishing high-quality journal and book contents. We offer the scholars various academic journals covering a variety of subjects and we are committed to reducing the hassles of scholarly publishing. To achieve this goal, we provide scholars with an all-in-one platform that offers solutions to every publishing process that a scholar needs to go through in order to show their latest finding to the world.

Research and Application of Materials Science

Publisher: Viser Technology Pte. Ltd.

ISSN: 2661-4464(online)
2661-4456(print)

Frequency: Semi-annual

Add.:21 Woodlands Close, #08-18,
Primz Bizhub SINGAPORE (737854)

https://www.viserdata.com/

Research and Application of Materials Science

Volume 1 No.1 (2019)

CONTENTS

VISER

Viser Technology Pte. Ltd.
Research and Application of Materials Science
https://doi.org/10.33142/msra.v1i1.665

Research Article Open Access

The Feasibility of Basalt Rock Powder and Superfine Sand as Partial Replacement Materials for Portland Cement and Artificial Sand in Cement Mortar

Hongxia Qiao[1], Desire Ndahirwa[2], Yuanke Li[3], Jinke Liang[4]

[1] Professor, Department of Construction Materials, School of Civil Engineering, Lanzhou University of Technology, Key Laboratory of Disaster Prevention and Mitigation in Civil Engineering of Gansu Province, Lanzhou 730050, China
[2] Postgraduate Student, Department of Structural Engineering, School of Civil Engineering, Lanzhou University of Technology, Lanzhou 730050, China
[3] Postgraduate Student, Department of Construction Materials, School of Civil Engineering, Lanzhou University of Technology, Lanzhou 730050, China
[4] Postgraduate Student, Department of Construction Materials, School of Civil Engineering, Lanzhou University of Technology, Lanzhou 730050, China

***Corresponding Author:** Hongxia Qiao, Lanzhou University of Technology, Lanzhou, China and Postcode: 730050, E-mail: qhxlut7706@163.com*

Abstract:
The research gap on the feasibility of basalt rock powder (BRP) and superfine sand (SS) in preparation of cement mortar is significant. This study examines probable changes occurred in the modified cement mortar due to incorporation of certain quantity of basalt rock powder and superfine sand in mixture proportion. The cement mortar included Portland cement, artificial sand and water as principal mixture constituents. Then, basalt rock powder and superfine sand were added as partial replacement materials for Portland cement and artificial sand respectively. Therefore, replacement percentages were 10%, 15%, 20%, 25% and 30% when the basalt rock powder replaced Portland cement and in case the artificial sand was replaced by superfine sand, 10%, 20%, 30%, 40% and 50%. Then, the strength indexes such as flexural strength, compressive strength, ultrasonic pulse velocity and dynamic elastic modulus were investigated. The results show that the presence of basalt rock powder in mixture proportion increased the flexural and compressive strengths of cement mortar however the cement mortar that contained superfine sand illustrated inadequate mechanical performance as flexural and compressive strengths decreased remarkably. Moreover, when basalt rock powder and superfine sand were included together in mixture proportion, the cement mortar's mechanical performance declined compared to that of the reference cement mortar. Despite the fact that basalt rock powder and superfine sand weakened the cement mortar's mechanical properties, it was found that they can be added into the cement mortar as partial replacement of Portland cement and artificial sand in the following ratios: from 10% to 25% when basalt rock powder replaces Portland cement and from 10% to 20% when artificial sand is replaced by superfine sand.

Keywords: *basalt rock powder, superfine sand, artificial sand, cement mortar, mechanical properties*

Citation: H.X. Qiao, et al., The Feasibility of Basalt Rock Powder and Superfine Sand as Partial Replacement Materials for Portland Cement and Artificial Sand in Cement Mortar. *Res Appl Mat Sci*, 2019,1(1): 1-9. https://doi.org/10.33142/msra.v1i1.665

1. Introduction

The application of basalt rock powder (BRP) and superfine sand (SS) in preparation of cement mortar remains a recent innovation in construction materials production industry. It is well known that the production of cement mortar requires enormous amount of cement and medium sand. However, essential mineral admixture resources for concrete and cement mortar production have been reported insufficient as construction demand has promptly increased in recent years. In addition, the rise of cement production and consumption in diverse construction projects has been blamed to be among anticipating causes to the environmental pollution and global drastic climate change. Hence, this study emphasizes on modifying the cement mortar mixture proportion by adding basalt rock powder as Portland cement partial replacement and superfine sand as artificial sand partial replacement.

Even though basalt rock powder and superfine sand appeal to offer a limited range of applications in construction, they can anticipate in promotion cementitious composites sustainability development. Countless studies have discussed the significance of basalt rock powder, superfine sand and other recently discovered mineral admixtures on the development and improvement of physical, chemical and mechanical properties of cement mortar and concrete. Yet, the shortage in findings related to the implementation of basalt rock powder and superfine sand in civil engineering materials production remains significant. The inclusion of basalt rock powder and superfine sand in cement mortar preparation as partial replacements of Portland cement and fine aggregate respectively, is considered to be an effective approach to diminish environmental concerns that initiated by their abundant unexploited disposals in the environment. Moreover, this strategy would as well reduce the magnitude of carbon dioxide emissions in the atmosphere generated by the cement manufacturing industry.

According to (Dobiszewska and Beycioğlu, 2017; Singh et al., 2017) primary motives for the increasing consumption of Portland cement include industrial revolution, recent technology development, rapid population growth and increase of living standards. The technological process of clinkerization which is common in modern cement production is responsible for a great consumption of energy and the emission of carbon dioxide to the environment. It has been reported that around 0.7-1 tonne of CO_2 is released for every tonne of cement production (Carvalho et al., 2018). Moreover, the production of a tonne of cement requires 60-130 kg of fuel oil or its equivalent and about 105 kWh of electricity depending on the cement type and production process (Tchamdjou et al., 2017).

The topic related to sustainability and durability of cementitious structures has attracted the scientific community. Many researchers and academicians have turned their efforts towards encouraging usage of construction wastes and industrial by-products as additives or substitute for cement and fine aggregate in concrete mixtures (Liu et al., 2013; Mehdipour and Kamal, 2018; Khandaker, 2003; Kannan et al., 2017). In fact, several discovered alternative mineral admixtures have a great importance in improvement of the mechanical behavior of cementitious composites and reduction of environmental pollution. In addition, the mortars made by including alternative mineral admixtures illustrate benefits such as low cost, diminution of permeability, improvement of strength or other properties of cement mortar and concrete. (Naceri and Makhloufi, 2009; Uysal and Yilmaz, 2011; Liu et al., 2013; Topcu et al., 2009; Shyam et al., 2017). Eventually, (Hafsa and Mishra, 2016) considered basalt rock powder as a relevant partial replacement of Portland cement thanks to exceptional structural properties that basalt rock presents.

According to (Pu et al., 1999) in southwest China precisely Chongqing the exploitation of superfine sand started as early as in the 1950's. (Lian and Chen, 1996; Wu and Lian, 1999) stated that the scarcity in raw materials resulted from decades of excessive excavation for the search for resources of coarse aggregates and medial sand. Therefore, (Zhao, 2013) reported that China is amongst countries that have been greatly affected by shortage in natural fine aggregate supply. For instance, in areas like Chongqing, Henan, Sichuan, Shandong and other places coarse and medium aggregates resources are rarely found but SS supply is available in abundance. SS unlike BRP has been used for construction purposes for many years. Traditionally, SS is used as plastering mortar component and it is also involved in brick and block works. The shortage in fine sand supply suitable for cement mortar and concrete production has pushed researchers to establish innovative solutions. (He et al., 2012) attempted to use SS in the mixture proportion as medium sand replacement and the findings illustrated that the modified cement mortar exhibited inferior mechanical performance. According to (Tu et al., 2012) in superfine sand concrete the increase of sand ratio implicates decrease of slumps and strength. Hence, SS has great effect on the concrete workability, especially on the concrete fluidity. Moreover, SS concrete illustrates a good frost resistance and impermeability.

When basalt rock powder is added into cement mortar to replace a portion of Portland cement, such addition illustrated a significant influence on the cement mortar's mechanical properties as it improves the flexural and compressive strengths of the produced cement mortar. Previous research works with regard to implementation of BRP in cement mortar or concrete preparation insisted that it improves rheological properties and workability of the cement mortar. It also accelerates the development of early age strength of mortars and the presence of BRP into cement paste decreases the yield stress and viscosity (Kmecová et al. 2014; Schankoski et al., 2017). Moreover, basalt waste added into the cement mortar mixture proportion enhances the resulted mortar's compressive strength. And also when basalt waste is used as a replacement of clinker in production of cement, it was reported that it reduces the CO_2 emission. In addition, hydration products observed on surface of BRP particles show the nucleation effect of mineral mixtures (Mendes et al., 2016). The superfine sand due to its small fineness modulus, large surface area and porosity, it increases cement, water, moisture and slurry content of concrete.

This study opts to investigate modifications occurred in mechanical performance of the cement mortar due to incorporation of basalt rock powder and superfine sand into the mixture proportions. The reference cement mortar consisted of Portland cement, water and artificial sand. However, the evaluated cement mortar included Portland cement, artificial sand, basalt rock powder, superfine sand and water. The basalt rock powder has been added in proportion of 10%, 15%, 20%, 25% and 30% by Portland cement weight and superfine sand 10%, 20%, 30%, 40% and 50% of artificial sand weight. To evaluate the effect of BRP and SS on the mechanical performance of the cement mortar, several mixture proportions were designed and assessed through experimental procedure. Then, based on the strength indexes such as flexural strength, compressive strength, ultrasonic pulse velocity and dynamic elastic modulus, the replacement ratios of BRP and SS that exhibited nearly similar results as those of the reference cement mortar were selected.

2. Experimental study

2.1 Raw materials

Cement: Qilian Mountains brand Portland cement with strength grade 42.5 was supplied by Gansu Cement Factory Ltd. According to the cement manufacturer, it had a Blaine fineness of 400 kg/m^2.

Table 2.1 Portland cement performance index

Stability	Specific surface area m_2/kg	Condensation time (min)		Flexural strength (MPa)		Comprehensive strength (MPa)	
		Initial setting	Final setting	3d	28d	3d	28d
Qualified	348	145	220	5.5	7.6	21.6	48.7

Table 2.2 Chemical composition of Portland cement

Portland cement components	SiO_2	Fe_2O_3	Al_2O_3	CaO	MgO	SO_3	Loss on ignition
Specification value %	-	-	-	-	≤ 5.0	≤ 3.5	≤ 3.0
Measured value %	30.54	3.78	4.16	54.25	1.43	2.83	1.67

Superfine sand: The superfine sand used in the experiment, was collected from yellow river beds in Lanzhou. We purchased the superfine sand from a local sand supplier company. The fineness modulus ranges from 0.6 to 1.18.

Table 2.3 Sieve analysis of superfine sand

Sieve size (mm)	Mass percentage of retained (%)	Cumulative mass percentage of retained (%)
4.75	-	-
2.36	-	-
1.18	0.37	0.37
0.6	15.04	15.41
0.3	28.9	44.31
0.15	37.6	81.91
< 0.15	18.05	99.96

Basalt rock powder was produced from local natural basalt rocks in accordance to the Chinese National Standards. It was also like superfine sand purchased from a local sand supplier company. No preliminary tests were effectuated before its use.

Table 2.4 Basalt rock powder chemical components

Component	C	O	Al	Si	K	Ca	Fe
Mass ratio	29.07	42.89	4.82	10.97	0.72	4.24	3.68

Artificial sand: The artificial sand was obtained after crushing local natural rocks. The synthetic sand used in cement mortar mixture had 2.36 mm maximum aggregate size, was produced in Lanzhou, Gansu province.

Like previously described on superfine sand, we used divers sieve sizes to determine its fineness modulus before using it in preparation of the cement mortar mixture.

Table 2.5 Sieve analysis of artificial sand

Sieve size (mm)	Mass percentage of retained (%)	Cumulative mass percentage of retained (%)
4.75	-	-
2.36	10	10
1.18	20	30
0.6	24	54
0.3	38	92
0.15	6	98

Table 2.6 Artificial sand performance index

Mud content	Apparent density	Bulk density	Void ratio	Fineness modulus
%	kg/m_3	kg/m_3	%	
3	2620	1520	42	2.8

2.2 Mixture proportions

Table 2.7 Cement mortar mixture constituents

Cement mortar blocks	Cement (kg/m_3)	Basalt rock powder(kg/m_3)	Artificial sand (kg/m_3)	Water (kg/m_3)	Substitution (%)
C0	450	0	1350	225	0
C1	405	45	1350	225	10
C2	382.5	67.5	1350	225	15
C3	360	90	1350	225	20
C4	337.5	112.5	1350	225	25
C5	315	135	1350	225	30

Table 2.8 Cement mortar mixture proportions

Cement mortar blocks	Cement (kg/m3)	Artificial Sand (kg/m3)	Superfine Sand (kg/m3)	Water (kg/m3)	Substitution (%)
H0	450	1350	0	225	0
H1	450	1215	135	225	10
H2	450	1080	270	225	20
H3	450	945	405	225	30
H4	450	810	540	225	40
H5	450	675	675	225	50

Figure 2.1. Portland cement

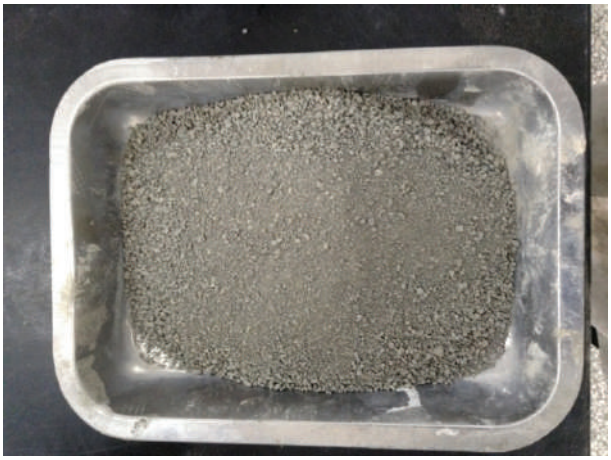

Figure 2.2. Artificial sand

Figure 2.3. Basalt rock powder

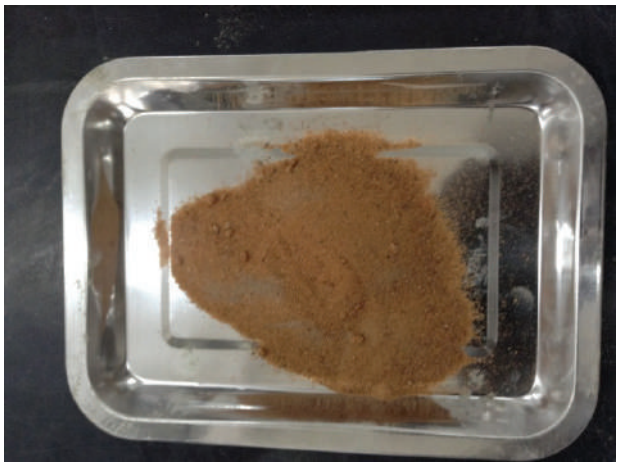

Figure 2.4. Superfine sand

2.3 Experimental program

According to "Cement mortar strength test method (ISO method)" GB/T17671-1999, 40 mm × 40 mm × 160 mm prism cement mortar test blocks were prepared. The experimental procedure proceeded with accurately weighting the amount of material required to prepare the test block according to the designed mixing ratio and then use the universal cement mixer to stir the materials used. During mixing, water was added cautiously. At first the water is put into the stirring pot, after the Portland cement was added, start stirring, then stir at low speed for 30s, and at the same time start the second 30s, and evenly the fine aggregate was added. Immediately after the mixture was obtained, it was molded on a vibrating table and the mortar was placed in two layers into the test mold during vibration molding.

The test samples were cured in moisture for 24 hours and under the specified curing conditions after demolding. After the samples reached the required testing age, tests were carried out. The evaluation involved non-destructive testing methods to measure the mass, ultrasonic pulse velocity and dynamic elastic modulus, besides the measurements were resumed after 120 days. Moreover, the flexural strength test was carried out, and after each fracture, the compressive strength test proceeded. During the entire loading process, the pressure receiving surface was the two sides of the test sample, and the area is 40 mm×40 mm. The range of 2400 N/s ± 200 N/s is evenly loaded until destruction. The ages for determining the flexural strength and compressive strength were 3, 7, 14, 21, 28, 56, 90 and 120 days, respectively.

3. Results and discussions

3.1 Partial replacement of Portland cement with basalt rock powder

3.1.1 Compressive strength

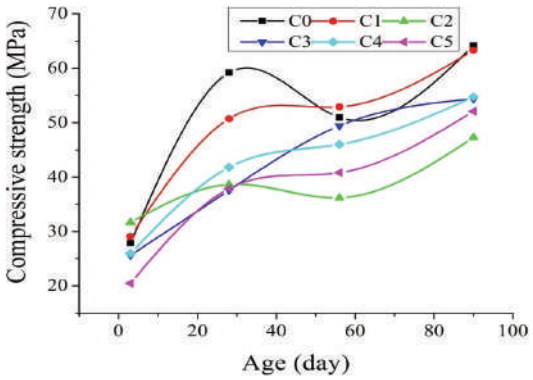

Figure 3.1 Rate curves of compressive strength of cement mortar samples at different testing ages

As shown in Figure 3.1, the effect of using BRP on physical and mechanical characteristics of cement mortar was evaluated. The graph shows that BRP decreased the compressive strength of cement mortar. In early ages, cement mortar with 30% replacement of Portland cement with basalt rock powder illustrated the lowest compressive strength. However, cement mortar containing 15% Portland cement substitution with basalt rock powder indicated the highest compressive strength. Therefore, in the period from 28d to 56d compressive strength significantly increased. The overall trend indicates that at the age of 90 days the best compressive strength results were spotted on the reference cement mortar and the mortar mixture with 10% replacement of Portland cement with basalt rock powder proceeded. Also, it is evident that the cement mortar with 15% substitution of Portland cement with basalt rock powder indicated considerably the lowest compressive strength. Briefly, incorporation of BRP into the cement mortar reduced its strength ability but it is noteworthy to report that the best results amongst modified mixtures was spotted on the cement mortar that contains 10% replacement of Portland cement with basalt rock powder. Its compressive strength diminution was estimated about 1.3% compared to that of reference mortar.

3.1.2 Flexural strength

As indicated in Figure 3.2, the flexural strength changes spotted in cement mortar were graphically presented. The overall results show that flexural strength decreased. Flexural strength tests were carried out at 3d and 28d after the cement mortar samples were prepared. In early ages, only cement mortar that contains 30% substitution of Portland cement with basalt rock powder illustrated the lowest increase rate in flexural strength compared to mortar mixtures. As the age increased, the trend as well changed. Besides, flexural strength sharply inclined for all evaluated mixtures including the reference cement mortar. The overall trend demonstrates that as the age increases, the flexural strength also increases. Moreover, the cement mortar with less amount of BRP illustrated relatively higher flexural strength than those cement mortar mixtures that have more quantity of BRP.

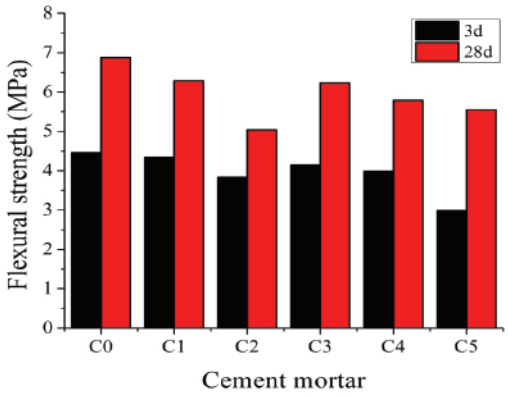

Figure 3.2 Rate curves of flexural strength of cement mortar samples at 3 and 28 days

3.1.3 Dynamic elastic modulus

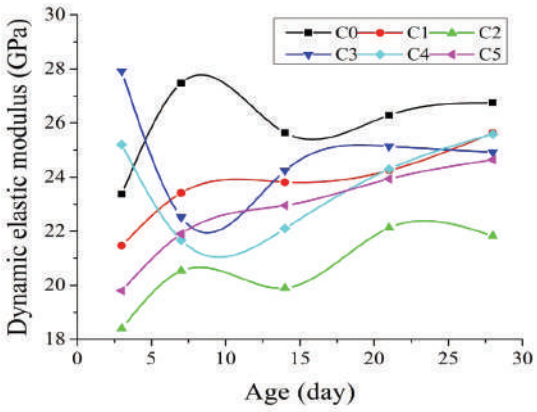

Figure 3.3 Rates curves demonstrate the variation of dynamic elastic modulus of cement mortar samples at different ages

The Figure 3.3 plots the results of the dynamic elastic modulus of cement mortar in interval between 3d and 28d. The graph shows that basalt rock powder affected the elasticity of cement mortar. For instance: at the age 3d, the cement mortar that contains 20% replacement of Portland cement with BRP showed comparably higher value than other mortar mixtures with more than 16% increase over the reference mortar. Whereas the cement mortar that contains 15% replacement Portland cement with BRP demonstrated the lowest value. Moreover, at age of 7d, dynamic elastic modulus sharp increase was spotted on the reference mortar, cement mortar containing 10%, 15% and 30% amount of BRP. Therefore, controversial results were noted on the cement mortar mixtures that contain 20% and 25% BRP. The period between 7d and 14d was marked by incline of dynamic elastic modulus except for reference cement mortar and the cement mortar with 15% BRP which was gradually declining. In the interval from 14d to 21d, the graph indicates a slight growth of dynamic elastic modulus for all mortar mixtures. Finally, at the age of 28d, reference mortar exhibited the highest dynamic elastic modulus. Therefore, mortar mixtures that contain BRP illustrated lower elasticity but it is essential to note that the cement mortar that contains 10% and 25% indicated the best results amongst the modified mixtures with decrease rate roughly 4.2% and 4.4% respectively compared to the reference cement mortar.

3.1.4 Mass

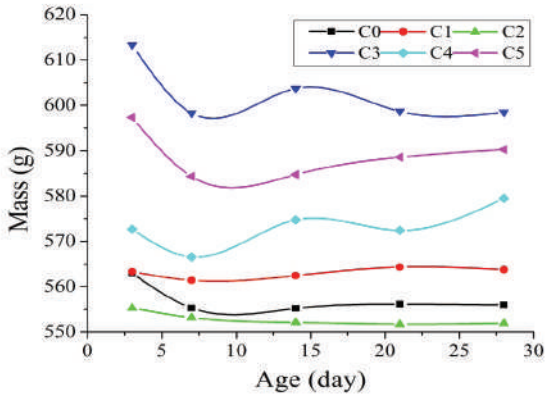

Figure 3.4 Rates curves illustrate the mass variation of cement mortars at different ages

As shown in Figure 3.4, the mass changes of cement mortar were graphically evaluated. Overall results show that addition of BRP changed the weight of cement mortar. At the age of 3d, cement mortar with 15% replacement of Portland cement with BRP weighted lower than other considered mixtures. On the contrary, the cement mortar 20% substitution of Portland cement with basalt rock powder was reported to be the heaviest amongst tested mixtures. The period between 3d and 7d was marked by a slight decline of mortar mixtures weight. Cement mortar mixtures with BRP content indicated dramatic rise of weight except for cement mortar that contains 15% BRP. Therefore, at the age of 28d, the heaviest mortar mixture was the cement mortar that contains 20% BRP with more than 7% increase rate. The lowest weight value was spotted on the cement mortar that contains 15% BRP with roughly 0.6% incline rate compared to the reference cement mortar. Briefly, the incorporation of BRP into the cement mortar sharply increases its weight.

3.1.5 Ultrasonic pulse velocity in longitudinal direction

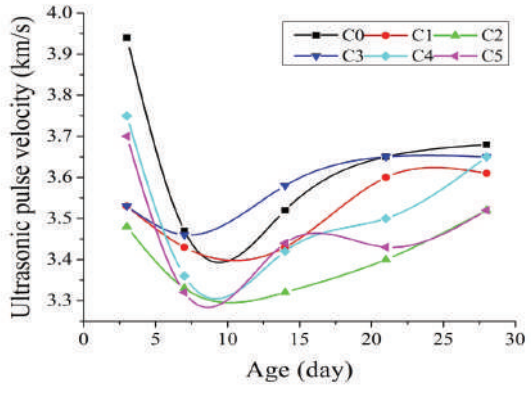

Figure 3.5 The variation of ultrasonic pulse velocity of cement mortars in longitudinal orientation at different testing ages

The Figure 3.5 indicates the evaluation of ultrasonic pulse velocity taken in longitudinal direction of the cement mortar. The incorporation of basalt rock powder into cement mortar reduced its ultrasonic pulse velocity. Overall trend shows that the reference cement mortar showed higher ultrasonic pulse velocity compared to other considered mixtures. For instance, at the age of 3d cement mortar with 15% and 25% basalt rock powder illustrated a decrease estimated about 11.6% and 4.7% respectively. Besides, at the age of 28d, the results noted that the decrease rate on those previously cited mortar mixtures became roughly 10.6% and 7.4 % respectively. Briefly, basalt rock powder decreased longitudinal ultrasonic pulse velocity.

3.1.6 Ultrasonic pulse velocity in transverse direction

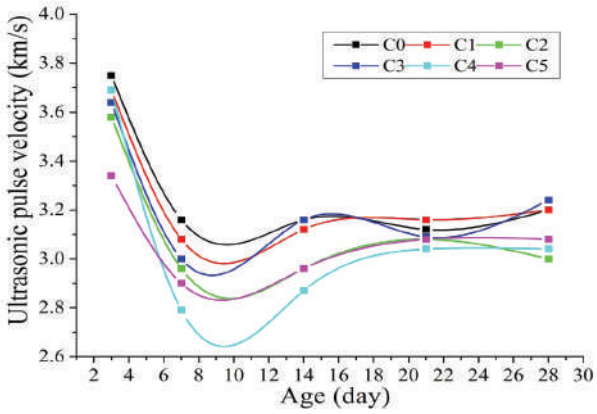

Figure 3.6 The variation of ultrasonic pulse velocity of cement mortars in transverse orientation at different testing ages

The Figure 3.6 illustrates results of ultrasonic pulse velocity taken in transverse direction of the cement mortar. Like it was noted when ultrasonic pulse velocity was taken in longitudinal direction, the graph shows that basalt rock powder decreases ultrasonic pulse velocity of the cement mortar. The best results of ultrasonic pulse velocity were spotted at the age of 3d. Therefore, the reference mortar presented higher ultrasonic pulse velocity compared to modified mixtures. For instance: at the age of 3d, the cement mortar with 25% and 30% indicated a decrease rate of estimated about 6.3% and 15.2% also, the results taken the age of 28d on previously tested mortar mixtures illustrated that diminution of ultrasonic pulse velocity was approximately 22.8% and 21.8%.

3.2 Partial replacement of artificial sand with superfine sand

3.2.1 Flexural strength

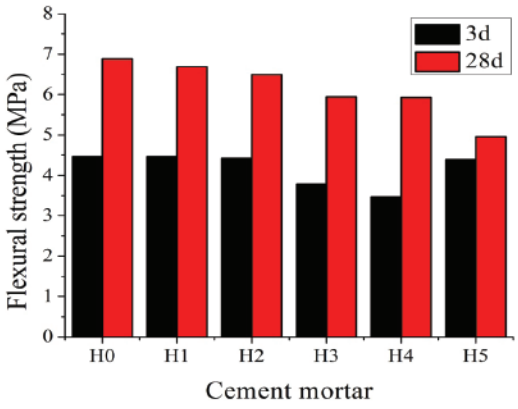

Figure 3.7 The variation of flexural strength of cement mortar at varying age

As demonstrated in the Figure 3.7, the flexural strength of cement mortar increases with increase of curing time. From the graph, it is evident that addition of superfine sand (SS) into

artificial sand (AS) cement based mortar decrease the flexural strength of cement mortar. At the age of 3d, the reference cement mortar indicated the highest flexural strength in comparison to the modified cement mortar mixtures. At the same time, the lowest flexural strength was spotted on cement mortar that contains 40% replacement of AS with SS. Moreover, the flexural strength trend kept gradually increasing and at 28d the noted results showed a sharp increase of flexural strength amongst tested mixtures. The highest flexural strength was spotted on the reference mortar. However, amongst modified mixtures, the remarkable flexural strength was noted on cement mortar than contained lower amount of SS 10% replacement of AS with a drop of nearly 3% compared to reference mortar.

3.2.2 Compressive strength

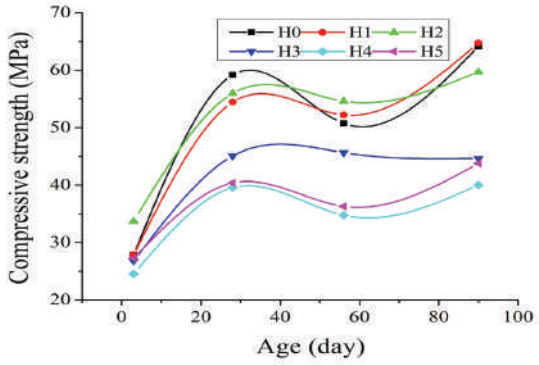

Figure 3.8 The variation of compressive strength of cement mortar at varying age

As shown on Figure 3.8, the compressive strength values of cement mortar were analyzed. The overall results indicated a sharp increase in the period of initial 28d, however between the interval of 28d to 56d the compressive strength dropped generally in tested mixtures, then the trend changed to increasing rate until 90d. At the age of 28d, cement mortar mixtures achieved more than 50% of strength that they exhibited at the age of 90d. For instance: the growth rate of reference cement mortar compressive strength in the period between 28d and 90d was roughly 8%. Moreover, amongst modified mixtures, the cement mortar containing 10% AS replacement with SS exhibited an increase rate in terms of flexural strength estimated nearly 16%. The cement mortar that contained 40% artificial sand substitution with SS indicated the lowest comparable compressive strength decrease of approximately 40% in comparison with reference cement mortar. Broadly, the incorporation of a high quantity of SS as partial replacement of AS significantly decreases compressive strength of cement mortar. But, as the graph indicates, high compressive strength of cement mortar could be achieved if less than 10% AS is replaced with SS.

3.2.3 Mass

As illustrated in Figure 3.9, the mass of the cement mortar was evaluated at different ages. The analysis of the results shows from the age of 3d to 7d the mass of all weighed samples considerably decreased. Eventually, the cement mortar mixtures containing SS exhibited higher mass compared to the reference cement mortar. In addition, the graph shows that the mass of cement mortar decreases with increase of curing time. For instance, the decrease rate of mass of the mixture in the period between 3d and 28d was roughly: 1.1% for the reference mortar and 0.4% for the cement mortar that contains 10% artificial sand replacement with superfine sand. Briefly, the presence of superfine sand as partial replacement of artificial sand notably increased the mass of the cement mortar. Thus, any amount of superfine sand incorporated into the mixture proportion as partial replacement of artificial sand can change its mass. Therefore, the smallest increase amongst modified mixtures was spotted on the cement mortar that contains 50% replacement of artificial sand with superfine sand.

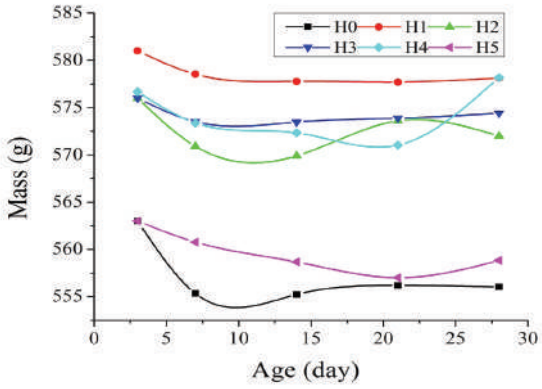

Figure 3.9 The variation of cement mortar mass at varying age

3.2.4 Ultrasonic pulse velocity in longitudinal direction

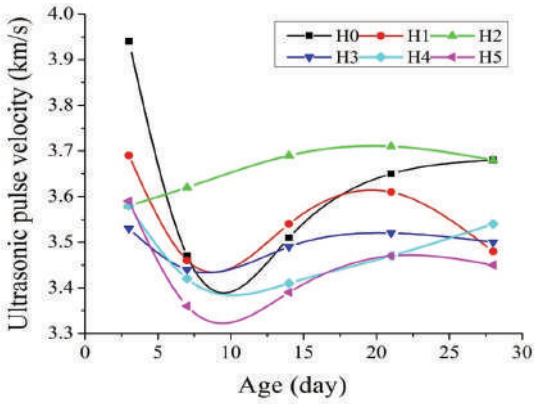

Figure 3.10 The alteration of ultrasonic pulse velocity in longitudinal orientation at varying age

The Figure 3.10 illustrates the evaluation of ultrasonic pulse velocity taken in longitudinal direction. The results show a reduction of velocity as the age increases. At the age of 3d, reference mortar showed the best velocity on the contrary, the cement mortar that contains 30% substitution of AS with SS demonstrated the lowest velocity. Moreover, the measurements taken at the age of 28d indicated that ultrasonic pulse velocity dropped compared to the results obtained on 3d. The highest ultrasonic pulse velocity was noted on the reference mortar and cement mortar that contains 20% replacement of AS with SS. However, the lowest ultrasonic pulse velocity was spotted on cement mortar with 50% replacement of AS with SS. Eventually, based on given results it is evident that SS considerably could reduce ultrasonic pulse velocity in the cement mortar mixture.

3.2.5 Ultrasonic pulse velocity in transverse direction

The Figure 3.11 shows analysis of ultrasonic pulse velocity

in transverse direction. It gives a detailed description of ultrasonic pulse velocity changes occurred in the cement mortar over a period of 28d. As it was spotted in the assessment of ultrasonic pulse velocity in longitudinal direction, the highest velocity was reported at the age of 3d. Also, in interval between 3d and 7d velocity decreased. Then, it slightly increased. At the age of 3d, the reference cement mortar indicated the highest ultrasonic pulse velocity but amongst modified mixtures, the cement mortar that contains 10% replacement of AS with SS showed the best results. Therefore, the lowest velocity value was noted on cement mortar that contains 30% AS replacement with SS. Besides, at the age of 28d, the reference cement mortar and cement mortar that contains 20% AS replacement with SS indicated the best results. Meanwhile, the lowest results were measured on the cement mortar with 30% replacement of AS with SS. Broadly, at 28d, 20% replacement of AS with SS indicated the same result as that of reference cement mortar but other tested mixtures illustrated comparably lower values. Thus, the incorporation of SS into the cement mortar could reduce its ultrasonic pulse velocity.

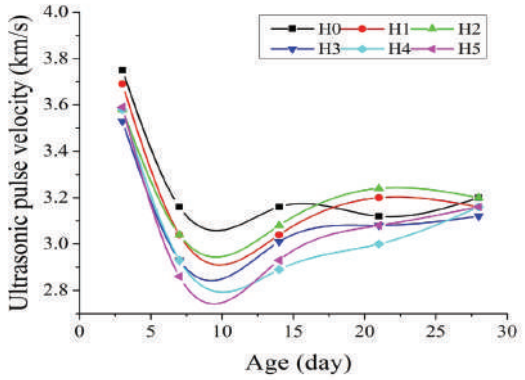

Figure 3.11 The alteration of ultrasonic pulse velocity in transverse orientation at varying age

3.2.6 Dynamic elastic modulus

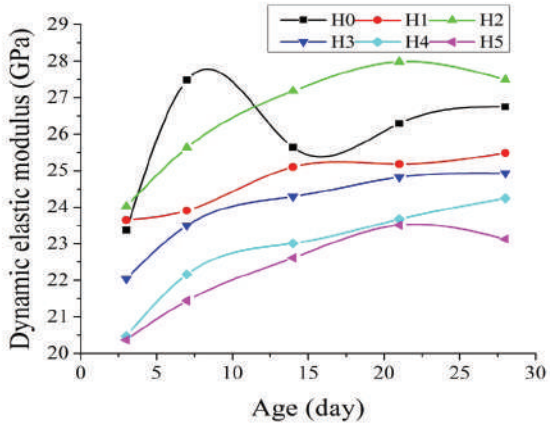

Figure 3.12 The variation of dynamic elastic modulus of cement mortar

As shown in Figure 3.12, the dynamic elastic modulus of the cement mortar was evaluated in the period between 3d and 28d. The reference cement mortar was compared with modified mixtures. The obtained results showed that dynamic elastic modulus of cement mortar increased. At the age of 3d, the cement mortar containing 20% replacement of AS with SS showed the highest dynamic elastic modulus with approximately 3% increase over the reference cement mortar. Besides, at the age of 28d, the cement mortar with 20% replacement of AS with SS remained the highest on account of dynamic elastic modulus value. Then, the reference cement mortar proceeded. To sum up, the superfine sand addition into cement mortar mixture could diminish its dynamic elastic modulus however, 20% replacement of artificial sand with superfine sand increases dynamic elastic modulus of cement mortar.

4. Conclusions

After testing formulated cement mortar samples, the following conclusions can be drawn:

1) Basalt rock powder significantly decreased the flexural strength and dynamic elastic modulus; therefore, the compressive strength and ultrasonic pulse velocity remained comparable. Besides, the weight remarkably increased. Thus, the basalt rock powder quantity ranging between 10 to 25% is considered as the appropriate partial replacement of Portland cement in cement mortar.

2) Superfine sand improved the dynamic elastic modulus and compressive strength of the cement mortar. Simultaneously, the cement mortar exhibited controversial results as the spotted values of ultrasonic pulse velocity and flexural strength at 3d were comparatively lower than those obtained from the reference mortar. But, as the age increased, at 28d SS cement mortar attained almost the same values as those of the reference mortar. Also, the weight significantly increased. The amount of superfine sand ranging from 10% to 20% opted to be the suitable partial replacement of artificial sand in preparation of cement mortar.

To sum up, in order to approve the impact of adding into the cement mortar basalt rock powder as partial replacement of Portland cement and superfine sand as partial substitution of artificial sand, the mechanical performance of formulated cement mortar was investigated through a range of strength assessment experiments. Hence, the suitable replacement of Portland cement with basalt rock powder was from 10% to 25% while on contrary the appropriate replacement for artificial sand with superfine sand ranged from 10% to 20%. Moreover, the findings confirmed that under appropriate circumstances basalt rock powder and superfine sand can be used in cement mortar preparation as partial replacements for Portland cement and artificial sand respectively to achieve profitable use of basalt rock powder and superfine sand deposit in the environment and to promote protection and conservation of natural resources.

Acknowledgement: The authors would like to acknowledge the support of National Natural Science Foundation of China for providing research fund to conduct present study (No. 51168031 and 51468039).

References

[1] Carvalho S.Z., Vernilli F., Almeida B., Oliveira M.D., and Silva S.N. (2018). "Reducing environmental impacts: the use of basic oxygen furnace slag in portland cement." Journal of Cleaner Production, Vol.172, pp. 385–390.

[2] Dobiszewska M., and Beycioğlu A. (2017). "Investigating

the influence of waste basalt powder on selected properties of cement paste and mortar." Materials Science and Engineering, Vol. 245.

[3] Hafsa J. and Mishra R. (2016). "A Green material from rock: basalt fiber – a review." Journal of the Textile Institute, Vol.107, No.7, pp. 923–937.

[4] He Jin Yun, Wang Lu Lu (2012). "C40 Study on the workability and compressive strength of C40 superfine sand concrete." Journal of Hebei University of Engineering (Natural Science Edition) Vol. 29, No. 3 pp. 0-4 (in Chinese).

[5] Kannan D.M., Sherif H.A., Amr S.E and Mahmoud M.R.T. (2017). "High performance concrete incorporating ceramic waste powder as large partial replacement of portland cement." Construction and Building Materials, Vol.144, pp.35–41.

[6] Khandaker H.M.A. (2003). "Blended cement using volcanic ash and pumice." Cement and Concrete Research, Vol. 33, pp. 1601–1605.

[7] Lian H.Z., Chen E.Y. (1996). "Influence of raw materials and mix on high strength & high performance concrete." Concrete, Vol. 5, pp. 10-17 (in Chinese).

[8] Liu L.B., Zhang Y.S., Zhang W.H., Liu Z.Y., Zhang L.H. (2013). "Investigating the influence of basalt as mineral admixture on hydration and microstructure formation mechanism of cement." Construction and Building Materials, Vol. 48, pp. 434-440.

[9] Mehdipour I.D. Ph and Kamal H.K. (2018). "Elucidating the role of supplementary cementitious materials on shrinkage and restrained-shrinkage cracking of flowable eco-concrete." J.Mater.Civ.Eng, Vol. 30, No. 3, pp.1–12.

[10] Mendes Thiago Melanda, Leonardo Guerra, Gilson Morales (2016). "Basalt waste added to Portland cement." Acta Scientiarum. Technology Vol. 38, No. 4, pp. 431-436.

[11] Naceri A. and Makhloufi C.H. (2009). "Use of waste brick as a partial replacement of cement in mortar." Waste Management, Vol.29, No.8, pp. 2378–2384.

[12] Pu X.C., Yan W.N., Wang C. (1999). "Preparation technology on superfine sand super high & high performance concrete." Journal of Chongqing Jianzhu University, Vol.1, pp. 1-4.

[13] Schankoski Rudiele Aparecida, Ronaldo Pilar, Luiz Roberto Prudêncio Jr., Raissa Douglas Ferron (2017). "Evaluation of fresh cement pasts containing quarry by-products powders."Construction and Building Materials Vol. 133, pp. 234-242.

[14] Shyam A., Abdullah A. and Syed A.A. (2017). "A Literature review on study of silica fume as partial replacement of cement in concrete." International Journal of Advanced Engineering, Managment and Science (IJAEMS), No. 3, pp. 250–253.

[15] Singh M., Choudhary K., Srivastava A., Sangwan K.S., Bhunia D. (2017). "A study on environmental and economic impacts of using waste marble powder in concrete." Journal of Building Engineering, Vol.13, pp. 87-95.

[16] Tchamdjou J.W.H., Cherradi T., Abidi M.L., Pereira de Oliveira L.A. (2017). "Influence of different amounts of natural pozzolan from volcanic assessing feasibility of using the heat demand-outdoor scoria on the rheological properties of Portland cement pastes." Energy Procedia, Vol. 139, pp. 696–702.

[17] Topcu İ. B., Bilir T., Uygunoğlu T. (2009). "Effect of waste marble dust content as filler on properties of self-compacting concrete." Construction and Building Materials, Vol.23, pp. 1947-1953.

[18] Tu Er-Hong Tu Er-Di, Zeng Li, Liu Zhi Dong, Gao Zhen (2010). "Superfine sand concrete mix design and test." Concrete Practical Technology, No. 7 pp. 141-144.

[19] Uysal M., Yilmaz K. (2011). "Effect of mineral admixtures on properties of self-compacting concrete." Cement and Concrete Composites, Vol. 33, pp. 771-776.

[20] Veronika Kmecová, Štefunková Zuzana (2014). "Effect of basalt powder on workability and initial strength of cement mortar." Vol. 1, No. 4, pp. 260-267.

[21] Wu Z.W., Lian H.Z. (1999). "High performance concrete." Press of Chinese Railway, pp. 329.

[22] Zhao Y.Q. (2013). "Experimental study on superfine sand concrete mixed by double mixing technology." Research Journal of Applied Sciences, Engineering and Technology Vol. 6, No. 9, pp. 1649–1652.

Viser Technology Pte. Ltd.
Research and Application of Materials Science
https://doi.org/10.33142/msra.v1i1.666

Research Article Open Access

Effects of Si Addition on Microstructure, Properties and Serration Behaviors of Lightweight Al-Mg-Zn-Cu Medium-entropy Alloys

Yasong Li, Ruixuan Li, Yong Zhang*

State Key Laboratory for Advanced Metals and Materials, University of Science and Technology Beijing, Beijing 100083, China

***Corresponding Author:** *Yong Zhang, 30# Xueyuan Road, Beijing, China; drzhangy@ustb.edu.cn*

Abstract:
A series of as-cast lightweight multicomponent alloys $Al_{(86-x)}Mg_{10}Zn_2Cu_2Si_x$ (x=0, 0.3, 0.6, 0.9, 1.2 at.%) were prepared by a vacuum induction furnace with a steel die. With the addition of Si, the reticular white Al-Cu phase deposited were gradually replaced by the gray eutectic Mg-Si phase, while the compressive strength of the alloys increases first and then decreases slowly. It is particularly noteworthy that the compression plasticity also exhibits this trend. When the Si content is 0.9 at.%, the compressive strength reaches its maximum at 779.11 MPa and the compressive plasticity reaches 20.91%. The effect of the addition of Si on the serration behavior of alloy was also studied; we found that the addition of Si introduces a new MgSi phase, and with the change of Si is significantly affects the morphology of the precipitated phase, which affects the serration behavior of the alloys. The comprehensive mechanical properties of the alloy are optimal at the critical point where the serration behavior disappears. In this work, we have provided a method and a composition for the preparation of a low-cost, high-strength, lightweight medium-entropy alloys.

Keywords: *Si Addition; Microstructure and Properties; Serration Behavior; Lightweight, Medium-entropy Alloys*

Citation: Y.S. Li, R.X. Li, Y. Zhang., Effects of Si Addition on Microstructure, Properties and Serration Behaviors of Lightweight Al-Mg-Zn-Cu Medi-um-entropy Alloys. *Res Appl Mat Sci*, 2019,1(1): 10-17. https://doi.org/10.33142/msra.v1i1.666

1. Introduction

As the development of the human beings, environmental issues and energy crisis are gradually being social cognitions. Energy saving, environmental protection, and the low-carbon life have become indispensable topics in people's daily life. Enhancing the use of light-weight materials can effectively save energy and reduce consumption. Besides, traditional aluminum/magnesium alloys have shown good specific stiffness and specific strength, meanwhile, a large number of research results and corresponding applications have been obtained[1-6]. In recent years, the high-entropy alloys have become a hot issue for researchers. Conventional high-entropy alloys are generally formed by Co, Cr, Fe, Ni, Mn as basic elements with alloying elements such as Al, Cu, Ti, and V et al. adding to the solid solution alloys[7-10]. These alloys exhibit excellent mechanical properties such as high strength, high toughness[9], good wear resistance[11], and corrosion resistance[12, 13]. However, such alloys tend to have high density, therefore, how to develop lightweight and low cost high-entropy materials have become the focus of many researchers.

There have been some lightweight high entropy alloys with great properties developed resent years. A new type of low-density, high-entropy alloy $Al_{20}Li_{20}Mg_{10}Sc_{20}Ti_{30}$ has developed by Khaled M. Youssef et al.[14]. This kind of alloy exhibit a nanoscale single face-centered cubic (FCC) solid solution phase, and due to the ultrafine grain structure, it shows not only excellent hardness similar to ceramics such as SiC, but also better ductility. However, since the melting point of Sc and Ti are much higher than Al, Li, and Mg, with mechanical alloying method the problem of preparing such alloys were solved. Furthermore, a new hexagonal close-packed (HCP) structure lightweight high-entropy alloys $Al_{20}Be_{20}Fe_{10}Si_{15}Ti_{35}$ are prepared by TSENG KoKai et al.[15], which exhibit excellent mechanical properties at both room temperature and high temperature. Rui Feng et al.[16] studies the AlCrFeMnTi high-entropy alloys by means of simulation calculation, and the design ideas of lightweight high-entropy alloys are revealed from the perspective of phase diagram, however, due to the addition of Cr, Fe, Mn, the density of the so-called lightweight material is still high, and the design of lightweight high-entropy alloy has not been fully revealed. Xing-hao Du et al.[17] reports a kind of lightweight high-entropy alloys prepared through copper die casting, and it is found that they have superior specific strength with a tetragonal symmetry lattice, however the plasticity of the alloy is not mentioned. Additionally, Rui Li

et al.[18, 19] investigated $Mg_x(MnAlZnCu)_{100-x}$ lightweight high-entropy alloys are and they exhibit high hardness, but the comprehensive mechanical properties are very poor.

More recently, many scholars have also conducted related researches and experiments. Since Al, Li, Mg are common lightweight structural material elements, Yang et al.[20] consider and develop two systems of AlLiMgZnCu and AlLiMgZnSn using the design principles of high-entropy alloys. However, in view of the strong electronegativity of these elements, the high entropy effects do not promote the formation of the single phase solid solution, while bulk intermetallic compounds are generated instead, which therefore results in deterioration in mechanical properties. On the other hands, When the content of Al is dominant as 80 at. %, the alloy tends to form a single face-centered cubic (FCC) solid solution phase. Therefore, two systems of medium-entropy alloy systems $Al_{80}Li_5Mg_5Zn_5Cu_5$ and $Al_{80}Li_5Mg_5Zn_5Sn_5$ have been developed, with compressive strengths exceeding 800 MPa and compression plasticity exceeding 17%. It can be found that although the mixing entropies of these alloys did not reach the maximum, they all showed superior mechanical properties. Based on this research, Baek Eun-Ji, et al.[21] develop an alloy system as $Al_{70}Mg_{10}Si_{10}Zn_5Cu_5$ by means of ultrasonic melting technology, and study the evolution law of the heat treatment phase of the alloys. In addition, the solid solution of medium-entropy alloy Al-6Mg-9Si-10Cu-10Zn-3Ni (wt. %) alloy and phase evolution at different aging temperatures and times were also studied[22, 23], however, ultrasonic melt degassing technology can significantly improve the mechanical properties of the alloy, but the mechanical properties of the alloy at room temperature are not good under high Si content, and it is difficult to decrease the size and morphology of the Si-rich precipitate by heat treatment. Li et al.[24] use supergravity investigated the microstructures of the lightweight Al-Li-Mg-Zn-Cu alloy, it shows that the supergravity method can achieve performance-enhancing alloys by centrifugation in a short time, gravity is also an entropy force, paving the way for the design and synthesis of entropy alloys with intriguing properties.

In this study, the low cost lightweight $Al_{(86-x)}Mg_{10}Zn_2Cu_2Si_x$ (x=0, 0.3, 0.6, 0.9, 1.2 at. %) medium-entropy alloys were prepared. The effect of different Si additions on the microstructure and properties of the alloy was investigated with SEM, universal testing machine, and micro hardness tester. At the same time, the serrated flow behaviors on the compressive stress-strain curve of the alloys were also studied. The effect of Si addition on the serrated flow behaviors and the effect of serrated flow behaviors on the mechanical properties of the alloys were also discussed.

2. Materials and Methods

The alloy ingots of about 120g are prepared by an Ar gas-induced vacuum induction furnace, using industrial pure aluminum (99.7 wt. %), pure magnesium (99.9 wt. %), pure zinc (99.9 wt. %), pure copper(99.9 wt. %) and pure poly-silicon (99.9 wt. %). They were melt at 800℃ for 15 minutes with induction stirring, then poured into a 30mm diameter cylindrical steel die. The nominal compositions of the alloys are shown in Table 1.

The microstructures are observed by Zeiss SUPRA 55 field emission scanning electron microscope (SEM) with energy dispersive spectroscopy (EDS) and electron backscattered diffraction (EBSD). In order to observe the total precipitate phase morphology better, the alloys structure were pre-etched with Keller reagent for 15s. The grain sizes of alloys were analyzed using the EBSD, and the compositions of the precipitated phase were analyzed by EDS.

This experiment uses (Rigaku) D/MAX-RB X-ray diffract-meter to characterize the phase composition of different Si content alloys. The experimental conditions are Cu target Ka, working voltage 30kV, working current 100mA, scanning speed 10 degree/min, range 10-90°.

Table 1. The elemental composition (120g±0.3%)

No.	Al	Mg	Zn	Cu	Si
Al86Mg10Zn2Cu2	99.1	10.5	5.6	5.4	0
Al85.7Mg10Zn2Cu2Si0.3	98.8	10.2	5.6	5.4	0.4
Al85.4Mg10Zn2Cu2Si0.6	98.2	10.2	5.6	5.4	0.8
Al85.1Mg10Zn2Cu2Si0.9	97.9	10.2	5.5	5.5	1.1
Al84.8Mg10Zn2Cu2Si1.2	97.5	10.2	5.6	5.4	1.5

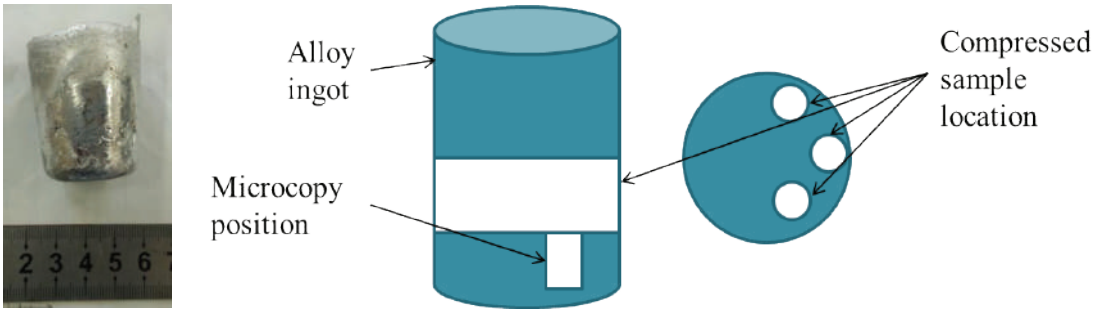

Figure 1 The alloy ingot and the sampling position of the metallographic sample of the compressed sample

The experiments use CMT 4305 Universal Testing Machine to test the compression mechanical properties at room temperature. Using the HXD-1000TM micro-hardness tester to detect the Vickers micro-hardness of the alloy. The alloy ingot and the sampling position of the metallographic sample of the compressed sample are shown in Figure 1.

3. Results and Discussion

3.1 Alloy design

As an inexpensive and lightweight semi-metal element, Si element is added to the aluminum alloy to improve the mechanical properties of the alloy[2, 5, 25-27]. Since Mg and Si are liable to form a high melting point intermetallic compound, for traditional cast aluminum alloys, the Mg/Si ratio has always been strictly controlled variable[28, 29]. Eun-Ji Baek et al.[21] showed that two kinds of Si-containing phases, Mg_2Si, Si and $Al_5Cu_2Mg_8Si_6$, Si were formed in the $Al_{70}Mg_{10}Si_{10}Cu_5Zn_5$ multi-component alloy, during the solidification of the alloy, a stable Mg_2Si phase is primary precipitated at 514-591 °C, when the temperature rises to 500-524 °C, the Si particles precipitated, while the $Al_5Cu_2Mg_8Si_6$ phase is formed at 440 °C. Furthermore, with the addition of Mg, Zn and Cu, some other intermetallics such as Mg-Zn and q-Al_2Cu are formed. As these precipitates have lower melting point, they finally formed out[1, 20, 30, 31]. In addition, Shao et al.[32] studied the high-entropy alloys of AlMgZnCuSi system, which obtained the best mechanical properties of $Al_{85}Mg_{10.5}Zn_{2.025}Cu_{2.025}Si_{0.45}$ alloy. Therefore, this paper intends to study the changes of microstructure and properties of $Al_{86}Mg_{10}Zn_2Cu_2$ alloy under the condition of lower Si addition.

3.2 Effect of Si addition on microstructure

Figure 2 shows the SEM-AsB photos of $Al_{(86-x)}Mg_{10}Zn_2Cu_2Si_x$ alloys under different Si addition, in which we can found that, with the addition of Si, the white eutectic network precipitate is replaced by the black precipitated phase. Figure 2(a) shows the microstructure of the $Al_{86}Mg_{10}Zn_2Cu_2$ alloy, with only white eutectic phase appearing, and with the addition of Si, a black strip phase appears, partially replacing the white eutectic network precipitate, which are shown in Figure 2(b). When the Si content reaches 0.6at. %, the small strip of black precipitated phase converted into the gray eutectic morphology, as shown in Figure 2(c). As the Si content reaches 0.9at. %, the black granular phase and the gray eutectic morphology become obviously larger, as shown in Figure 2(d). When the addition of Si reaches 1.2at. %, the black granular phases gradually increase, and a larger area of eutectic structure appears Figure 2(e). Therefore, a large area of eutectic structure can be formed in the alloy microstructure by the addition of a trace amount of Si, so that the casting property of the alloy can be optimized accordingly. The Figure 2(f) shows the electron backscattered diffraction (EBSD) Euler picture of the alloy with the addition Si 0.9at. %, we can find that the grain size of the alloy is between 200-300 ㎜, since the lattice parameters of the B, C, and D phases cannot be determined, they were appeared as black blind spots on the EBSD image. Also these phases were not only at the grain boundary, and also exist inside the grains.

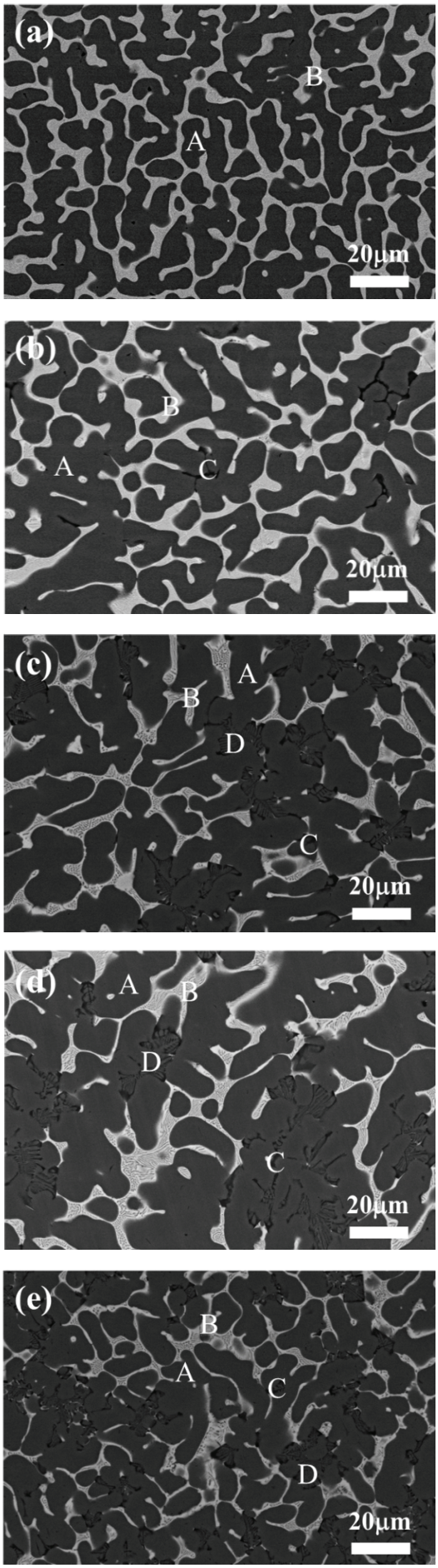

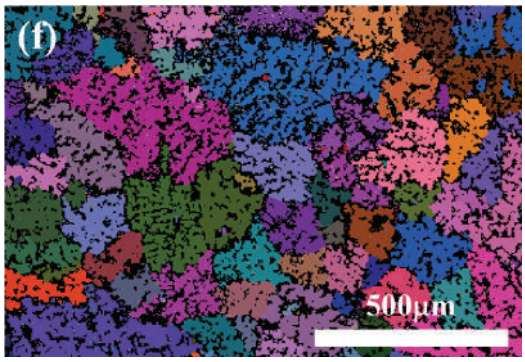

Figure 2 the SEM-AsB photos and EBSD image of the alloys with different Si addition

3.3 Effect of phase formation

Figure 3 shows the XRD pattern of the alloys under different Si addition conditions. XRD pattern analysis of the alloys exhibit that the peak of Mg_2Si appears and become stronger when the amount of Si reaches 0.6at. %, and the $Mg_{32}(AlZn)_{49}$ weakened or even disappeared meanwhile. Eun-Ji Baek's[21] research shows that three kinds of Si-containing precipitates are produced in $Al_{70}Mg_{10}Si_{10}Cu_5Zn_5$. Their results also show that the Si-rich precipitates tend to have higher melting points, and results in the Si-rich precipitates preferentially precipitated during the solidification process, thereby suppressing the precipitation of the MgCuZn-rich phase.

The compositions of different precipitates are characterized by SEM with EDS, which is shown in Table 2. The EDS analysis has shown that a new Si-rich precipitate phase is formed in the alloy with minute quantity Si, and the microstructures have changed significantly. We can see from the EDS data analysis that the three precipitates in the alloy contain different elemental differences. The alloy without Si addition are formed by matrix A phase and B phase. The matrix A phase is α-Al solid solution phase, and it contains less solute elements. The B phase is a eutectic phase, which is rich of Mg-Cu-Zn elements. The C phase is possibly the Mg_2Si phase, and D is the eutectic Mg_2Si.

Table 2. The energy dispersive spectroscopy(EDS) analysis

Element at.%		Al	Mg	Zn	Cu	Si
0	A	92.96	5.34	1.05	0.65	--
	B	67.49	20.94	4.70	6.87	--
Si0.3	A	89.37	5.98	2.81	1.84	--
	B	55.54	18.13	10.59	15.52	--
	C	46.45	27.68	--	1.46	24.42
Si 0.6	A	92.47	4.20	2.34	0.99	--
	B	53.74	16.12	11.41	18.72	--
	C	67.87	14.80	1.07	1.07	15.19
	D	72.73	17.50	0.90	0.53	8.33
Si 0.9	A	91.89	4.15	2.67	1.28	--
	B	61.74	11.68	9.96	16.63	--
	C	53.99	27.50	1.10	1.27	16.15
	D	76.78	9.73	2.95	1.84	8.71
Si 1.2	A	91.24	3.96	2.95	1.85	--
	B	49.26	18.18	12.16	20.40	--
	C	51.41	23.67	1.87	0.93	22.12
	D	73.83	14.63	2.43	1.16	7.92

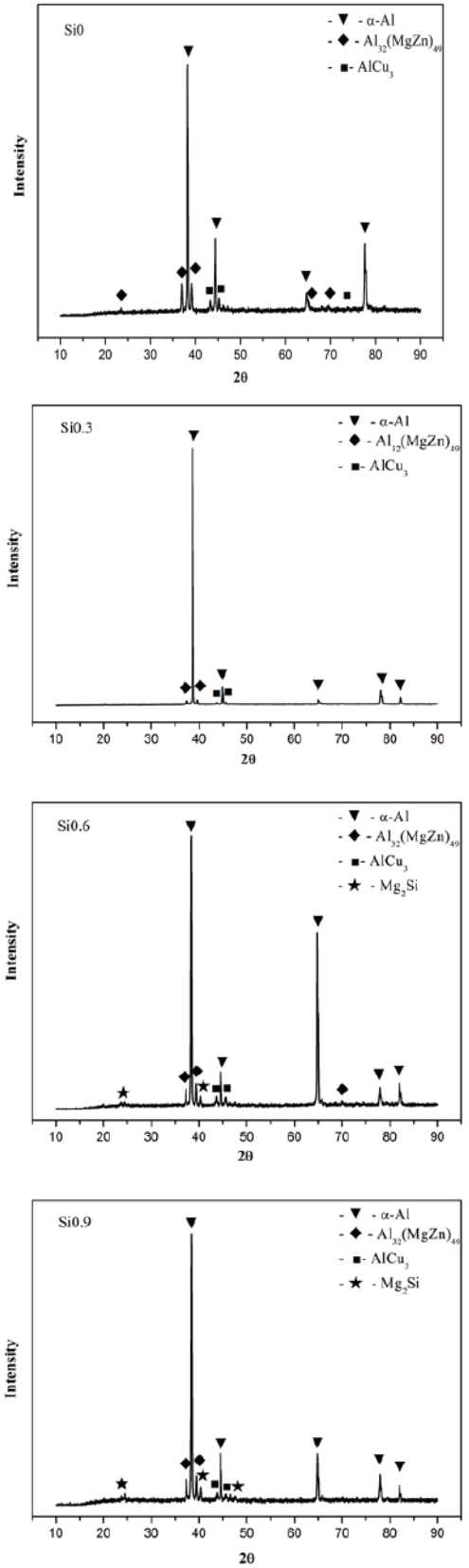

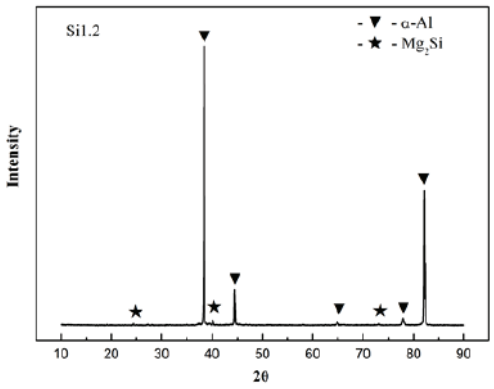

Figure 3 the XRD patterns under different Si contents

3.4 Properties

The compressive stress-strain curves and the micro-hardness of the alloys of the alloys are shown in Figure 4. With the addition of Si addition, the compressive strength of the alloys increases first and then decreases, and its maximum compressive strength reaches 779.11MPa; meanwhile, the compression plasticity of the alloy also shows this trend, and its maximum value reaches 20.9 % when the addition of Si reaches 0.9 at.%. In addition, it is found that there are serrated flows in the compression process, while when the Si content exceeds 0.9at.%, the serrated flow disappears, with the compressive strength and plasticity of the alloy decreasing. We will discuss this phenomenon in Section 4.2. We can find that the trend of the micro-hardness of alloys change is similar to the compressive strength of the alloy with Si addition.

3.5 Serration behavior

The serrated flow behavior of the alloys has become a hot topic for a long time, typically in superalloys[33], aluminum-magnesium alloys[33, 34] and stainless steels[35], in recent years, these behaviors were also found in bulk metal glass[36, 37] and high-entro

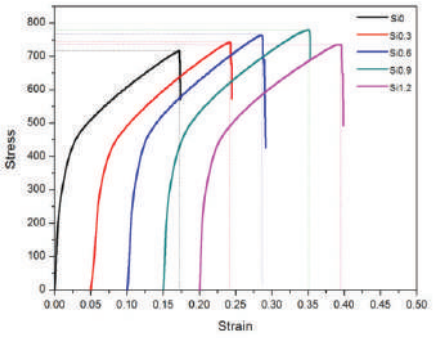

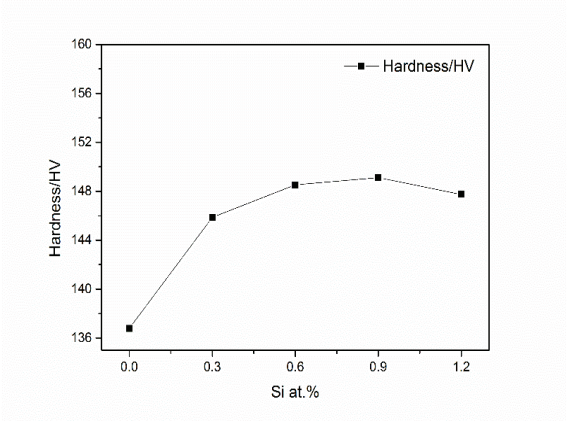

Figure 4 the compressive stress-strain curves and the micro-hardness of the alloys with different Si addition

py alloys[38-40]. For these materials, when there is an appropriate temperature, strain rate or pre-deformation, the avalanche shear deformation accompanying the stress zigzag drop will happen during the compression, which is called the Portevin-Le Chatelier (PLC) effect[34, 41, 42]. The stress increase is due to the hindered and pinned dislocations by the interstitial atoms, which

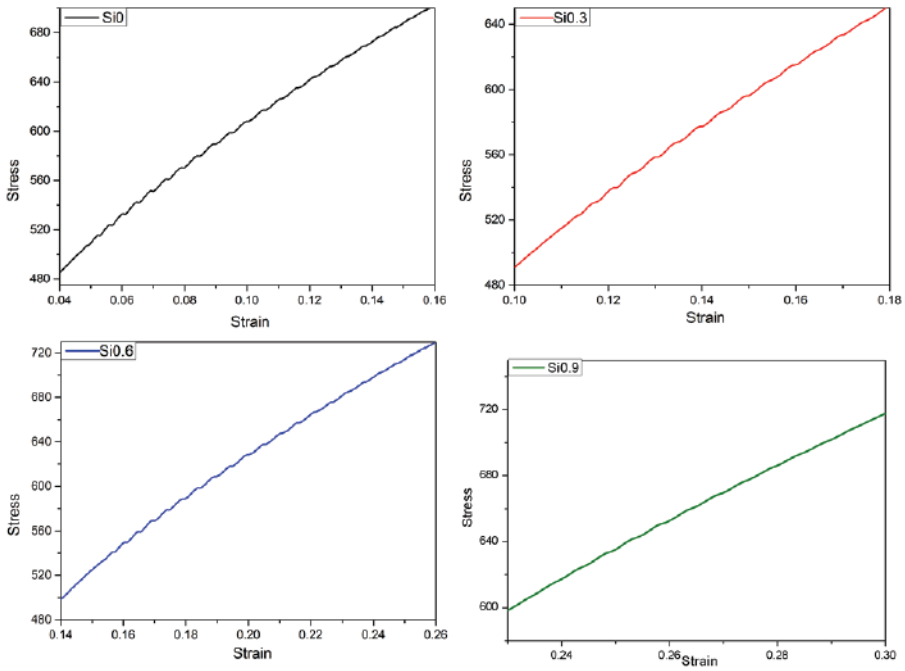

Figure5 the serration flow behavior under initial conditions with different Si addition

causes the dislocation walls or dislocation loops forming, however, when the stress continues to increase, the dislocations will break away from the bond and continue to slip, so that the stress decrease a little. In this way, the cyclic fluctuation of the stress occurs, which can be seen that the serration behavior yield in the metal crystal is related to the dislocation motion and the extension of the Lüders bands. In aluminum-magnesium alloys, these serration flow behaviors often explained by the dynamic strain aging (DSA) theory which is proposed by Cottrell[43], this theory clarifies the dynamic interaction between movable dislocations and solute atoms. At present, there is some controversy about the interpretation of the theory. The DSA theory focuses on the interaction between solute atoms and defects in the crystal. However, the influence of precipitation in the material on the Portevin-Le Chatelier (PLC) effect cannot be ignored, especially in high alloyed aluminum alloy. As an alloying element in Al-Mg alloys, Si is easy to form Mg_2Si precipitates with Mg in the alloys. Therefore, the addition of trace amounts of Si will have a more complicated effect on the serration behavior.

Figure 5 shows the serration behaviors of the alloys, which have Si addition below 0.9at.%. It can be found that, with the increase of Si content, the serration behaviors become weaker and then they turns stronger but not stronger than before. However, when the addition of Si reaches 0.9at.%, Stress-strain curve tends to be smooth. At this time, the alloy exhibits excellent mechanical properties, and the serrated flow is the type D[34]. Through EDS analysis, we can see that the content of solid solution elements in the matrix have a little change. It shows that the change of solid solution elements in the matrix have no obvious influence on the serration flow behavior of alloys. This indicated that the second phases have an effect on the serration flow behavior of alloys.

In order to better study the serration behaviors, we studied the relationship between stress drop with different Si content, which is shown in Figure 6. It can be found that with the increase of strain, the stress drop of the different alloys are shown an approximately linear decrease with slight data fluctuations. On the other hands, with the increase of Si content, the average value of stress drops first decrease, then increase, and finally turn to 0 when the addition of Si reaches 0.9 at.%. This trend is consistent with the serration behavior on the compressive stress-strain curve of the alloys.

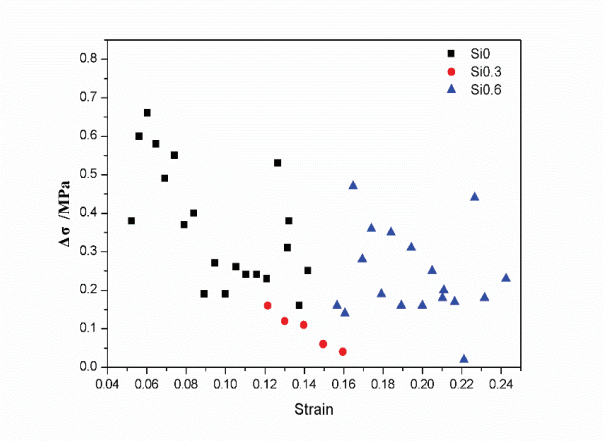

Figure 6 the variation of stress drop with strain under different Si content conditions

Through the analysis of serrated flow behaviors of different alloys, it can be seen that the mechanical properties of the alloys are closely related to the serrated phenomenon. Therefore, the changes of the serrated flow behaviors is mainly due to the changes of the Mg content, which can be explained by the DSA theory. According to the Cottrell-Bilby type kinetics[43], the solute atom concentration around the dislocation line satisfies Equation 1.

$$c_s = c_m \left[1-\exp(-pt^{\theta})\right] \quad (1)$$

where c_s is the solute atomic concentration, c_m is its saturation value, t is the effective time for the solute atoms to disperse into dislocations (t_w is the waiting time), p is a constant related to the solute atom's ability to diffuse, and θ is a constant as 1/3 when solute atoms diffuse by tube diffusion. Based on this, when the content of Mg atoms is lowered, the solute atoms for diffusion are reduced, and the pinning effect on dislocations is lowered. With the addition of Si, a new Mg2Si precipitate phase partially replaces the Al-Mg-Cu precipitates in the alloy. Due to the precipitation of Mg2Si, which affects the serrated flow behaviors exactly, which causes the serrated flow become weaken. At the same time, the precipitation phase formed by the lower addition of Si is finer and its distribution in the matrix also lead to an increase in the mechanical properties of the alloy. Therefore, the influencing factor of the serrated flow behaviors in the alloy is mainly the change of the precipitated phase. As Mg_2Si-phase is formed, the other precipitates decrease. As a result, the influence of precipitation on dislocations becomes weaken, which in turn leads to the weaken of the serration behaviors. When the Si content reaches 0.6 at.%, the precipitation phase of Mg_2Si in the alloy increases remarkably, and its corresponding morphology also changes with the content of Mg in the matrix decreases through EDS analysis. However, the pinning and hindrance of the formed relative dislocations is enhanced, which cause the enhanced strength and serration behavior. As the addition of Si reaches 0.9 at.%, a large number of lamellar eutectic structures forms, and the formation of larger granular Mg_2Si phases leads to further enhancement of alloy strength. Due to the lamellar eutectic structure, the dislocations can easily slides during the compression process, which causes the serration behavior of the alloy to be weaken, and it is very obvious in the compressive stress and strain curve of the alloys. At this time, the stress-strain curve of the alloy has approached the smooth critical point, which may also be the reason for the best compression strength and compression plasticity of the alloy during compression. When the addition amount of Si reaches 1.2at.%, a larger area of eutectic Mg2Si phase appears, and the granular Mg2Si phase grows, causing some casting defects such as pores to occur, and the serration behavior in the alloy disappears, the mechanical properties of the alloy are reduced but higher than without Si addition (as shown in the Figure 4). Therefore, the mechanical properties of the alloy can be optimized under the critical state of the serration behavior of the alloy. The purpose of optimizing the mechanical properties of the alloy can be achieved by paying attention to the serrated flow behavior of the alloy, which provides a new idea for optimizing the mechanical properties of the alloy.

When the Si content reaches 0.9 at.%, the stress-strain curve of the alloy tends to be smooth, and the stress drop is very small. In order to better study the relationship between serration

behavior and alloy properties, we can use elastic strain energy instead of stress drop. The area of stress and strain in the stress rise curve on the stress-strain curve of the alloy reflects the elastic strain energy of the alloy, which is shown in Figure 7. We can find that the elastic strain energy of the alloy increases first and then tends to be stable as the strain increases. With the addition of Si, the average elastic strain energy increases and the serration behavior becomes weaken. It is coincident with the compressive stress-strain curves, which were shown in Figure 5.

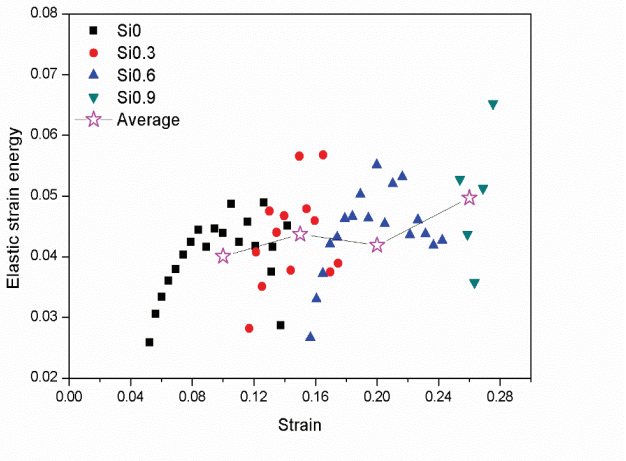

Figure 7 the elastic strain energy of the alloy with different Si addition

The analysis of the elastic strain energy of the alloy shows that the effect of precipitation on the elastic strain energy of the alloy is very obvious, which also affects the serration behavior. With the addition of Si, the Mg_2Si phase forms a new strengthening system with the original precipitation phase, which enhances the comprehensive mechanical properties of the alloy. When the amount of Si is added to 0.3 at.%, the elastic strain energy of the alloy enhanced. When the Si content is further increased to 0.6 at.%, the morphology of the precipitated phase changes, that is to say, the eutectic structure appears. As a result, although the content of precipitated phase has increased, the total strengthening effect has been weakened. In performance, the strength is improved, while the serration behavior is increased and the elastic strain is reduced. When the Si content reaches 0.9 at.%, a large amount of eutectic Mg_2Si and a small amount of granular Si-rich phase appear. The alloy get the highest compressive strength, the highest compression plasticity, and the improved elastic strain energy, with the serration behavior disappearing. Therefore, in addition to solid solution atoms, the morphology and type of precipitated phase also significantly affect the serration behavior of the alloy.

4. Conclusions

In this study, a series of light-weight Al(86-*x*)Mg10Zn2Cu2Si*x* medium-entropy alloys are successfully prepared, and the effect of Si content on the microstructure, properties and serration behaviors are investigated. The results are summarized as follows:

(1) Trace amounts of Si can significantly change the type and morphology of precipitated phases in the alloy, and the appearance of eutectic structure may improve the casting properties of the alloy.

(2) The addition of Si improves the mechanical properties of the alloy, when the Si content reaches 0.9 at.%, the mechanical properties of the alloy are optimal.

(3) The serration behaviors of the alloys also change with the addition of Si. The mechanical properties of the alloy can be optimized under the critical state of the serration behavior, which indicats that the type and morphology of the precipitated phase can significantly affect the serration behavior of the alloy.

Author Contributions: The experiments and writing papers is by Yasong Li, and the paper discussion and revision was assist by Ruixuan Li. Yong Zhang was the corresponding author.

Conflict of Interest: No conflict of interest was reported by the authors.

Acknowledgement: The authors would like to thank the National Science Foundation of China (NSFC, Grants 51671020)and Dongguan Yi'an Technology Co., Ltd. for the financial support.

References

[1] Li H, Cao F, Guo S, et al. Effects of Mg and Cu on microstructures and properties of spray-deposited Al-Zn-Mg-Cu alloys[J]. Journal of Alloys and Compounds. 2017, 719: 89-96.

[2] G. M H, Jacobs, Spencer P J. Thermodynamic evaluations of the systems A1-Si-Zn and Cu-Mg-Ni[J]. Journal of Alloys and Compounds. 1995, 220: 15-18.

[3] Shu W X, Hou L G, Zhang C, et al. Tailored Mg and Cu contents affecting the microstructures and mechanical properties of high-strength Al–Zn–Mg–Cu alloys[J]. Materials Science and Engineering: A. 2016, 657: 269-283.

[4] Jung J, Park S H, Yu H, et al. Improved mechanical properties of Mg–7.6Al–0.4Zn alloy through aging prior to extrusion[J]. Scripta Materialia. 2014, 93: 8-11.

[5] Li Q, Zhao Y, Luo Q, et al. Experimental study and phase diagram calculation in Al–Zn–Mg–Si quaternary system[J]. Journal of Alloys and Compounds. 2010, 501(2): 282-290.

[6] Li C, Sun J, Li Z, et al. Microstructure and corrosion behavior of Al–10%Mg 2 Si cast alloy after heat treatment[J]. Materials Characterization. 2016, 122: 142-147.

[7] Zhang Y, Zuo T T, Tang Z, et al. Microstructures and properties of high-entropy alloys[J]. Progress in Materials Science. 2014, 61: 1-93.

[8] Miracle D B, Senkov O N. A critical review of high entropy alloys and related concepts[J]. Acta Materialia. 2017, 122: 448-511.

[9] Zhang W, Liaw P K, Zhang Y. Science and technology in high-entropy alloys[J]. Science China Materials. 2018, 61(1): 2-22.

[10] Yan X H, Li J S, Zhang W R, et al. A brief review of high-entropy films[J]. Materials Chemistry and Physics. 2018, 210: 12-19.

[11] Cai Z, Cui X, Liu Z, et al. Microstructure and wear resistance of laser cladded Ni-Cr-Co-Ti-V high-entropy alloy coating after laser remelting processing[J]. Optics & Laser Technology. 2018, 99: 276-281.

[12] Gao L, Liao W, Zhang H, et al. Microstructure, Mechanical and Corrosion Behaviors of CoCrFeNiAl0.3 High Entropy

Alloy (HEA) Films[J]. Coatings. 2017, 7(10): 156.
[13] Yao Qiu, Sebastian Thomas, Mark A. Gibson, et al. Corrosion of high entropy alloys[J]. npj Materials Degradation. 2017(1): 1-18.
[14] Youssef K M, Zaddach A J, Niu C, et al. A Novel Low-Density, High-Hardness, High-entropy Alloy with Close-packed Single-phase Nanocrystalline Structures[J]. Materials Research Letters. 2015, 3(2): 95-99.
[15] Tseng K, Yang Y, Juan C, et al. A light-weight high-entropy alloy Al20Be20Fe10Si15Ti35[J]. Science China Technological Sciences. 2018, 61(2): 184-188.
[16] Feng R, Gao M C, Zhang C, et al. Phase stability and transformation in a light-weight high-entropy alloy[J]. Acta Materialia. 2018, 146: 280-293.
[17] Du X H, Wang R, Chen C, et al. Preparation of a Light-Weight MgCaAlLiCu High-Entropy Alloy[J]. Key Engineering Materials. 2017, 727: 132-135.
[18] Li R, Gao J C, Fan K. Study to Microstructure and Mechanical Properties of Mg Containing High Entropy Alloys[J]. Materials Science Forum. 2010, 650: 265-271.
[19] Li R, Gao J C, Fan K. Microstructure and Mechanical Properties of MgMnAlZnCu High Entropy Alloy Cooling in Three Conditions[J]. Materials Science Forum. 2011, 686: 235-241.
[20] Yang X, Chen S Y, Cotton J D, et al. Phase Stability of Low-Density, Multiprincipal Component Alloys Containing Aluminum, Magnesium, and Lithium[J]. JOM. 2014, 66(10): 2009-2020.
[21] Baek E, Ahn T, Jung J, et al. Effects of ultrasonic melt treatment and solution treatment on the microstructure and mechanical properties of low-density multicomponent Al70Mg10Si10Cu5Zn5 alloy[J]. Journal of Alloys and Compounds. 2017, 696: 450-459.
[22] Ahn T, Jung J, Baek E, et al. Temperature dependence of precipitation behavior of Al–6Mg–9Si–10Cu–10Zn–3Ni natural composite and its impact on mechanical properties[J]. Materials Science and Engineering: A. 2017, 695: 45-54.
[23] Ahn T, Jung J, Baek E, et al. Temporal evolution of precipitates in multicomponent Al–6Mg–9Si–10Cu–10Zn–3Ni alloy studied by complementary experimental methods[J]. Journal of Alloys and Compounds. 2017, 701: 660-668.
[24] Li R, Wang Z, Guo Z, et al. Graded microstructures of Al-Li-Mg-Zn-Cu entropic alloys under supergravity[J]. Science China Materials. 2018.
[25] Hallstedt B. Molar volumes of Al, Li, Mg and Si[J]. Calphad. 2007, 31(2): 292-302.
[26] Liu Y, Zhang Y, Yu W, et al. Pre-nucleation clusters mediated crystallization in Al–Si melts[J]. Scripta Materialia. 2016, 110: 87-91.
[27] Sanchez J, Vicario I, Albizuri J, et al. Compound Formation and Microstructure of As-Cast High Entropy Aluminums[J]. Metals. 2018, 8(3): 167.
[28] Xu X, Yang Z, Ye Y, et al. Effects of various Mg/Si ratios on microstructure and performance property of Al-Mg-Si alloy cables[J]. Materials Characterization. 2016, 119: 114-119.
[29] Tao G H, Liu C H, Chen J H, et al. The influence of Mg/Si ratio on the negative natural aging effect in Al–Mg–Si–Cu alloys[J]. Materials Science and Engineering: A. 2015, 642: 241-248.
[30] Li H, Cao F, Guo S, et al. Microstructures and properties evolution of spray-deposited Al-Zn-Mg-Cu-Zr alloys with scandium addition[J]. Journal of Alloys and Compounds. 2017, 691: 482-488.
[31] Guo M X, Zhang Y, Zhang X K, et al. Non-isothermal precipitation behaviors of Al-Mg-Si-Cu alloys with different Zn contents[J]. Materials Science and Engineering: A. 2016, 669: 20-32.
[32] Shao L, Zhang T, Li L, et al. A Low-Cost Lightweight Entropic Alloy with High Strength[J]. Journal of Materials Engineering and Performance. 2018.
[33] Mccormick P G, Ling C P. Numerical modelling of the Portevin—Le Chatelier effect[J]. Acta Metallurgica et Materialia. 1995, 43(5): 1969-1977.
[34] Zhang S, Mccormick P G, Estrin Y. The morphology of Portevin–Le Chatelier bands: finite element simulation for Al–Mg–Si[J]. Acta Materialia. 2001, 49(6): 1087-1094.
[35] Hutanu R, Clapham L, Rogge R B. Intergranular strain and texture in steel Luders bands[J]. Acta Materialia. 2005, 53: 3517-3524.
[36] Yanga F. Plastic flow in bulk metallic glasses: Effect of strain rate[J]. APPLIED PHYSICS LETTERS. 2007(91).
[37] Wei-Hua W. The nature and properties of amorphous matter[J]. PROGRESS IN PHYSICS. 2013, 33(5): 177-351.
[38] Chen S, Yang X, Dahmen K, et al. Microstructures and Crackling Noise of AlxNbTiMoV High Entropy Alloys[J]. Entropy. 2014, 16(2): 870-884.
[39] Chen S, Li W, Xie X, et al. Nanoscale serration and creep characteristics of Al0.5CoCrCuFeNi high-entropy alloys[J]. Journal of Alloys and Compounds. 2018(752): 464-475.
[40] Chen S, Xie X, Li W, et al. Temperature effects on the serrated behavior of an Al 0.5 CoCrCuFeNi high-entropy alloy[J]. Materials Chemistry and Physics. 2018, 210: 20-28.
[41] Zhang Y, Liu J P, Chen S Y, et al. Serration and noise behaviors in materials[J]. Progress in Materials Science. 2017, 90: 358-460.
[42] Kocks R A M F. New observations on the mechanisms of dynamic strain aging and of jerky flow[J]. Acta Metallurgica. 1979, Issue 7(Volume 27): 1125-1134.
[43] Cottrell A H. CRYSTALS, DISLOCATIONS AND PLASTIC FLOW[Z]. London: OXFORD AT THE CLARENDON PRESS, 1953134.

Viser Technology Pte. Ltd.
Research and Application of Materials Science
https://doi.org/10.33142/msra.v1i1.668

Research Article Open Access

Construction of MnO_2 Nanowire for a High-Performance Lithium Ion Supercapacitor

Wenbo Wang[1], Yanhong Shi[1], Yang Su[1], Yihai Wang[1], Haizhu Sun[1*]

[1] National & Local United Engineering Laboratory for Power Battery, College of Chemistry, Northeast Normal University, Changchun, China

***Corresponding Author:** Haizhu Sun, 5268 Renmin Street, Changchun, 130024, China; sunhz335@nenu.edu.cn*

Abstract:
Developing lithium ion capacitors possessing both brilliant energy and power density is still significant for numerous re-searchers. In this paper, we synthesized MnO_2 nanowires via a simple hydrothermal process. The nanostructure MnO_2 can expose more electrochemical sites and thus optimize the kinetics of Li^+. Moreover, we used MnO_2 nanowires (MnO_2 NWs) as anode and a N-doped porous carbon (NPC) as cathode to assemble lithium ion capacitors (MnO_2 NWs//NPC LIC). Compared to the traditional supercapacitor with aqueous electrolyte, the MnO_2 NWs//NPC LIC exhibits a wider voltage of 0-4.2 V, which is helpful to enhance its energy and power density. Furthermore, MnO_2 NWs//NPC LIC can deliver an excellent capacity of 150 mAh g^{-1} with an excellent energy density of 82.7 Wh kg^{-1} and power density of 1.05 kW kg^{-1}. Meanwhile, a good cyclic stability of LICs with a 20% retention after 1000 times charge and discharge process proves its practical potential, indicating a good promising for the application in storage devices.

Keywords: *Manganese dioxide; Nanostructure; N-doped porous carbon; Lithium-ion supercapacitor*

Citation: W. B. Wang, et al., Construction of MnO_2 Nanowire for a High-Performance Lithium Ion Supercapacitor. *Res Appl Mat Sci*, 2019,1(1): 18-23. https://doi.org/10.33142/msra.v1i1.668

1. Introduction

The uninterrupted consumption of fossil fuel cells for huge energy supply boosts the rapid development of energy storage devices [1, 2]. Compared to other energy storage devices [3], lithium ion batteries (LIBs) [4] get much attention because of its outstanding energy density (0.15-0.2 kWh kg^{-1}) while supercapacitors (SCs) [5] stand out owing to its remarkable power density (2-5 kW kg^{-1}) and stable cyclic ability (over 100000 times). Nowadays, the LIBs and SCs are widely applied in manufacturing industry, hybrid electrical vehicle, smart power grids and so on. However, the low power density and poor cyclic stability of LIBs and low energy density of SCs cannot meet the higher and higher demand of people. Therefore, many researchers turn their view to develop a new energy storage system with both outstanding energy density and power density.

Lithium ion capacitors (LICs) are born at this moment by combining a battery-type anode and a capacitor-type cathode [6-8]. To date, a few LICs have been reported containing a wide work voltage window, fast charge/discharge process and superior cycling life. Nevertheless, the existing LICs have an obvious imbalance between two electrodes, resulting from its capacitive reaction that cathode is faster than the intercalation reactions of anode. Therefore, it is of importance to choose proper anode materials with great rate capability to improve this imbalance for a high-performance LICs [9]. Among anode materials, MnO_2 exhibits a low cost and excellent electrochemical properties, gradually becoming a substitute of expensive rare metal oxides. For example, Liu et al. developed bowl-like MnO_2 nanosheets presenting a specific capacitance of 379 F g^{-1} at a current density of 0.5 A g^{-1} while the capacitance retained ratio of 60.5% from 0.5 to 10 A g^{-1} and after 5000 times the capacitance can maintain 87.3% of the original value [10]. Besides, Won-Sub Yoon et al. reported a l-MnO_2 3D nanoarchitecture for LIBs with high capacities of ~1400 mAh g^{-1} at 100 mA g^{-1} and ~749 mAh g^{-1} at 1000 mA g^{-1} [11]. Based on this excellent rate capability, MnO_2 can effectively balance the kinetics of cation and anion, which is helpful to assemble a high-performance LICs.

Carbon materials (such as AC, CNT, graphene, etc) are widely selected as lithium ion supercapacitor electrodes because of their stable and devisable structure, superior conductive characteristic and economic practicality [12, 13]. The wide application in both LIBs and SCs attracts a lot of attention of researchers. For a more excellent electrode, many workers put in a lot of effort to optimize the carbonaceous materials. For example, Huang et al. used F-GDY as anode with a great rate performance (1825.9

mAh g^{-1} at 0.1 A g^{-1}, 979.2 mAh g^{-1} at 5 A g^{-1}) [14]. Peng et al. reported a CNT-threaded N-doped carbon film (CNCF), showing a remarkable specific capacitance of 340 F g^{-1} at 2 A g^{-1}, long cycling life with a Coulombic efficiency of 97.7% after 10000 times at 20000 mA g^{-1} as a supercapacitor electrode [15]. Inspired by these work, N-doped porous carbons are a kind of vital material as the capacitor-type cathode for a more glorious lithium ion capacitor.

Here, we synthesized a kind of MnO_2 nanowire via a simple one spot hydrothermal method. As an anode of LICs, MnO_2 nanowire displays a capacity of 185 mAh g^{-1}at 200 mA g^{-1} with 41.1 % capacity retention at 5C, which benefits from the 3D stacked nanostructure MnO_2 NWs exposing more active sites, increasing surface area and improving the kinetics of Li ions (Li^+). This brilliant rate capacity is beneficial for balancing kinetics between anode and cathode. Particularly, we designed a non-aqueous LICs with a MnO_2 nanowires as anode and an NPC material as cathode. This N-doped 3D porous carbon increases the specific surface area, offering more adsorption sites to shorten the ion transport pathway. The N doping optimizes the wettability between porous carbon cathode and the electrolyte. Therefore, the MnO_2//NPC LIC can deliver a fine capacity of 150 mAh g^{-1} at 500 mAh g^{-1}. Moreover, it demonstrates a superior energy density of 82.7 Wh kg^{-1} at power density of 1050 W kg^{-1} with a good cycling life of LIC with a 20% retention after 1000 times. Especially, a red LED was powered by this MnO_2//NPC LIC, which proved its excellent practical potential.

2. Experimental Section

2.1. Preparation of MnO_2 NWs

The MnO_2 NWs were prepared via the one-step hydrothermal method [16]. Firstly, 158.3 mg $KMnO_4$ and 53.5 mg NH_4Cl were separately added to 30 mL of deionized (DI) water and stirred with a duration of 15 min. After that, the mixture was stirred for 20 min and then dumped into a 100 mL autoclave at 200 °C for 24 h. After cooling down to ambient temperature, the sample was obtained by centrifuge and wash using DI and ethanol 3 times. Finally, the MnO_2 NWs was obtained after drying at 60 °C for 24 h in an oven.

2.2. Preparation of NPC

NPC was synthesized as previously reported [17]. Briefly, gelatin, citric acid and $FeCl_3$ (mass ratio 3:1:4) were added in 0.03 L DI at 90 °C until dissolved. Then, the dried brown gel was calcined at a two-step process (300 °C for 60 min with 3 °C min^{-1}, 800 °C for 120 min at 5 °C min^{-1}) under an Ar/H_2 atmosphere. After acid and DI washing, the black power was obtained. Finally, the power and KOH (mass ratio: 1:3) were mixed homogeneously and activated at 650 °C for 2h. After further acid and DI washing, the NPC was prepared in an oven at 60 °C.

2.3. Electrode Preparation

The anode was prepared by mixing MnO_2 NWs, acetylene black and poly(vinylidene fluoride) (PVDF) with a weight ratio of 7:2:1 in N-Methyl pyrrolidone (NMP). Then, the slurry was smeared on the Cu foil. Similarly, this cathode was synthesized containing N doped porous carbon, acetylene black and PVDF with the same ratio coated on an aluminum foil. All of the prepared electrodes were dried under 100 °C for 12 h in a vacuum oven. These half cells (2032 coin-type cell) were assembled with lithium metal as counter electrode and reference electrode as well as commercial LBC3008A as the electrolyte in the Ar-filled glove box. Before composing the LICs, we gave MnO_2 NWs anodes in close contact with Li metal in the commercial electrolyte LBC3008A for 48 h for a prelithium process. The anode and cathode mass ratio were about 1:3. Specific capacity of MnO_2 NWs//NPC LIC was calculated on a base of anode mass.

2.4. Characterizations

The XRD test was measured on a Rigaku P/max 2200VPC with Cu Kα radiation to investigate the phase of MnO_2 NWs and NPC. SEM (XL 30 ESEM-FEG, FEI Company) and TEM was performed to characterize the surface and interior porous features of as-prepared products. Cyclic voltammetry (CV) and electricimpedance spectroscopy (EIS) were executed on a CHI660E electrochemical workstation (Chenhua, Shanghai). Here, EIS was measured between 10^{-2} Hz and 10^5 Hz. Cycling and rate measurements were carried out by a LAND CT2001A battery measurement system.

The energy density and power density were calculated as follow [18]:

$$P=\Delta V\times i/m \quad (1)$$

$$E=P\times t/3600 \quad (2)$$

$$\Delta V=(V_{max}+V_{min})/2 \quad (3)$$

3. Results and discussion

3.1. MnO_2 NWs as the anode

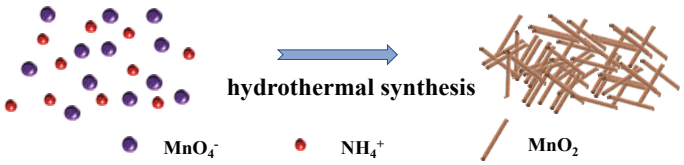

Figure 1. The schematic diagram of MnO_2 nanowires.

The MnO_2 NWs were prepared via a simple hydrothermal process in Figure 1. $KMnO_4$ as Mn source was reduced from Mn (VII) to Mn (IV) to form a stable MnO_2 NWs. Following is the chemical reaction:

$$2NH_4MnO_4 \rightarrow N_2\uparrow+2MnO_2+4H_2O+O_2\uparrow$$

The nanostructure MnO_2 possesses large surface area and more electrochemical sites, and hence optimize the kinetics of Li^+. [19] From SEM images in Figure 2a, MnO_2 exhibits nanowire morphology. Many MnO_2 NWs are intertwined presenting a three-dimensional (3D) network. From a magnification SEM image in Figure 2b, the length of MnO_2 NWs is about 500 ~ 700 nm with a diameter of about 50 nm. Moreover, XRD analysis was conducted to get a further crystal phase of MnO_2 NWs in Figure 2c. It shows that the obtained MnO_2 nanowires are well consistent with the pure MnO_2 with a space group of I4/m (87) (JCPDS: 44-0141). Moreover, the diffraction peaks at 12.8°, 18.1°, 28.8°, 36.7°, 37.5°, 39.0°, 42.0°, 49.9°, 56.4°, 60.3°, 65.1°, and 69.7° correspond to the (110), (200), (310), (400), (211), (330), (301), (411), (600), (521), (002) and (541) planes, respectively, which further confirms the successful preparation of a high crystal pure phase MnO_2 NWs.

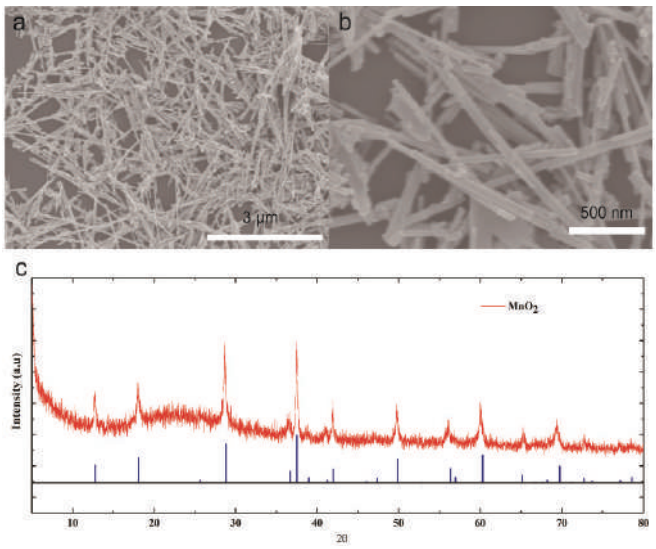

Figure 2. (a) SEM image of MnO_2 NWs with a scale of 3 μm. (b) Magnified SEM image with a scale of 500 nm. (c) XRD pattern of MnO_2 NWs, which confirms that high crystal pure phase 3D stacked MnO_2 NWs are synthesized.

In order to study the electrochemical performance of MnO_2 NWs as anode in LICs, half cells with a counter electrode of Li foil between 0.01 and 3 V (vs. Li/Li^+) was tested. In Figure 3a, CV curves of MnO_2 electrodes at a series of scan rates between 0.1-0.5 mV s^{-1} are presented to reflect the Li^+ transfer in/out of the MnO_2 NWs. At a scan rate of 0.1 mV s^{-1}, the reduction peak at about 0.45 V is assigned to the SEI formation and the transform from Mn (IV) to Mn (0). The oxidation peak at about 1.3 V is attributed to the reoxidation from Mn (0) to Mn (IV). The other CV curves display a similar reaction mechanism. The charge/discharge curves in Figure 3b also proves this process. The reaction is summarized as follow:[20]

$$MnO_2 + 4Li \leftrightarrow 2Li_2O + Mn$$

Moreover, the CV curves at other scan rates exhibit similar redox peaks and retain the curve shape, exhibiting that the MnO_2 NWs have a satisfied rate capacity. Especially, the excellent rate properties are proved from Figure 3c. When the current density is 0.2, 0.4, 0.6, 0.8, 1 and 2 A g^{-1}, the sample shows stable capacities of 185, 175, 122, 100, 76 and 25 mAh g^{-1}. That is to say, when the current density increases 5 times, the capacity retention reaches 41.1%. More importantly, the MnO_2 NWs anode remains 170 mAh g^{-1} after 1000 cycles in Figure 3e, displaying the fine long cyclic stability. The EIS result is conducted in Figure 3d. As known, the smaller the diameter of this semicircle is, the faster the charge transfer. A small charge transfer resistance of MnO_2 NWs benefits to the fast insertion and de-intercalation of Li^+. These outstanding performances are attributed to the nanostructure of MnO_2 and the exposed active sites, which makes MnO_2 NWs a proper candidate for LICs anode.

3.2. NPC as the cathode

N-doped hierarchical porous carbon was chosen as cathode for the LICs. In Figure 4a, a bulk carbon material with a macropore structure is observed. The surface macropores are distributed uniformly with about 500 nm in diameter. The TEM image in Figure 4b exhibits willow-leaf-shaped mesopores. These special pores show a ~160 nm long and a ~40 nm wide. This particular porous structure will effectively shorten transfer pathway and accelerate the transfer of the electrolyte ion. In Figure 4c, the XRD pattern of NPC reflects the degree of graphitization. The peaks at about 25° and 44° are attributed to (002) and (100) planes and this wide shape demonstrates the amorphous nature. This defective structure is resulted from the N and O atom defects reported in previous work. Moreover, the N-doping improves the contact of electrode and electrolyte, further enhancing the electrochemical activation of NPC as cathode for LICs.[21]

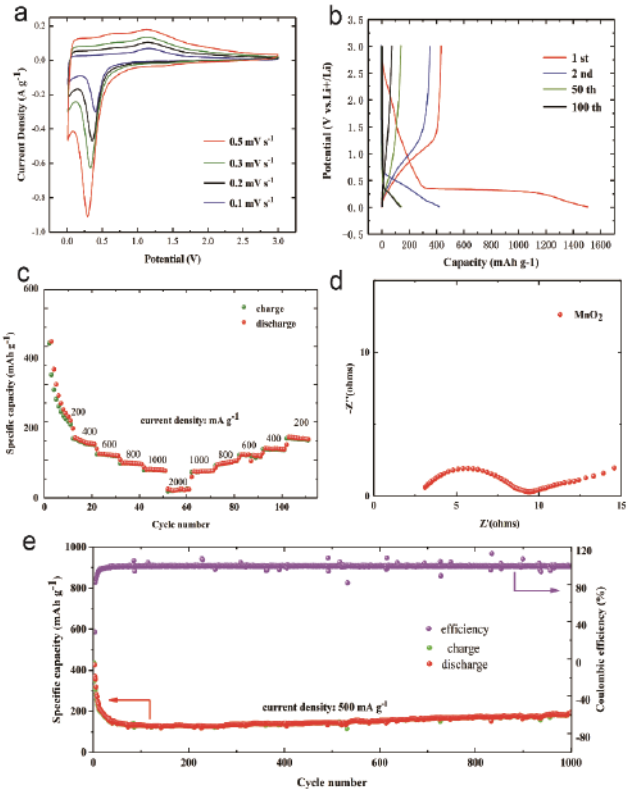

Figure 3. The Li^+ storage properties of MnO_2 NWs anode: (a) CV curves of MnO_2 NWs with scan rates from 0.1 to 0.5 mV s^{-1}, (b) The selected charge-discharge curves at 500 mA g^{-1}, (c) The rate properties with current densities between 200-2000 mA g^{-1}, (d) EIS spectroscopy between 0.01 and 10^5 Hz, (e) the long cycling property and Coulombic efficiencies of this sample at 500 mA g^{-1}, displaying a satisfied electrochemical performance.

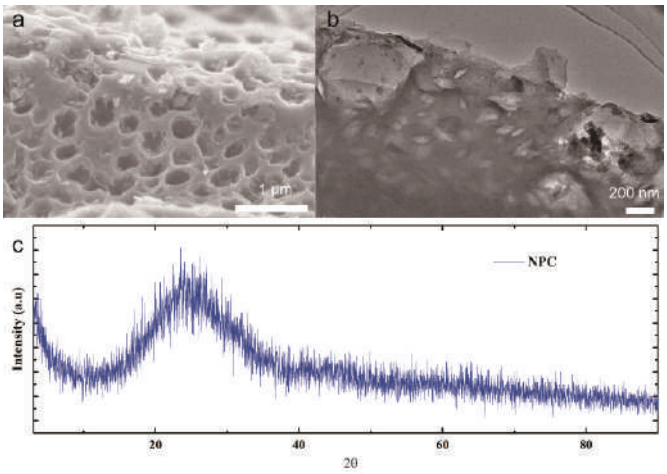

Figure 4. (a) SEM image of NPC at 1μm, (b) TEM image of NPC at 200 nm, (c) XRD pattern of NPC, which shows that N-doped porous carbon possesses a meso and macro structure.

The electrochemical property of nitrogen doped hierarchical porous carbon materials was studied in Figure 5. The CV curve at 1mV s^{-1} with an extended potential window of 2-4.2 V was shown in Figure 5a. Non-redox peaks in these rectangles reflect an ideal capacitive contribution, which corresponds to the charge/discharge curve without any platform in Figure 5b. The selected curves of the 1st, 2nd, 50th and 100th cycles overlap well with each other, illustrating that the NPC cathode has the super stable adsorption ability at 0.5 A g^{-1}. Moreover, the rate property test of NPC cathode in Figure 5c give a series capacity of 97, 75, 66 and 60 mAh g^{-1} at 200, 600, 1000 and 2000 mA g^{-1}, respectively. EIS test in Figure 5d shows that the NPC cathode has a small charge transfer resistance and ion diffusion resistance, further presenting a candidate with a fast ion storage. The cycling performance of NPC in Figure 5e illustrates that the capacity of NPC cathode remains about 30 mAh g^{-1} after 700 cycles. This good adsorption ability is attributed that the 3D porous structure increases the specific surface area, offers more adsorption sites and shortens the ion transport pathway. The N doping optimizes the wettability between NPC cathode and the electrolyte, much suitable for a satisfied performance LIC.

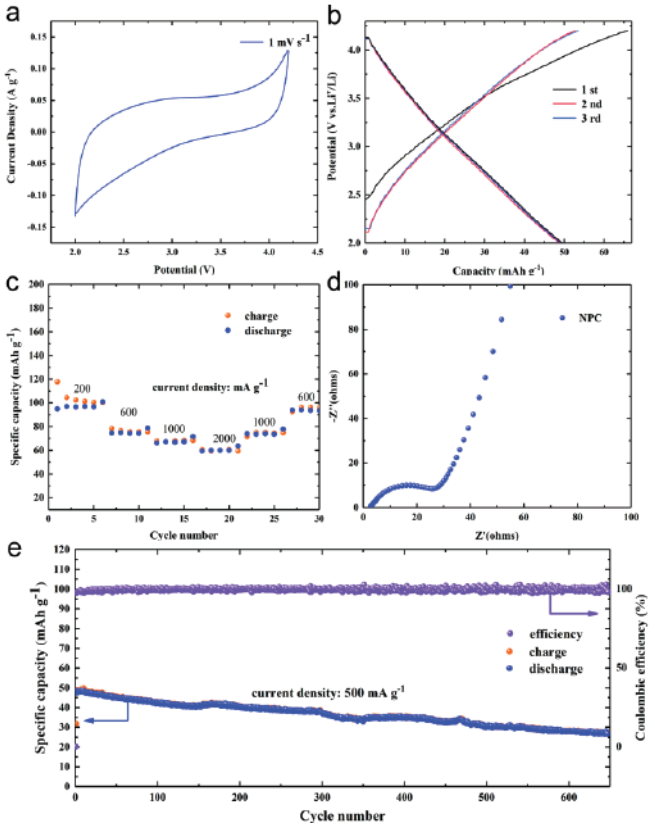

Figure 5. The PF_6^- absorption ability of the NPC cathode: (a) the CV curves of NPC at 1 mV s^{-1}, (b) The charge/discharge curves at the 1st, 2nd, 50th and 100th cycle at 500 mA g^{-1}, (c) The rate property of NPC at 200, 600, 1000, 2000 mA g^{-1}, (d) The EIS spectrum of NPC between 0.01 and 10^5 Hz, (e) The cycling life of NPC at 500 mA g^{-1}, displaying superior adsorption ability.

3.3. MnO_2 NWs//NPC LICs

Utilizing the prepared prelithiated MnO_2 nanowires as anode and the NPC we previously reported as cathode, a LICs with a commercial electrolyte of LBC3008A was assembled. The whole charge/discharge process is explained in detail from Figure 6. In a charge process, the NPC cathode adsorbs the PF_6^- in the surface macro and meso pores with N-doping defects. At the same time, the Li^+ is transferred and reacts to the MnO_2 nanowires anode. The discharge process is the opposite of the charge process. In order to balance the anode and cathode, we make a mass ratio of anode and cathode be 1:3 according to the literature. Moreover, the 3D network of stacked MnO_2 nanowires offers more reaction sites for a fast Li^+ migration, effectively offsetting the intrinsic slow migration rate of Li^+. The 3D porous structure offers more adsorption sites and the N doping optimizes the wettability of NPC. Both of these two advantages make MnO_2 nanowires anode and NPC cathode more matched to construct MnO_2//NPC LICs.

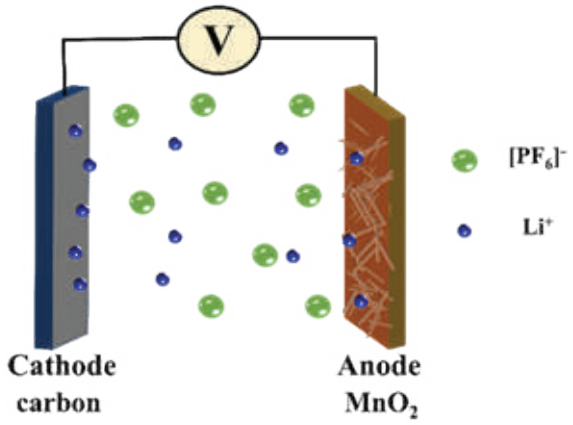

Figure 6. The Schematic model of the LICs assembled by MnO_2 nanowires as anode and NPC as cathode, accuratly interpreting the charge/discharge mechanism of MnO_2 NWs//NPC LICs.

The electrochemical property of MnO_2//NPC LICs is evaluated in Figure 7. Figure 7a exhibits CV curves at different scan rate with an extended potential window of 0-4.2 V. Similar near rectangles and non-redox peaks display an ideal capacitive contribution, which corresponds to no platform in the charge/discharge curve in Figure 7b. The maintenance of rectangle shape further reflects the high rate performance. The charge and discharge curves of MnO_2//NPC LICs exhibit a capacity of 250, 156 and 100 mAh g^{-1} (on base of anode mass) at 0.2, 0.4, 0.6 A g^{-1}, respectively. Its result also confirms the MnO_2//NPC LICs has a good rate property. More interestingly, the satisfied retention of 20% after 1000 times at 500 mA g^{-1} in Figure 7c, demonstrates a stable performance of the MnO_2//NPC LICs. The energy density of 82.7 Wh kg^{-1} and a remarkable power density of 1.05 kW kg^{-1} is comparable to those aqueous supercapacitors such as LFP@C//ARGO [22], LMO/AC Li - Ion flow capacitor [23] and so on in Figure 7d. This illuminates the extended potential range can largely improve the energy density of MnO_2//NPC LICs. The success of a lighted red LED (Voltage: 2 V, current range: 5 mA-17.5 mA) (inset Figure 7d) powered by the MnO_2//NPC LICs further proves its excellent practical potential.

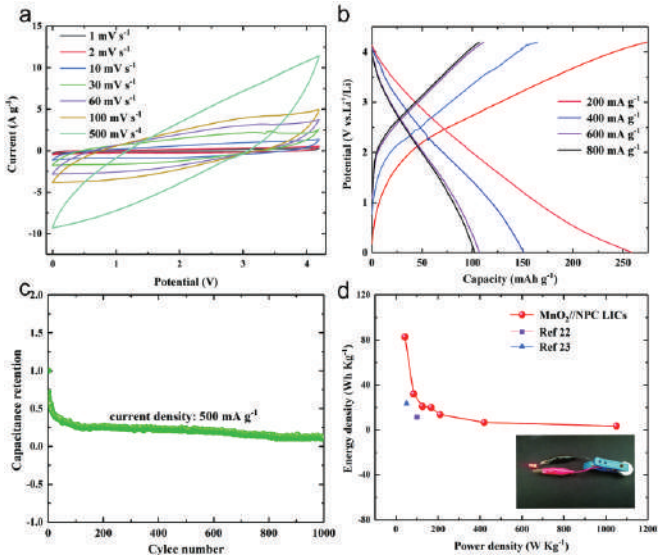

Figure 7. The electrochemical properties of MnO_2 NWs//NPC LICs: (a) The CV curves from 1 mVs^{-1} to 500 mVs^{-1}, (b) The charge/discharge curves at 200, 400, 600 and 800 mA g^{-1}, (c) The cycling stability at 500 mA g^{-1} after 1000 times, (d) The relationship of energy density and power density of MnO_2 NWs//NPC LICs and the comparison with other literatures. The inset is a photo show of a lighted red LED powered by our MnO_2 NWs//NPC LICs.

4. Conclusion

In this paper, the MnO2 nanostructure was successfully prepared via a simple chemical reaction. The obtained MnO2 nanowires expose more active sites and improve the reaction rate with Li+. As an anode of LICs, it delivers a capacity of 185 mAh g-1 at 0.5 A g-1 and accompanies a 41.1 % capacitance maintaining at 1 A g-1. The fine rate performance is beneficial for balancing the kinetics between anode and cathode. Moreover, the NPC material was chosen as cathode to design a non-aqueous LICs. The N-doped 3D porous carbon offers a larger specific surface area, more adsorption sites and a shorter ion transport pathway. The N doping optimizes the wettability between NPC cathode and the electrolyte. In consequence, the MnO2//NPC LICs can display a brilliant capacity of 150 mAh g-1 at 500 mA g-1. Meanwhile, it demonstrates a high energy density of 82.74 Wh kg-1 and a brilliant power density of 1.05 kW kg-1. The success of powering a red LED further proves its excellent practical potential, which provides a realizable thought for the future storage system.

Author Contributions: W.B. Wang, Y.H. Shi, Y. Su, Y.H. Wang and H.Z. Sun are contributors in this work. W.B. Wang performed the whole experiment including samples preparation, electrode preparation, the cell assembly in a glove box and the measurement of electrochemical properties of the cycling and rate performance, the CV curves, the EIS test. Y.H. Shi, Y. Su and Y.H. Wang helped to characterize the morphology features such as SEM, TEM and XRD measurements and analyse the obtained results. Professor H.Z. Sun conducted this whole paper.

Conflict of Interest: No conflict of interest was reported by the authors.

Acknowledgments: Financial supports from the NSFC (21574018, and 51433003), Jilin Provincial Education Department (543), Jilin Provincial Key Laboratory of Advanced Energy Materials (Northeast Normal University) are gratefully acknowledged.

References

[1] Y Wang, S Su, L Cai, et al. Monolithic integration of all-in-one supercapacitor for 3D electronics. Advanced Energy Materials 2019; 9(15): 1900037.

[2] Q Zeng, X Zhang, X Feng, et al. Polymer-passivated inorganic cesium lead mixed-halide perovskites for stable and efficient solar cells with high open-circuit voltage over 1.3 V. Advanced Materials 2018; 30(9): 1705393.

[3] J Guo, F Wan, X Wu, et al. Sodium-ion batteries: work mechanism and the research progress of key electrode materials Journal of Molecular Science. 2016; 32(04): 265-279.

[4] D Xu, W Liu, C Zhang, et al. Monodispersed FeCO3 nanorods anchored on reduced graphene oxide as mesoporous composite anode for high-performance lithium-ion batteries. Journal of Power Sources 2017; 364: 359-366.

[5] K Yang, K Cho, S Yang, et al. A laterally designed all-in-one energy device using a thermoelectric generator-coupled micro su-percapacitor, Nano Energy 2019; 60: 667-672.

[6] J M Campillo-Robles, X Artetxe, K del Teso Sanchez, et al. General hybrid asymmetric capacitor model: Validation with a com-mercial lithium ion capacitor. Journal of Power Sources 2019; 425: 110-120.

[7] C Li, S Cong, Z Tian, et al. Flexible perovskite solar cell-driven photo-rechargeable lithium-ion capacitor for self-powered wearable strain sensors. Nano Energy 2019; 60: 247-256.

[8] C Liu, QQ Ren, SW Zhang, et al. High energy and power lithium-ion capacitors based on Mn3O4/3D-graphene as anode and activated polyaniline-derived carbon nanorods as cathode. Chemical Engineering Journal 2019; 370: 1485-1492.

[9] H Wang, C Zhu, D Chao, et al. Nonaqueous hybrid lithium-ion and sodium-ion capacitors. Advanced Materials 2017; 29(46): 1702093.

[10] P Liu, Y Zhu, X Gao, et al. Rational construction of bowl-like MnO2 nanosheets with excellent electrochemical performance for supercapacitor electrodes. Chemical Engineering Journal 2018; 350: 79-88.

[11] H Kim, N Venugopal, J Yoon, et al. A facile and surfactant-free synthesis of porous hollow □-MnO2 3D nanoarchitectures for lithium ion batteries with superior performance. Journal of Alloys and Compounds 2019; 778: 37-46.

[12] C Yang, M Zhang, N Kong, et al. Self-supported carbon nanofiber films with high-level nitrogen and phosphorus co-doping for advanced lithium-ion and sodium-ion capacitors, Acs Sustainable Chemistry & Engineering 2019 7(10): 9291-9300.

[13] L Zhang, Y Wang, Z Niu, et al. Single atoms on graphene for energy storage and conversion. Small Methods 1800443.

[14] X Shen, J He, K Wang, et al. Fluorine-enriched graphdiyne as an efficient anode in Lithium-ion capacitors. ChemSusChem 2019; 12(7): 1342-1348.

[15] Y Liu, G Li, Z Chen, et al. CNT-threaded N-doped porous carbon film as binder-free electrode for high-capacity supercapacitor and Li-S battery. Journal of Materials Chem-

istry A 2017; 5(20): 9775-9784.
[16] S Wang, BY Guan, L Yu, et al. Rational design of three-layered TiO2@Carbon@MoS2 hierarchical nanotubes for enhanced lithium storage. Advanced Materials 2017; 29(37): 1702724.
[17] Y Shi, L Zhang, TB Schon, et al. Porous carbon with willow-leaf-shaped pores for high-performance supercapacitors. Acs Ap-plied Materials & Interfaces 2017; 9(49): 42699-42707.
[18] Q Xia, H Yang, M Wang, et al. High dnergy and high power lithium-ion capacitors based on boron and nitrogen dual-doped 3D carbon nanofibers as Both cathode and anode. Advanced Energy Materials 2017; 7(22): 1701336.
[19] Z-H Huang, Y Song, DY Feng, et al. High Mass Loading MnO2 with Hierarchical Nanostructures for Supercapacitors. ACS Nano 2018; 12(4): 3557-3567.
[20] L Feng, Z Xuan, H Zhao, et al. MnO2 prepared by hydrothermal method and electrochemical performance as anode for lithi-um-ion battery. Nanoscale Research Letters 2014; 9: 290.
[21] S Wang, Y Shi, C Fan, et al. Layered g-C3N4@Reduced Graphene Oxide Composites as Anodes with Improved Rate Perfor-mance for Lithium-Ion Batteries. Acs Applied Materials & Interfaces 2018; 10(36): 30330-30336.
[22] H Gao, J Wang, R Zhang, et al. An aqueous hybrid lithium ion capacitor based on activated graphene and modified LiFePO4 with high specific capacitance. Materials Research Express 2019; 6(4): 045509.
[23] H Liu, L Liao, YC Lu, et al. High energy density aqueous li-ion flow capacitor. Advanced Energy Materials 2017; 7(1): 1601248.

Viser Technology Pte. Ltd.
Research and Application of Materials Science
https://doi.org/10.33142/msra.v1i1.669

Research Article Open Access

Influence of Processing Technology on Mooney Viscosity and Burning Time of Mixed Rubber

Qi Liu[1], Hui Li[1,2]

[1] Shenzhou Tires in Ningxia,PingLuo,753400,China;
[2] China University of Mining and Technology, Beijing 100039,China

Abstract:
The influence of mixed rubber processing technology on Mooney viscosity and burning time was studied. The results showed that the Mooney viscosity of mixed rubber increased with the extension of the parking time, and the burning time did not change significantly. With the increase of the number of thin pass, the Mooney viscosity of mixed rubber decreases continuously, and the burning time varies with different thin pass temperature..

Keywords: *mixed rubber; Processing technology; Mooney viscosity; Burning time; BoTong*

Citation: Q. Liu, H. Li, Influence of Processing Technology on Mooney Viscosity and Burning Time of Mixed Rubber. *Res Appl Mat Sci*, 2019,1(1): 24-27. https://doi.org/10.33142/msra.v1i1.669

Mooney viscosity, also known as rotational viscosity, is the value measured by Mooney viscometer. Mooney viscosity reflects the quality of rubber processing and molecular weight level and wide distribution range. Low Mooney viscosity rubber easy to adhere to the roll, its molecular weight is low and narrow distribution range. Scorch time is a physical quantity to measure the rate of early vulcanization of rubber. Burning time is too short, in the process of operation will cause the early vulcanization of rubber, affecting rubber mixing, rolling, pressing and other processes; Burning time too long, will lead to rubber vulcanization cycle too long and reduce the production efficiency.

After determining the rubber formula, the main factors affecting the rubber Mooney viscosity and burning time are the rubber processing process. Extending the parking time and increasing The Times of thin pass will affect the Mooney viscosity and burning time of mixed rubber [1]-[3].

1 Experiment

1.1 Main raw materials

Natural rubber: brand SMR20, Malaysia; Brominated butyl rubber: brand BIIR, waf international trade (Shanghai) co., Ltd. Carbon Black: brand Numbers (N234, N326, N375, N660), c Black Cat Carbon Black Co., Ltd. Butadiene rubber: brand BR9000, China petroleum northwest chemical sales branch; White carbon black: brand 175GR, palm Chemical Co.,Ltd; Silane coupling agent: brand tyc-si69, jingdezhen hongbai chemical technology co., Ltd. Zinc oxide: brand name: 99.7%, yangzhou zhenzhong zinc industry co., Ltd. Promoter: brand (NS, DZ, DM), shandong shangshun chemical co., Ltd.

1.2 Basic formula

In this experiment, four basic formulas of tires were selected for research (as shown in table 1).

Table 1 Basic formula of tires/phr

The raw materials	1#	2#	3#	4#
SMR20	100.00	45.00	100.00	20.00
BR9000	/	55.00	/	/
BIIR	/	/	/	80.00
N234	45.00	/	/	/
N326	/	/	56.00	/
N375	/	31.00	/	/
N660	/	22.00	/	69.00
oil	/	5.00	/	8.00
Silica White	15.00	/	/	/
TYC-Si69	3.00	/	/	/
ZnO	3.50	4.00	8.00	/
SA	2.50	2.00	/	2.00
4020	2.00	/	2.00	/
wax	1.00	2.00	/	/
S	1.30	1.40	/	0.80

The raw materials	1#	2#	3#	4#
HD-OT20	/	/	4.50	/
RA-65	/	/	5.00	/
NS	1.50	0.80	/	/
DZ	/	/	1.20	/
DM	/	/	/	1.30
Other	2.50	5.50	2.50	8.80

Note: the basic formula is 100 copies of raw rubber as the benchmark, other raw materials according to the corresponding number of copies.

1.3 Main equipment and instruments

Kobe steel: BB430 mixer; Yiyang rubber & plastic machinery co., Ltd. : GN255 mixer, xk-660 mixer; Qingdao xianrui electromechanical co., Ltd. : xk-160 type smelting machine; Alpha corporation: Mooney viscometer MV2000.

1.4 Sample preparation

The mixing rubber was prepared by conventional mixing process. After 4 hours of parking, 1.5 kg of tread rubber, tire side rubber, tire rubber and dense layer rubber were respectively cut, and roller was used on the XK-160 type furnace.(Roller temperature: 60 ± 5 °C, Roller distance: 2.0 mm) 5 times out of the piece, parked 4 hours after the test.

Through the design of three schemes for mixing rubber Menny viscosity, burning time test study.

Option one: Sampling tests after the specified time for laboratory parking(as shown in Figure 1).

Option 2: After the roller temperature is 45 ± 5 °C and the roller distance is 0.5 mm, the machine is parked for 8 hours(as shown in Figure 2).

Option 3: After the roller temperature is 90 ± 5 °C and the roller distance is 0.5 mm, the machine is parked for 8 hours(as shown in Figure 2).

Laboratory temperature 23±3℃, humidity 40 ~ 60%.

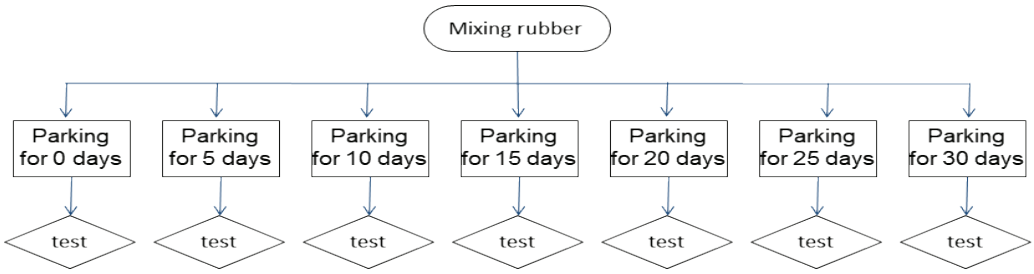

Figure 1 Effect of parking time on mixing rubber test

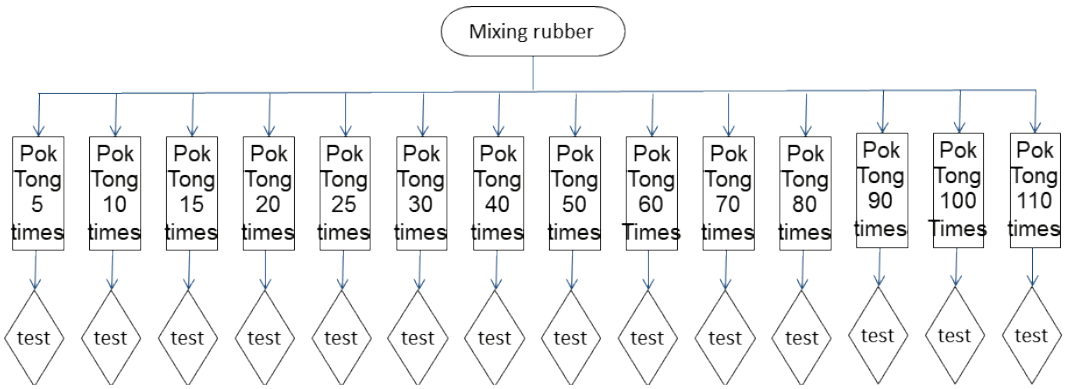

Figure 2 Effect of thin-pass times on mixing rubber

1.5 The performance test

All properties of rubber are tested in accordance with the corresponding national or enterprise standards.

1.5.1 The effect of parking time on rubber properties

Menny viscosity(shown in Table 2) and scorch time(shown in Table 3) of mixed rubber were sampled at intervals of 5 days.

Table 2 Rubber Mooney viscosity test at different parking times

Project	Parking time /d							
	0	5	10	15	20	25	30	R
1#	75	77	77	78	79	79	83	8
2#	62	62	62	62	63	63	64	2
3#	80	82	82	82	83	83	84	4
4#	69	69	70	70	71	71	71	1

Note: the test equipment is American alfarmeni viscometer, ML100℃ (1+4) min (Use a large rotor at 100 °C to Preheat the Menny viscometer cavity for 1 minute and rotate the corresponding Menini viscosity for 4 minutes.); R is for range (the same below).

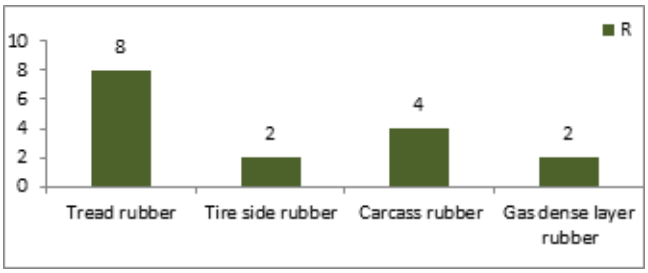

Figure 3 Menny viscosity is range after mixed rubber is parked(R)

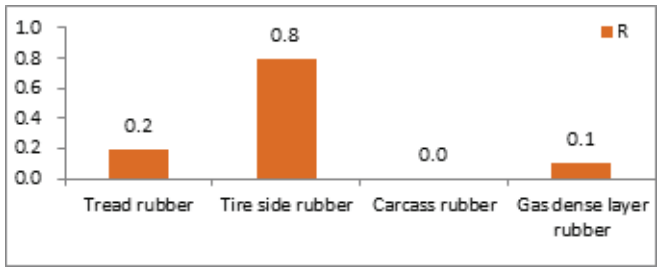

Figure 4 Scorch time is range after mixed rubber is parked(R)

Table 3 Rubber burning time test with different parking time/min

Project	Parking time /d							
	0	5	10	15	20	25	30	R
1#	14	14.1	14	14.1	14.2	14.3	14.2	0.2
2#	19.7	20.1	19.1	18.8	18.5	18.3	18.9	0.8
3#	12.4	12.8	12.2	12.4	12.6	12.7	12.4	0
4#	5.9	5.8	5.7	5.8	5.8	5.9	6	0.1

Note: test equipment, same as above, T5 (Using a large rotor at 130 °C to Preheat the Menni viscometer cavity for 1 minute after the rotor rotates the Menni viscosity value to increase by 5 values.).

Table 4 Rubber Mooney viscosity test at 45±5℃

Project	BoTong number/Number														
	5	10	15	20	25	30	40	50	60	70	80	90	100	110	R
1#	60	59	58	57	57	56	52	56	55	53	52	51	50	49	11
2#	56	56	55	54	54	53	52	54	53	52	51	51	50	49	7
3#	69	66	65	63	62	60	58	53	51	50	48	47	45	43	26
4#	63	62	62	61	61	60	59	62	60	59	59	57	57	55	8

Note: test equipment and test conditions are the same as above.

Table 5 Rubber charring time of 45±5℃ thin pass test/ min

Project	BoTong number/Number													
	5	10	15	20	25	30	40	50	60	70	80	90	100	110
1#	13.7	13.8	13.8	14	14	14	14.1	13.7	13.5	13.6	13.9	13.9	13.8	14
2#	19.9	19.6	19.7	20	20.1	19.9	20.1	21	21	21.4	21	21.1	21.1	21.1
3#	13.4	13.5	13.5	14	13.9	14.2	14.5	16.4	16.4	16.8	16.8	17.1	17.3	17.4
4#	7	7	7.1	7.3	7.6	7.7	8	8.4	8.7	9.1	9.1	9.2	9.5	9.6

Note: test equipment and test conditions are the same as above.

Table 6 Rubber Mooney viscosity of 90±5℃ thin pass test

Project	BoTong number/Number											
	10	20	30	40	50	60	70	80	90	100	110	R
1#	61	58	57	56	55	54	53	52	51	51	51	10
2#	56	55	54	54	52	50	50	49	49	49	48	8
3#	74	73	72	71	71	70	70	69	69	68	68	6
4#	65	65	65	64	64	64	63	63	63	63	63	2

Note: test equipment and test conditions are the same as above.

1.5.2 Effect of thin pass times on rubber properties

(1) the rubber Mooney viscosity (as shown in table 4) and burning time (as shown in table 5) were sampled and tested under thin pass condition with roll temperature of 45±5℃ and roll spacing of 0.5mm.

(2) the rubber Mooney viscosity (shown in table 6) and

Table 7 Rubber charring time of 90±5℃ thin pass test min

Project	BoTong number/Number										
	10	20	30	40	50	60	70	80	90	100	110
1#	14.7	14.8	14.8	14.8	14.9	14.9	15	14.5	14.8	14.5	14.4
2#	24.2	24.2	24.3	24.4	24.5	24.7	25.3	25.1	25.3	25	25.2
3#	15.1	15.1	15.3	15.5	15.5	15.8	15.9	15.8	16	16	16.1
4#	8.4	8.4	9	9.2	9.4	9.5	9.7	9.8	10	10.2	10.1

Note: test equipment and test conditions are the same as above.

burning time (shown in table 7) were sampled and tested under the thin pass condition of roll temperature 90±5℃ and roll spacing 0.5mm.

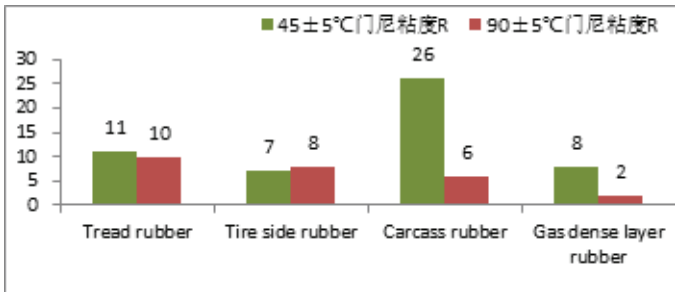

Figure 5 Menny viscosity is range after mixing rubber thinning(R)

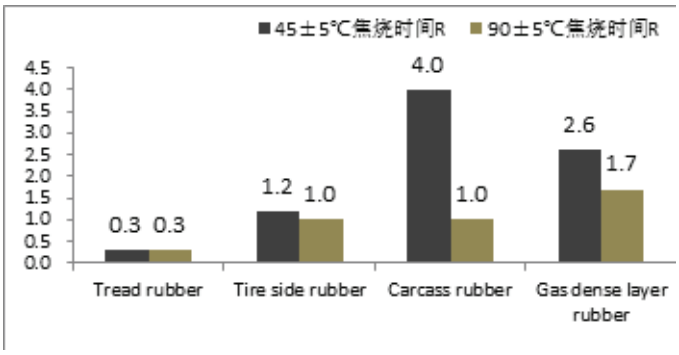

Figure 6 Scorch time is range after mixing rubber thinning(R)

2 Results and discussion

2.1 Effect of parking time on rubber properties

As shown in Table 2 and Figure 3, as the parking time extends, the Meni viscosity of mixed rubber continues to increase, and the Meni viscosity of tread rubber increases significantly.

As shown in Table 2 and Figure 3, as the parking time extends, the burning time of the rubber on the side of the tire is shorter than that of other rubber, and the burning time of other mixed rubber is not obvious.

2.2 Effect of thin pass times on rubber properties

As shown in Tables 4, 6, and 5, with the increase in the number of thin-pass, the Meni viscosity of mixed rubber has decreased, and the low temperature(45 ± 5 °C, the same below) thin-pass has the most effect on the Meni viscosity of fetal rubber. The most obvious.

As shown in Tables 5, 7, and 6, the burning time of mixed rubber has been extended with the increase of the number of thin-pass, and the low temperature thin-pass has the most obvious effect on the burning time of fetal rubber and gas-dense rubber.

The influence of mixed rubber and low-temperature thin-pass on the Moni viscosity and coking time of rubber is more obvious than that of high-temperature(90 ± 5 °C) thin-pass.

3 Conclusion

(1) The parking time(one month) is extended, the Meni viscosity of the mixed rubber is increased, and the burning time of the rubber on the side of the tire is shortened relatively significantly.

(2) Increase the number of thin-pass times(110 times), decrease the Meni viscosity of the mixed rubber, extend the scorch time at low temperature thin-pass(in which the scorch time of the fetal rubber is the most obvious) and extend at high temperature thin-pass. Not obvious.

(3) In the process of actual rubber processing, the effect of extended parking time or extended mixing time on the processing performance of rubber in different parts of the tire is different.

Reference

[1] zhang anqiang, wang lianshi, zhou yiyu, research on coke burning performance in CR mixing process [J], rubber industry, 2003.50 (5) : 261-265.

[2] Jiang zhijie, miao guishao, study on coking time of mixed rubber [J]. Special rubber products, 1999.20 (2) : 12-15.

[3] Lin yaling et al. Scorch characteristics of rubber under mixing conditions [J]. Rubber industry, 2003.50 (11) : 645-650.

Viser Technology Pte. Ltd.
Research and Application of Materials Science
https://doi.org/10.33142/msra.v1i1.670

Research Article Open Access

Fabrication and Growing Kinetics of Highly Dispersed Gadolinium Zirconate Nanoparticles

Renbo Zhu[1], Jianpeng Zou[2], Jie Mao[3*], Xiaofeng Zhang[3], Chunming Deng[3], Min Liu[3], Wenlong Chen[4]

[1] School of Materials Science and Engineering, University of New South Wales, Sydney, Australia
[2] State Key Laboratory of Powder Metallurgy, Central South University, Changsha, China
[3] National Engineering Laboratory for Modern Materials Surface Engineering Technology & the Key Lab of Guangdong for Modern Surface Engineering Technology, Guangdong Institute of New Materials, Guangzhou, China
[4] Guangdong Industrial Analysis and Testing Center, Guangzhou, China

***Corresponding Author:** Jie Mao, Changxing Road No. 363, Tianhe District, Guangzhou, 510650, China, maojie@gdinm.com*

Abstract:
Highly dispersed gadolinium zirconate (GZ) nanoparticles with fluorite structure were successfully synthesized by co-precipitation method, and their phase composition and microstructure, formation mechanism, and grain growth kinetics were investigated. The results suggest that the nanoparticles were obtained through hydroxide dehydration and solid phase reaction. High dispersion was accomplished by ethanol solvent to reduce the hydrogen bond and sodium dodecyl benzene sulfonate (SDBS) surfactant to increase the electrostatic repulsion between the nanoparticles. The grain growth activation energy of GZ powders calcined at lower temperature (< 1200 °C) is 86.5 kJ/mol (Q_l), and the grain growth activation energy of GZ powders calcined at higher temperature (> 1200 °C) is 148.4 kJ/mol (Q_h). The current study shows that the optimal process to synthesize dispersed GZ nanoparticles includes ethanol solvent, 3 wt.% SDBS surfactant, and 1100 °C as calcining temperature.

Keywords: *Gadolinium zirconate; Co-precipitation method; Phase structure; Kinetics; Dispersed nanoparticles*

Citation: R.B. Zhu et al., Fabrication and Growing Kinetics of Highly Dispersed Gadolinium Zirconate Nanoparticles. *Res Appl Mat Sci*, 2019,1(1): 28-34. https://doi.org/10.33142/msra.v1i1.670

1. Introduction

The rare earth zirconates, $Ln_2Zr_2O_7$ (Ln denotes a rare earth element) with pyrochlore and defect fluorite structure, have received considerable attention in various industrial applications, including matrix nuclear fuel [1–3], catalytic materials [4–6], and thermal barrier coatings (TBCs) [7–9]. These zirconates have significant advantages, which include low thermal conductivity and excellent thermal stability [10–13]. Therefore, $Ln_2Zr_2O_7$ is widely used as TBCs to provide better thermal insulation and corrosion resistance for hot-section components of gas turbines.

$Gd_2Zr_2O_7$ (GZ) is a good candidate as it shows significant superiority over traditional Y_2O_3 stabilized ZrO_2 (YSZ) materials due to its low sintering rate, low thermal conductivity and high thermal stability [14–16]. Besides, GZ presents the relatively higher coefficient of thermal expansion (CTE) among the rare earth zirconates [17], which contributes to the relatively lower thermal stress in the interface of ceramic layer and bond layer and longer service life. Well dispersed nanoparticles increase material reactivity, which assists TBC preparation, such as powder evaporation in the plasma plume and columnar coating formation with better fracture resistance.

Various methods have been proposed to obtain highly dispersed GZ nanoparticles, including solid-state reaction, sol-gel, combustion, hydrothermal synthesis and co-precipitation [11,18–21]. Solid-state reaction is the common method to synthesize zirconate nanoparticles but requires high sintering temperature (above 1450 °C) [22], which is not good for achieving high dispersion, since agglomeration becomes more severe at higher sintering temperatures. Composition segregation is another shortcoming in this method. It is necessary to use the expensive alkoxide in the sol-gel method, which is unsuitable for manufacturing nanoparticles. High heating and cooling rates in the combustion method cause the formation of defect concentration and non-equilibrium phase in the products. The hydrothermal method presents the high requirements for the equipments and can produce a limited amount of powders. On the other hand, the co-precipitation method can reduce synthesis temperature,

improve production, and accurately control chemical composition. Thus, co-precipitation has a great potential for manufacturing dispersed GZ nanoparticles.

It is difficult to produce the highly dispersed nanoparticles by traditional coprecipitation method since the agglomerations and sintering still exist in this process. The agglomeration includes soft agglomeration and hard agglomeration [23]. Soft agglomeration arises mainly from Van der Waals attraction, which can be destroyed easily and is beneficial to obtain dispersed particles. Hard agglomeration is formed with solid neck connection, which can't break easily. Water molecules can bridge neighboring precipitates in the co-precipitation process, producing hard agglomerates with solid necks and connecting neighboring particles after precipitate dehydration [24]. While, hydroxyl groups in the ethanol solvent are the terminal groups and obstruct bridge formation, which are promising in fabricating GZ nanoparticles with high dispersion.

However, few studies have considered agglomeration effects in the highly dispersed GZ nanoparticle production. This paper aims to synthesize GZ nanoparticles with less agglomeration by the modified co-precipitation method. The phase composition, microstructure, formation mechanism, and grain growth kinetics are also investigated.

2. Materials and methods

2.1. Preparation

Gadolinium nitrate and zirconium oxychloride (99.99%, Golden Dragon Rare-Earth Co., Ltd., Fujian, China) were dissolved in ethanol and distilled water solvent, respectively. Then, the solutions were mixed at the atomic proportion of Gd : Zr = 1 : 1 and stirred for 30 min with different sodium dodecyl benzene sulfonate (SDBS) dispersants ratios. The precursor solution was added dropwise into ammonium hydroxide (pH = 10) while continuously stirring to fabricate hydroxide precipitates. After filtration, the precipitates were continuously washed with the same corresponding solvent until pH of filtrate is 7. Then, the precipitates were dried at 100 °C for 10 h. After grinding in the zirconia balls and jars for 2 h (ball to precipitate mass ratio is 1 : 1), the dried precipitates were calcined above 900 °C for 2 h.

2.2. Analyses and measurements

X-ray diffractometry (XRD, D/max 2550PC, Japan) was used for phase analyses of GZ powders with different calcining temperature at a scan rate of 4 °/min. The phase structure of the GZ powders was identified by Fourier-transform infrared (FTIR) spectroscopy (Spectrum-2, America). Particle morphology was analyzed with scanning electron microscopy (SEM, S-4300, Japan), transmission electron microscopy (TEM, JEM-2100F, Japan) and high-resolution transmission electron microscopy (HRTEM, JEM-2100F, Japan). GZ powders were also analyzed by the selected area electron diffraction (SAED) patterns. Thermal analysis of dried precipitates was performed in the air by thermo gravimetric and differential scanning calorimeter (TG/DSC, STA-449-F5, Germany) from 25 °C to 1400 °C at a heating rate of 10 °C/min. The GZ powder specific surface areas were calculated by the Brunauer–Emmett–Teller (BET) nitrogen adsorption method.

3. Results and discussion

3.1. Gadolinium zirconate powder phase composition and microstructure

Figure 1 presents the XRD patterns for GZ powders precipitated in the ethanol solvent with 3 wt.% SDBS and calcined above 900 °C for 2h. The samples exhibit similar XRD patterns, identified as single phase with defect fluorite structure (JCPDS No. 01-080-0471, space group Fm-3m). No distinct diffraction peaks of impurities exist. Thus, the pure substitutional solid solution has been successfully synthesized. As calcining temperature increases, diffraction peaks of GZ powders are sharper, which indicates GZ grain growth and improved crystallinity. However, there is no phase transformation from defect fluorite structure to pyrochlore structure, hence the defect fluorite structure remains relatively stable up to 1400 °C.

As crystallization is fully developed by 1100 °C, it is necessary to set the calcining temperature above 1100 °C to ensure nanocrystal integrity. However, higher calcining temperature contributes greatly to nanoparticle sintering and hard agglomeration, which are not good for synthesizing highly dispersed nanoparticles. Thus, calcining temperature should be 1100°C to ensure both good GZ powder dispersion and crystal integrity.

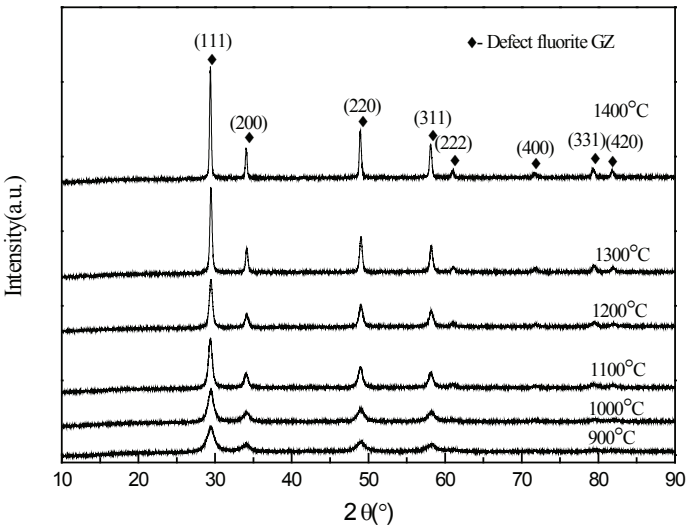

Figure 1. XRD patterns of gadolinium zirconate powders precipitated in ethanol solvent with 3 wt.% SDBS at various calcining temperatures.

Figure 2 exhibits the infrared spectra of GZ powders at different calcining temperatures. The absorption bands centered at approximately 3446 and 1638 cm^{-1} are attributed to the residual water in the GZ powders, whereas bands in 1000–780 cm^{-1} correspond to residual nitrate vibrations. The absorption band at ~ 610 cm^{-1} is shown due to Zr–O bonds in the lattice, and the vibration frequency of Gd–O bonds is detected at 420 cm^{-1}. Bands at 1517, 1398 and 1123 cm^{-1} correspond to C=C, C–N, and C–H bonds in the powders calcined at 1000 °C [25,26]. As calcining temperature increases to 1100 °C, these three bonds disappear, indicating loss of impurities.

Figure 3 shows SEM micrographs of GZ nanoparticles fabricated in various ways. GZ powders precipitated in water solvent (Figure 3a) exhibit no significant boundaries among GZ nanoparticles, which are severely agglomerated into larg-

er clusters. Particle boundaries are clearly differentiated in the powders precipitated in ethanol solvent (Figure 3b), indicating better dispersion of GZ particle. BET surface areas were 23.4 and 44.5 m^2/g for the powders precipitated in the water and ethanol, respectively. The larger BET surface area confirms that powders precipitated in the ethanol have better dispersion. Nanoparticles with different SDBS ratios (2, 3, and 4 wt.%) show BET surface area 62.3, 98.6, and 85.7 m^2/g, respectively (Figure 3c, Figure 3d, Figure 3e), indicating that the amount of SDBS in dispersion follows the order: 3 > 4 > 2 wt.%. The dispersion mechanism is discussed in section 3.2.

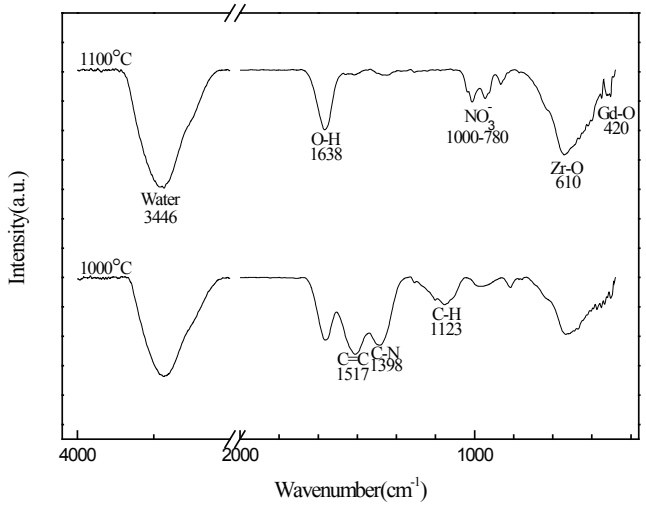

Figure 2. Infrared spectra for gadolinium zirconate powders precipitated in ethanol solvent with 3 wt.% sodium dodecyl benzene sulfonate at various calcining temperatures.

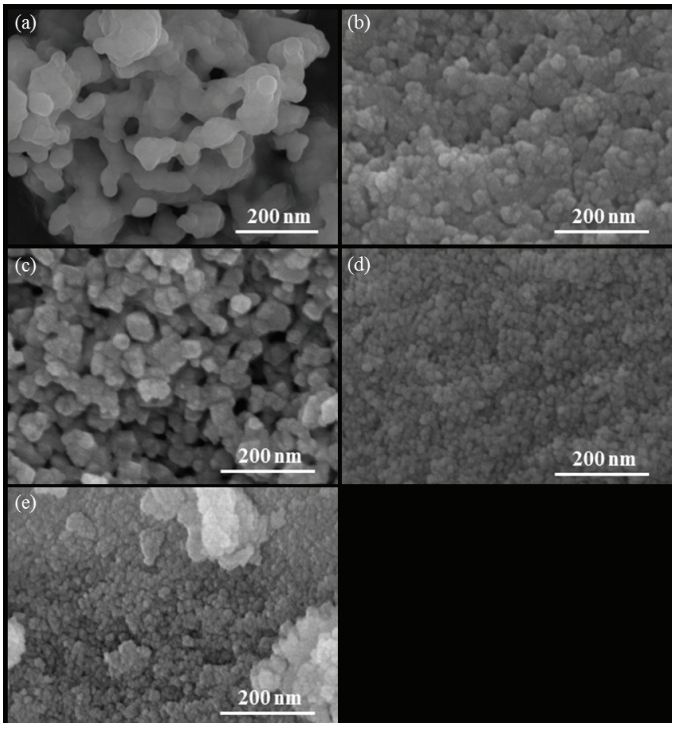

Figure 3. SEM images for gadolinium zirconate nanoparticles prepared with (a) water; (b) ethanol; and (c) 2 wt.%, (d) 3 wt.%, and (e) 4 wt.% sodium dodecyl benzene sulfonate.

Figure 4 shows TEM/HRTEM images and SAED patterns for GZ powders precipitated in the water and ethanol solvent with 3 wt.% SDBS. GZ particle size is above 20 nm when precipitated in the water (Figure 4a), and GZ nanoparticles are closely agglomerated into large and dense particles. In contrast, nanoparticle size is below 20 nm when precipitated in the ethanol solvent with 3 wt.% SDBS (Figure 4b). The GZ powders precipitated in the ethanol are better dispersed than the powders precipitated in the water. Figure 4c shows a typical HRTEM image for powders precipitated in the water, exhibiting wide lines between the grains with different orientations. It originates from Moire patterns induced by nanocrystal overlay, indicating agglomeration and sintering behavior between nanoparticles precipitated in the water. GZ powders precipitated in the ethanol exhibit clearer grain boundaries (Figure 4d), indicating better dispersion. The SAED pattern (Figure 4e) exhibits defect fluorite structure, consistent with XRD analysis, and the sharp rings indicate polycrystalline material. SAED pattern from a single grain (Figure 4f) shows diffraction spots of atomic planes, belonging to the corresponding atomic planes in the face-centered cubic structure of GZ grain.

3.2. Gadolinium zirconate powder formation mechanism

Hydroxide thermal analysis is conducive to clarifying hydroxide decomposition and GZ formation. Figure 5 presents the TG/DSC analysis for dry hydroxide precipitates. The DSC curve of hydroxides shows a distinct endothermic peak at approximately 111 °C, accompanied by an abrupt weight drop (~10%) due to the removal of residual water in the precipitates [27]. The endothermic peak at approximately 483 °C corresponds to zirconium hydroxide decomposition, and the peak at approximately 628 °C corresponds to gadolinium hydroxide decomposition. No significant weight loss occurs above 628 °C, indicating that zirconia and gadolinia formation has almost completed. The exothermal peak at approximately 1065 °C corresponds to the solid phase reaction of powders, in which zirconia and gadolinia react to form GZ.

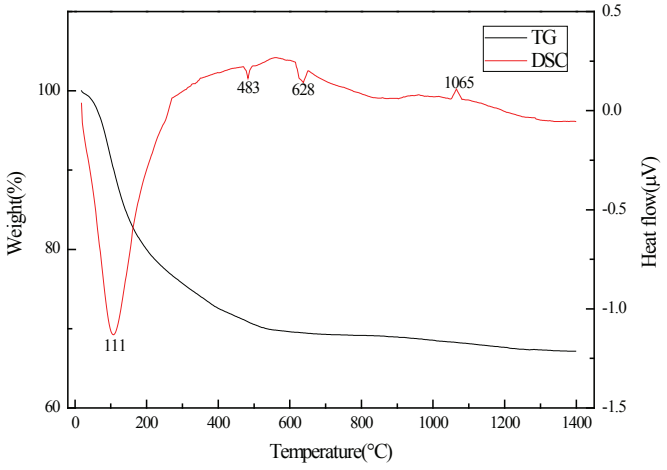

Figure 5. Thermogravimetric (TG) and differential scanning calorimeter (DSC) curves for hydroxide precipitates precipitated in ethanol solvent with 3 wt.% sodium dodecyl benzene sulfonate

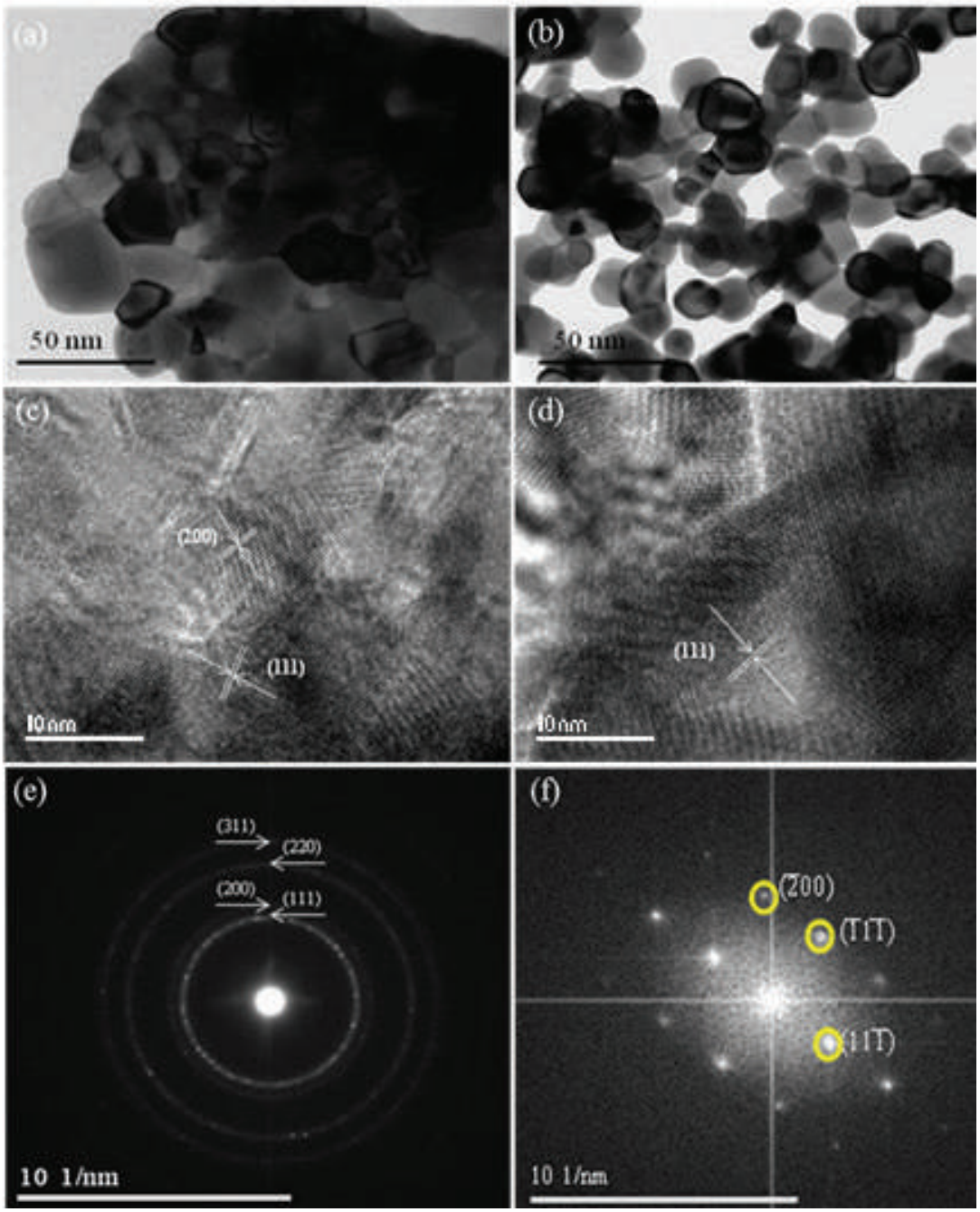

Figure 4. Morphology and crystal structure for gadolinium zirconate nanoparticle powders precipitated with 3 wt.% SDBS. (a) TEM images, (c) HRTEM images, and (e) SAED patterns with water solvent; and (b) TEM images, (d) HRTEM images, and (f) SAED patterns with ethanol solvent.

The equations of chemical reactions in the calcining process can be expressed as

$$Zr(OH)_4 \rightarrow ZrO_2 + 2H_2O \uparrow \quad 111\ ^\circ C, \tag{1}$$

$$2Gd(OH)_3 \rightarrow Gd_2O_3 + 3H_2O \uparrow \quad 628\ ^\circ C, \tag{2}$$

and

$$2ZrO_2 + Gd_2O_3 \rightarrow Gd_2Zr_2O_7 \quad 1065\ ^\circ C. \tag{3}$$

Agglomerate strength is related to the amount of hydrogen bond in the solvent, connecting the hydroxide precipitate through formation of bridges between adjacent particles. Figure 6 shows the solvent function in the model [28]. For hydroxide precipitated in the water, chemical bonds form between nanoparticles after further dehydration and sintering of precipitate, yielding hard agglomerates. However, the ethoxy group serves as the terminal group rather than bridging group, hence hydrogen bonds connecting neighboring particles don't form in the ethanol solvent and link particles together. The nonbridging hydroxyl groups in the ethanol solvent can obstruct bridge formation between adjacent particles and exhibit soft agglomerates.

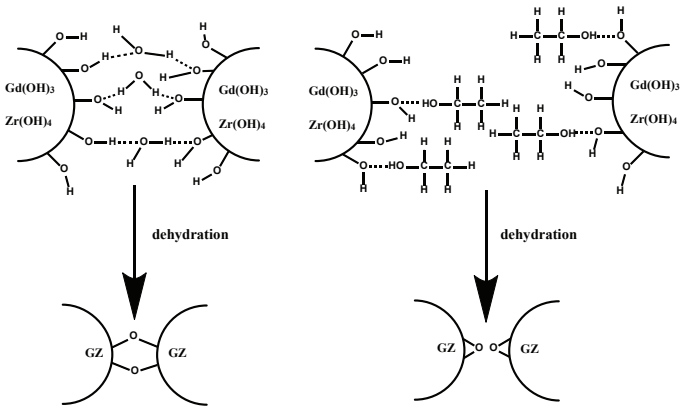

Figure 6. Agglomeration formation of GZ powders (a) hard agglomeration in the water solvent; (b) soft agglomeration in the ethanol solvent

Surfactant molecules adsorbing on the nanoparticle surfaces reduce the surface energy and reduce particle agglomeration, hence stabilizing growing particles and facilitating high dispersion. SDBS is an effective anion surfactant and can provide micelles to confine the reactions and provide electrostatic repulsion among the nanoparticles to increase their dispersion [29], as shown in Figure 7.

The dispersion of nanoparticles improves with the SDBS concentration from 2 to 3 wt.%, since surfactants adsorbing on the nanoparticle surfaces increase electrostatic repulsion when the total amount of surfactant is insufficient to cover all nanoparticles in the range below 3 wt.%. However, excess surfactant increases anion concentration in the solvent and hence reduces repulsion between nanoparticles, reducing surfactant effectiveness against GZ powders agglomeration. This is because surfactants can't absorb on the nanoparticles after surfactant concentration reaches critical micelle concentration. The agglomeration among the surfactants occurs, which reduces the repulsion between nanoparticles.

3.3. Grain growth kinetics

We investigated grain growth kinetics to estimate GZ nanoparticle grain size. Consider the (111) lattice plane half width as an example. GZ grain sizes prepared with 3 wt.% SDBS were estimated under different synthesis temperatures from the Scherrer equation

$$G=\frac{k\lambda}{B\cos\theta}, \quad (4)$$

where G is the mean grain size, λ = 0.15418 nm is the incident wavelength, k = 0.89 is the Scherrer constant, B is the diffractive peak full width at half maximum (FWHM), and θ is the diffractive angle.

Figure 8 shows that the calculated GZ powder grain size with 3 wt.% SDBS varies 7.4–36.6 nm between 900 and 1400 °C. GZ grain grows faster at the temperatures above 1200 °C since more lattice disorders and defects remain when calcining temperature is below 1200 °C. However, the GZ grain grows with fewer obstacles as lattice disorders decrease with the elevated temperature when calcining temperature is above 1200 °C. Well dispersed nanoparticles can increase material reactivity, which is good for TBC preparation, such as powder evaporation in the plasma plume and columnar structure formation with better fracture resistance.

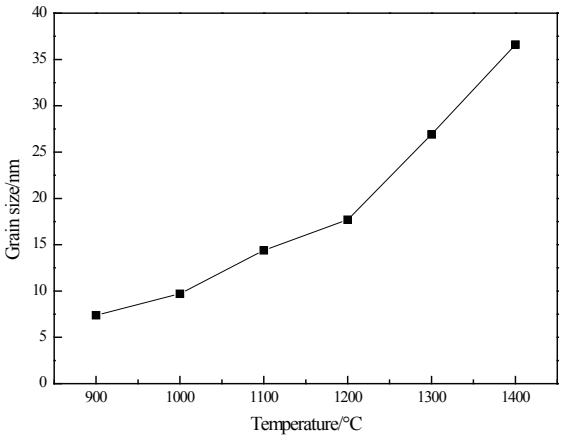

Figure 8. Grain size for gadolinium zirconate powder precipitated in ethanol solvent with 3 wt.% sodium dodecyl benzene sulfonate at different calcining temperatures.

Classically [30–32], grain growth rate and grain size are given as follows:

$$\frac{dG(t)}{dt}=\frac{c}{G(t)}, \quad (5)$$

where c is the constant related to the temperature, G and t

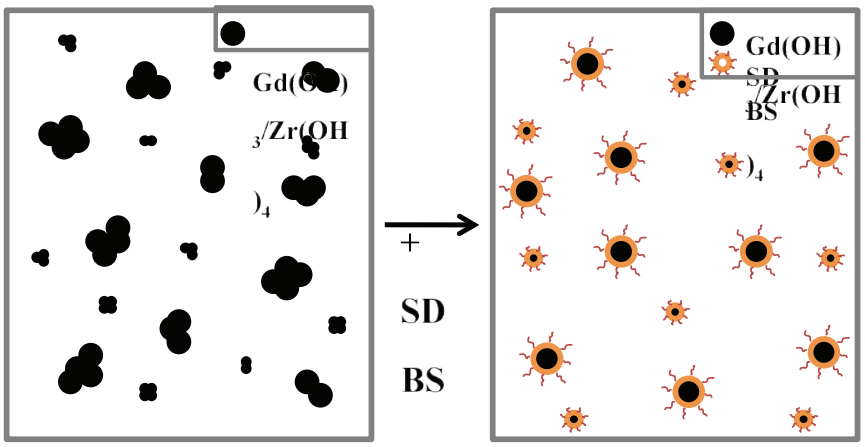

Figure 7. Dispersion mechanism model for sodium dodecyl benzene sulfonate (SDBS) on gadolinium zirconate (GZ) nanoparticles.

are the grain size and grain growth time, respectively,

$$c=\frac{A}{T}\exp(-\frac{Q}{RT}), \quad (6)$$

where T and R are the calcining temperature and gas constant, respectively; A and B are the temperature-irrelevant constants; and Q is the activation energy of grain growth. Then, grain growth is given as follows:

$$G(t)^2-G_o^2=2ct. \quad (7)$$

In this paper, $G_0 \approx 0$ and t = 2 h. Thus, equation (7) is deduced as

$$\ln G=B-\frac{Q}{2RT}. \quad (8)$$

Figure 9 confirms that ln$G$ is linear with respect to 1/T, and grain growth activation energy is deduced from the slope (Q/2R). The result shows grain growth activation energy of GZ powders is 86.5 kJ/mol (Q_l) for the powders calcined at the lower temperature (< 1200 °C), which is less than 148.4 kJ/mol (Q_h) for the powders calcined at higher temperature (> 1200 °C). At the lower temperature, GZ nanoparticles exhibit relatively smaller grain size and higher surface energy, indicating that GZ grains grow more easily with lower grain growth activation energy. Since crystallization is not fully developed, more disorders and defects are present, which lead to lower resistance of grain growth and lower grain growth activation energy at the lower calcining temperature. However, disorders and defects decrease when calcining temperature is above 1200 °C since crystallization has fully developed with relatively stable crystal structure, contributing to higher grain growth activation energy of GZ powders.

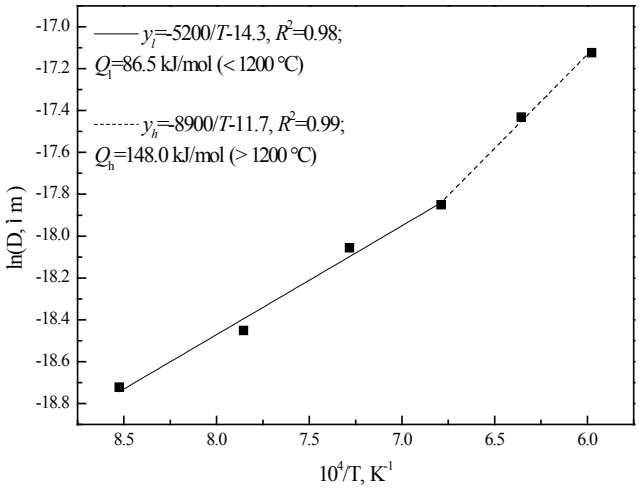

Figure 9. The relationship between lnD and 1/T for gadolinium zirconate.

Grain growth activation energy of GZ powders is greater than that of YSZ nanoparticles (13 kJ/mol) [33], supporting the stable GZ thermal properties and better sintering resistance. More pores can be retained in TBC ceramic layers, with better sintering resistance during thermal cycles. The retained pores will help relieve thermal stress concentration of ceramic layer in the thermal cycling and hence improve thermal cycling lifetime. In contrast, the amount of pores in the ceramic layer decreases with lower sintering resistance, decreasing CTE and increasing thermal mismatch in the interface of ceramic layer and underlying alloy. Thus, GZ application with greater sintering resistance will improve service life during thermal cycling.

4. Conclusions

This study successfully prepared gadolinium zirconate nanoparticles with defect fluorite structure by co-precipitation. As the calcining temperature increases from 900 °C to 1400 °C, the diffraction peak of the GZ powders in XRD patterns is sharper, which indicates the grain growth from 7.4 nm to 36.6 nm between 900 °C and 1400 °C for the nanoparticles with 3 wt.% SDBS. 1100 °C is the most appropriate calcining temperature to produce highly dispersed GZ nanoparticles.

Formation of GZ nanoparticles includes dehydration of zirconium hydroxide at approximately 483 °C, dehydration of gadolinium hydroxide at approximately 628 °C, and solid phase reaction at approximately 1065 °C. GZ nanoparticle dispersion can be readily accomplished by using ethanol and SDBS surfactant as reacting media. Ethanol efficiently obstructs the formation of hydrogen bond between hydroxide precipitates. SDBS surfactant further increases GZ nanoparticles dispersion, reaching optimal condition for 3wt.% SDBS.

Grain growth activation energy for GZ nanoparticles precipitated with 3 wt.% SDBS is calculated to be Q_l = 86.5 kJ/mol for GZ powders at the lower calcining temperature (< 1200 °C), which is less than Q_h = 148.4 kJ/mol for GZ powders at the higher calcining temperature (> 1200 °C), due to the decreased disorders and defects in the lattice and better developed crystallization at the higher calcining temperatures. Grain growth activation energy of GZ nanoparticles is greater than that of YSZ nanoparticles, indicating that GZ nanoparticles with 3 wt.% SDBS exhibit better sintering resistance and will be superior for preparing TBCs with longer service life.

Acknowledgements: This study was supported by the National Key Research and Development Program of China (grant 2017YFB0306100), the Natural Science Foundation of Hunan Province (grant 2018JJ2524), and the International scientific technological cooperation projects of China (grants 2015DFR50580 and 2013DFA31440).

References

[1] A Imaura, N Touran, RC Ewing. MgO-pyrochlore composite as an inert matrix fuel: Neutronic and thermal characteristics. Journal of Nuclear Materials 2009: 389: 341-350.

[2] J Zhang, J Lian, F Zhang, et al. Intrinsic structural disorder and radiation response of nanocrystalline $Gd_2(Ti_{0.65}Zr_{0.35})_2O_7$ pyrochlore. Journal of Physical Chemistry C 2010; 114: 11810-11818.

[3] J Lian, KB Helean, BJ Kennedy, et al. Effect of structure and thermodynamic stability on the response of lanthanide stannate pyrochlores to ion beam irradiation. Journal of Physical Chemistry B 2006; 110: 2343-2351.

[4] LG Tejuca, JLG Fierro, JMD Tascón. Structure and reactivity of perovskite-type oxides. Advances in Catalysis 1989; 36: 237-328.

[5] N Yamazoe, Y Teraoka. Oxidation catalysis of perovskites---relationships to bulk structure and composition (valency, defect, etc.). Catalysis Today 1990; 8: 175-199.

[6] Y Teraoka, K Torigoshi, H Yamaguchi, et al. Direct decomposition of nitric oxide over stannate pyrochlore oxides: relationship between solid-state chemistry and catalytic activity. Journal of Molecular Catalysis A: Chemical 2000; 155: 73-80.

[7] W Pan, SR Phillpot, C Wan, et al. Low thermal conductivity oxides. MRS Bulletin 2012; 37: 917-922.

[8] PK Schelling, SR Phillpot, RW Grimes. Optimum pyrochlore compositions for low thermal conductivity. Philosophical Magazine Letters 2004; 84: 127-137.

[9] XQ Cao, R Vassen, W Jungen, et al. Thermal stability of lanthanum zirconate plasma-sprayed coating. Journal of the American Ceramic Society 2001; 84: 2086-2090.

[10] L Wang, Y Wang, XG Sun, et al. Preparation and characterization of nanostructured $La_2Zr_2O_7$ feedstock used for plasma spraying. Powder Technology 2011; 212: 267-277.

[11] HY Jin, D Huang, Q Gao, et al. Synthesis of lanthanum zirconium oxide nanomaterials through composite-hydroxide-mediated approach. Materials Research Bulletin 2012; 47: 51-53.

[12] X Cao, R Vassen, W Jungen, et al. Thermal stability of lanthanum zirconate plasma-sprayed coating. Journal of the American Ceramic Society 2001; 84: 2086-2090.

[13] L Ling, X Qiang, F Wang, et al. Thermophysical properties of complex rare-earth zirconate ceramic for thermal barrier coatings. Journal of the American Ceramic Society 2010; 91: 2398-2401.

[14] ZG Liu, JH Ouyang, Y Zhou, et al. Structure and thermal conductivity of $Gd_2(TixZr_{1-x})_2O_7$ ceramics. Materials Letters 2008; 62: 4455-4457.

[15] L Ling, X Qiang, F Wang, et al. Thermophysical properties of complex rare-earth zirconate ceramic for thermal barrier coatings. Journal of the American Ceramic Society 2010; 91: 2398-2401.

[16] HM Zhou, DQ Yi, H Zhong. Dy and Ce co-doped $La_2Zr_2O_7$ ceramic powder used for thermal barrier coating. Journal of Inorganic Materials 2008; 23: 567-572.

[17] R Vassen, MO Jarligo, T Steinke, et al. Overview on advanced thermal barrier coatings, Surface and Coatings Technology 2010; 205: 938-942.

[18] MOD Jarligo, YS Kang, A Kawasaki. Physicochemical properties of single phase $La_2Zr_2O_7$ particle. Materials Transactions 2005; 46: 189-192.

[19] KK Rao, T Banu, M Vithal, et al. Preparation and characterization of bulk and nanoparticles of $La_2Zr_2O_7$ and $Nd_2Zr_2O_7$ by sol-gel method. Materials Letters 2002; 54: 205-210.

[20] NA Dhas, KC Patil. Combustion synthesis and properties of fine-particle rare-earth-metal zirconates, $Ln_2Zr_2O_7$. Journal of Materials Chemistry 1993; 3: 1289-1294.

[21] S Komarneni. Hydrothermal preparation of the low-expansion NZP family of materials. International Journal of High Technology Ceramics 1988; 4: 31-39.

[22] JA Labrincha, JR Frade, FMB Marques. $La_2Zr_2O_7$ formed at ceramic electrode/YSZ contacts. Journal of materials science 1993; 28: 3809-3815.

[23] S Wang, Y Zhai, X Li, et al. Co-precipitation synthesis of MgO-doped ZrO_2 nano powder. Journal of the American Ceramic Society 2006; 89: 3577-3581.

[24] MJ Readey, RR Lee, JW Halloran, et al. Processing and sintering of ultrafine MgO-ZrO_2 and (MgO, Y_2O_3)-ZrO_2 Powders. Journal of the American Ceramic Society 2010; 73: 1499-1503.

[25] H Guo, X Yang, T Xiao, et al. Structure and optical properties of sol-gel derived Gd_2O_3 waveguide films. Applied Surface Science 2004; 230: 215-221.

[26] S Xing, G Zhao. Morphology and thermostability of polypyrrole prepared from SDBS aqueous solution. Polymer Bulletin 2006; 57: 933-943.

[27] C Wang, Y Wang, L Wang, et al. Hydrothermal assisted synthesis and hot-corrosion resistance of nano lanthanum zirconate particles. Ceramics International 2014; 40: 3981-3988.

[28] MS Kaliszewski, AH Heuer. Alcohol interaction with zirconia powders, Journal of the American Ceramic Society 2010; 73: 1504-1509.

[29] X Cheng, X Zhang, H Yin, et al. Modifier effects on chemical reduction synthesis of nanostructured copper, Applied Surface Science 2006; 253: 2727-2732.

[30] CS Smith. Grains, phases, and interphases: an interpretation of microstructure. Metals Technology 1948; 175: 15-51.

[31] JE Burke. Some factors affecting the rate of grain growth in metals. Transactions of the American Institute of Mining and Metallurgical Engineers 1949; 180: 73-91.

[32] JE Burke, D. Turnbull. Recrystallization and grain growth. Progress in Metal Physics 1952;3: 220-292.

[33] S Shukla, S Seal, R Vij, et al. Reduced activation energy for grain growth in nanocrystalline yttria-stabilized zirconia, Nano Letters 2003;3: 397-401.

Viser Technology Pte. Ltd.
Research and Application of Materials Science
https://doi.org/10.33142/msra.v1i1.671

Research Article Open Access

Solvothermal Synthesis and Visible Photocatalytic Activity of $Zn_{0.4}Cd_{0.6}S/TiO_2$/Reduced graphene oxide Nanocomposite

Yongji Shi, Botao Sun, Xinwei Wang*, Deshuang Guo

School of Materials Science and Engineering, Changchun University of Science and Technology, Changchun 130022, China

***Corresponding Author:** Xinwei Wang, wxw4122@cust.edu.cn*

Abstract:
$Zn_{0.4}Cd_{0.6}S/TiO_2$/Reduced graphene oxide ($Zn_{0.4}Cd_{0.6}S/TiO_2$/RGO) nano-photocatalyst was synthe-sized by a facile solvothermal method. During the reaction, TiO_2 and $Zn_{0.8}Cd_{0.2}S$ nanoparticles were evenly dispersed across the surface of RGO, which enhanced response to visible light. The photocatalytic activity of as-synthesized $Zn_{0.4}Cd_{0.6}S/TiO_2$/RGO nanocomposite was studied by means of degrading methylene blue (MB) through the irradiation of visible light. Compared with other nanocomposites, the $Zn_{0.4}Cd_{0.6}S/TiO_2$/RGO nanocomposite showed the highest photocatalytic degradation efficiency (96%) and high stability, which was 5.4 times of photodegradation efficiency of pure TiO_2.

Keywords: *$Zn_{0.4}Cd_{0.6}S/TiO_2$/RGO; photocatalytic activity; visible light irradiation*

Citation: Y.J. Shi, et al., Solvothermal Synthesis and Visible Photocatalytic Activity of $Zn_{0.4}Cd_{0.6}S/TiO_2$/Reduced graphene oxide Nanocomposite. *Res Appl Mat Sci*, 2019,1(1): 35-38. https://doi.org/10.33142/msra.v1i1.671

1. Introduction

Semiconductor nanomaterial photocatalysts have attracted extensive attention in recent years due to its potential applications in hydrogen production and environment pollutant degradation [1,2]. Among them, oxide semiconductors have been mainly focused in photocatalysis. However, most oxide semiconductors such as TiO_2 (E_g>3.0 eV) mainly absorb ultraviolet light due to wide band gaps, which leads to low light utilization efficiency, and even the overall process being impractical [3-5]. As we all know, ultraviolet light only occupies about 4% of the solar spectrum, while visible light possesses 43% [6-9]. Therefore, increasing the availability of visible light for the practical application of photocatalyst still is now a challenge. $Zn_xCd_{1-x}S$, as a typical alloyed chalcogenide semiconductor, is a promising material due to its remarkable properties such as excellent electrical conductivity, valence bands at relatively negative potentials [10-13]. Therefore, it can be applied in photocatalysis, particularly in the visible light driven photocatalytic degradation of dyes. Furthermore, the rapid recombination of the excited electron-hole pairs is also an obstacle limiting the photocatalytic activity of catalysts. To solve the problem, various investigations have been carried out to improve the efficiency of the photocatalytic activity for single semiconductor [14-18].

Two-dimensional graphene as a promising material is widely used in the field of photocatalysis because of large specific surface area, and high carrier mobility [9]. The researchers have actively used different experimental methods or techniques to combine various semiconductor nanocomposites with graphene or reduced graphene oxide (RGO) to effectively improve their photocatalytic properties [19-21].

Therefore, TiO_2, $Zn_{0.4}Cd_{0.6}S/TiO_2$, $Zn_{0.4}Cd_{0.6}S/TiO_2$/RGO nanocomposites are synthesized via a facile solvothermal process. And these synthesized nanocomposites as typical photocatalysts is studied for their photodegradation activity, in which methylene blue (MB) is selected as probe material to determine the photocatalytic properties of synthesized nanocomposites under visible light irradiation.

2. Experimental

Photocatalysts synthesis: Since preliminary studies showed that the $Zn_xCd_{1-x}S$ nanoparticles (x=0.4) without graphite oxide (GO), namely, $Zn_{0.4}Cd_{0.6}S$ exhibited highest photodegradation activity [19]. GO was synthesized by classical modified Hummers experimental methods by natural graphite powder as carbon source [14]. The a typical synthesis process of the $Zn_{0.4}Cd_{0.6}S/TiO_2$/RGO nanocomposites is as follows: firstly, 329 mg $Zn(Ac)_2{\cdot}2H_2O$ (as Zn source), 100 mg $Cd(Ac)_2{\cdot}2H_2O$ (as Cd source), and 150 mg $TiCl_3$ (as Ti source) were added to 100 mL DMSO solution (as S source).Then, the suspension solution was vigorously stirred, and the 100 mg GO was put in it for 3 h. Afterward, the suspen-

sion solution was transferred into a Teflon-lined autoclave (200 mL) to react 12 h at 180℃. The reaction products were cleaned in turn by ethanol and deionized water, and then dried at 60℃ under vacuum. In addition, pure TiO_2 (or $Zn_{0.4}Cd_{0.6}S/TiO_2$) was also synthesized by the above method in the absence of GO (or $Zn_{0.4}Cd_{0.6}S$).

Characterization: X-ray diffraction (XRD) patterns of the powders were carried out by means of a Bruker D8 Advance X-ray diffractometer. To exhibt the morphologies and structures of samples, transmission electron microscope (TEM) (JOEL TEM-2010) with a field emission gun operating at 200 kV were employed. UV-vis spectrophotometer (Shimadzu, UV3600) was used to test UV-vis diffuse reflectance spectra and the concentration changes of MB of the samples.

Photocatalytic experiment: To evaluate photocatalytic activities of as-prepared samples, the degradation experiment for MB solution was carried out under visible light irradiation (λ > 420 nm). First, as-prepared samples (50 mg) was completely dispersed into 0.01 mM/100 mL MB solution. Then dispersed solution was continuously stirred with the help of 300W Xe lamp with light filter (420nm). And, the suspension was stirred in dark for 1 h to reach adsorption-desorption equilibrium. The reusability experiments of the sample were also tested by reusing the photocatalyst with the same experimental conditions.

3. Results and Discussion

Figure 1a shows the XRD patterns of TiO_2, $Zn_{0.4}Cd_{0.6}S$, and $Zn_{0.4}Cd_{0.6}S/TiO_2$/RGO nanocomposites. $Zn_{0.4}Cd_{0.6}S$ and TiO_2 exhibite sphalerite phase [JCPDS No. 05-0566] and anatase phase [JCPDS No.71-1166], respectively. $Zn_{0.4}Cd_{0.6}S/TiO_2$/RGO shows mixed crystal phase in which include correlative characteristic peaks of $Zn_{0.4}Cd_{0.6}S$ and TiO_2. Otherwise, no apparent peaks of RGO are observed in $Zn_{0.4}Cd_{0.6}S/TiO_2$/RGO nanocomposite because of its lower loading content and weak crystallization.

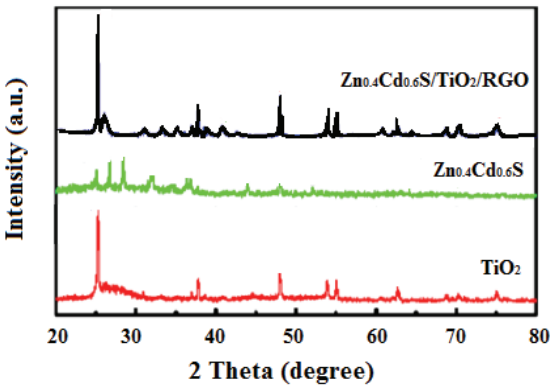

Figure 1. X-ray diffraction patterns of TiO_2, $Zn_{0.4}Cd_{0.6}S$, and $Zn_{0.4}Cd_{0.6}S/TiO_2$/RGO nanocomposites.

Figure 2 shows TEM image of $Zn_{0.4}Cd_{0.6}S/TiO_2$/RGO nanocomposite. From the image, we can see that $Zn_{0.4}Cd_{0.6}S$ and TiO_2 are nanospheres composing of smaller nanoparticles (Figure 2). Furthermore, these nanospheres are homogeneously scattered on RGO, indicating a strong interaction between these nanospheres of $Zn_{0.4}Cd_{0.6}S$, TiO_2 and RGO support to be propitious to catalytic activity.

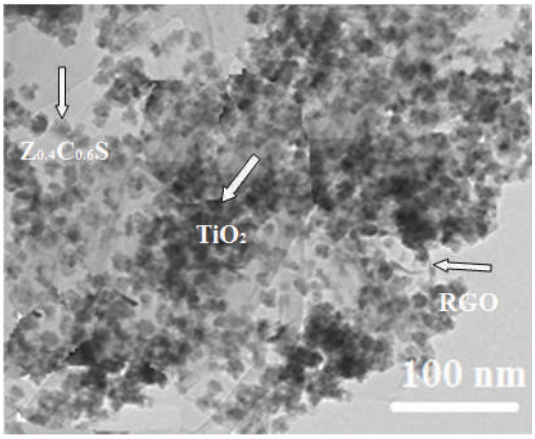

Figure 2. TEM image of $Zn_{0.4}Cd_{0.6}S/TiO_2$/RGO nanocomposite.

The UV-vis diffused reflectance spectra of TiO_2, $Zn_{0.4}Cd_{0.6}S/TiO_2$, and $Zn_{0.4}Cd_{0.6}S/TiO_2$/RGO nanocomposites are also shown in Figure 3. As can be seen, the onset wavelength for TiO_2, $Zn_{0.4}Cd_{0.6}S/TiO_2$, and $Zn_{0.4}Cd_{0.6}S/TiO_2$/RGO are ca.375 nm, 480 nm, and 550 nm respectively, corresponding to a bandgap of 3.31 eV, 2.58 eV, and 2.25 eV. We have estimated the bandgap energy of synthesized samples via extrapolating the straight portion of the $(ahv)^2$ versus photon energy (h) curve to a=0, in which a is absorption coefficient, h is Planck's constant, and v is frequency from the Kubelka-Munk function [15,16]. In addition, the absorbance intensity and region of $Zn_{0.4}Cd_{0.6}S/TiO_2$/RGO nanocomposite obviously enhance and broaden with the induction of RGO in the rang of visible light (>500 nm), which can be attributed to the full absorption of RGO for visible light. Therefore, we can infer that the prepared nanocomposites are suitable for visible-light response.

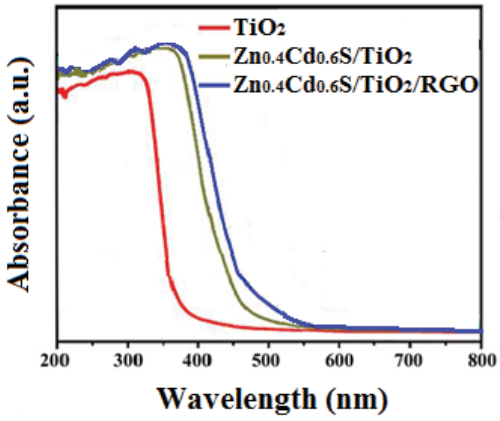

Figure 3. UV-vis diffuse reflectance spectra of TiO_2, $Zn_{0.4}Cd_{0.6}S/TiO_2$, and $Zn_{0.4}Cd_{0.6}S/TiO_2$/RGO nanocomposites.

The photocatalytic activities of $Zn_{0.4}Cd_{0.6}S$, $Zn_{0.4}Cd_{0.6}S/TiO_2$, and $Zn_{0.4}Cd_{0.6}S/TiO_2$/RGO nanocomposite are measured by the photodegradation of MB in aqueous solution under visible light irradiation (λ > 420 nm). The results are shown in Figure 4a and b, respectively. It is clear that the photocatalytic activity of pure $Zn_{0.4}Cd_{0.6}S$ is low, only 18% of MB is degraded. The photodegradation activities of $Zn_{0.4}Cd_{0.6}S/TiO_2$, and $Zn_{0.4}Cd_{0.6}S/TiO_2$/RGO nanocomposite are significantly enhanced compared with $Zn_{0.4}Cd_{0.6}S$. This indicate that higher photocatalytic activity is achieved due to intimate contact between $Zn_{0.4}Cd_{0.6}S$, TiO_2, and RGO, which is beneficial to interelectron transfer at the in-

terface. Notably, the photocatalytic activity of $Zn_{0.4}Cd_{0.6}S/TiO_2$/RGO nanocomposite increases quickly with induction of RGO, and which reaches the optimum activity, namely, the highest photodegradation efficiency 98 % after 120 min, which is 5.4 times that of pure $Zn_{0.4}Cd_{0.6}S$. Their photodegradation efficiency show as follows (Figure4a): $Zn_{0.4}Cd_{0.6}S/TiO_2$/RGO > $Zn_{0.4}Cd_{0.6}S/TiO_2$> $Zn_{0.4}Cd_{0.6}S$. In addition, to effectively demonstrate the degradation efficiency, the photodegradation kinetic process of $Zn_{0.4}Cd_{0.6}S/TiO_2$/RGO was also investigated for MB. The kinetic reacting process are fitted to a pseudo first-order reaction at low dye concentrations. This reaction follows the following formula:

$$\ln(C_0/C) = kt$$

C_0 is the initial concentration and C is the measured concentration, while k correspond to the photodegradation rate constant for the MB solution at reaction time t. As can be seen in Figure4b, the order of the k values is summarized as follows: $Zn_{0.4}Cd_{0.6}S/TiO_2$/RGO (k=0.0309)> $Zn_{0.4}Cd_{0.6}S/TiO_2$ (k=0.0295)> $Zn_{0.4}Cd_{0.6}S$ (k=0.0178). It is well coincident with the results presented in Figure4b. The photocatalytic enhancement of the $Zn_{0.4}Cd_{0.6}S/TiO_2$/RGO nanocomposite may be attributed to the introduction of both TiO_2 and RGO can simultaneously promote the migration of photogenerated electrons and holes from $Zn_{0.4}Cd_{0.6}S$ to space separated active sites on RGO and TiO_2, respectively, thus greatly suppressing their recombination and increasing their lifetime. Among them, TiO_2 nanoparticles can not only assemble the photogenerated holes from $Zn_{0.4}Cd_{0.6}S$ but also act as oxidation active sites to facillitate the irreversible consumption of the holes by sacrificial reagents, while the photogenerated electrons can be further enriched in the conduction band of $Zn_{0.4}Cd_{0.6}S$. In addition, the unique features of RGO nanosheets can effectively collect the photogenerated electrons from the conduction band of $Zn_{0.4}Cd_{0.6}S$, prolong the lifetime of the photogenerated electrons and enlarge the reduction reaction space, thus enhacing the photocatalytic activity of the $Zn_{0.4}Cd_{0.6}S/TiO_2$/RGO nanocomposite[22].

Furthermore, to evaluate the photostability, We have performed three cyclic photocatalytic degradation experiments for the $Zn_{0.4}Cd_{0.6}S/TiO_2$/RGO nanocomposite under the same experimental conditions (Figure 5). After 3 consecutive cycles, the photocatalytic degradation efficiency of $Zn_{0.4}Cd_{0.6}S/TiO_2$/RGO nanocomposite did not decrease significantly for the photodegradation of MB, which fully indicates that the structure of the $Zn_{0.4}Cd_{0.6}S/TiO_2$/RGO is optical stability and does not suffer from photocorrosion in the process of photodegradation.

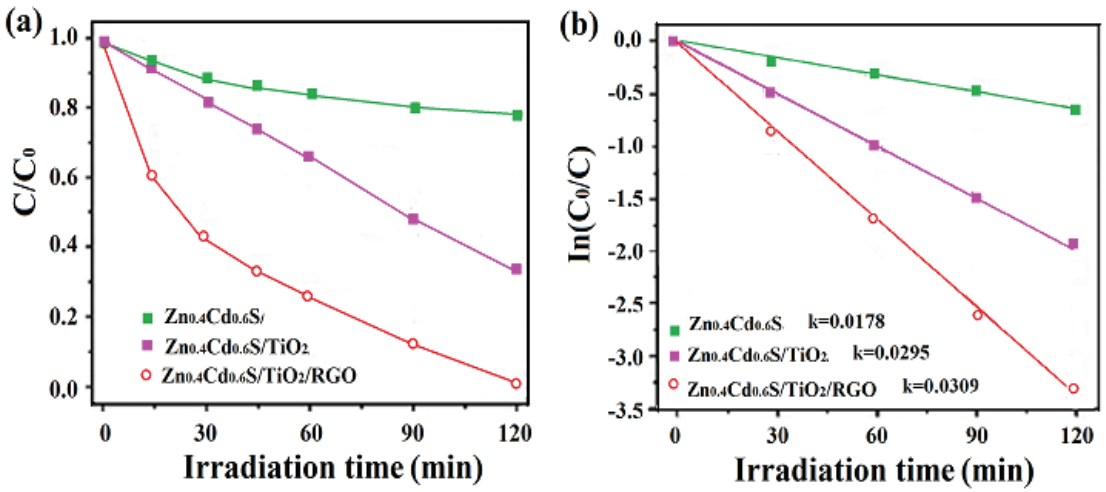

Figure 4. Photodegradation of MB (a) and the kinetics of photodegradation of MB (b) by different photocatalysts under visible light.

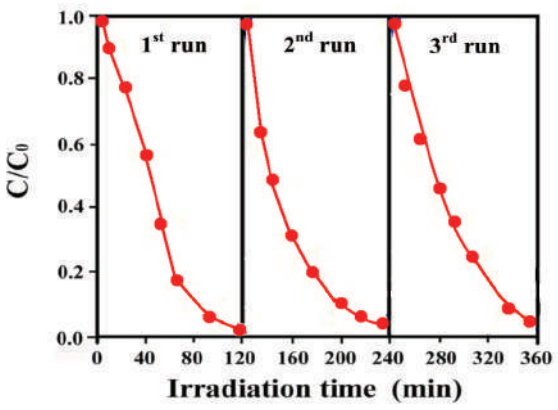

Figure 5. Recycling runs in the photodegradation of MB with $Zn_{0.4}Cd_{0.6}S/TiO_2$/RGO under the visible-light irradiation

4. Conclusions

we have developed a solvothermal method for the synthesis of $Zn_{0.4}Cd_{0.6}S/TiO_2$/RGO nano-photocatalysts, which showed that $Zn_{0.4}Cd_{0.6}S$ and TiO_2 nanoparticles can be distributed homogeneously on RGO surface. Besides, $Zn_{0.4}Cd_{0.6}S/TiO_2$ nanocomposite had much higher photocatalytic activity than pure TiO_2 nanoparticles for MB degradation. Among them, the $Zn_{0.4}Cd_{0.6}S/TiO_2$/RGO exhibited the highest photocatalytic activity, which is 5.4 times of pure TiO_2 nanoparticles.

Acknowledgments: This work is supported by the Innovation Foundation of Changchun University of Science and Technology (XJJLG-2016-11, XJJLG-2016-14) and the Foundation of NANOX (18JG01)..

References

[1] Woan K, Pyrgiotakis G, Sigmund W. Photocatalytic carbon-nanotube-TiO_2 composites[J]. Advanced Materials, 2009, 21(21): 2233-2239.

[2] Yu J, Zhang J, Jaroniec M. Preparation and enhanced visible-light photocatalytic H_2-production activity of CdS quantum dots-sensitized $Zn_{1-x}Cd_xS$ solid solution[J]. Green Chemistry, 2010, 12(9): 1611-1614.

[3] Cui L, Hui KN, Hui KS, et al. Facile microwave-assisted hydrothermal synthesis of TiO_2 nanotubes[J]. Materials Letters, 2012, 75: 175-178.

[4] Etacheri V, Di Valentin C, Schneider J, et al. Visible-light activation of TiO_2 photocatalysts: Advances in theory and experiments[J]. Journal of Photochemistry and Photobiology C: Photochemistry Reviews, 2015, 25: 1-29.

[5] Truong QD, Liu JY, Chung CC, et al. Design and fabrication of semiconductor photocatalyst for photocatalytic reduction of CO_2 to solar fuel[J]. Catal. Commun, 2012, 19: 8589.

[6] Li YX, Chen G, Wang Q, et al. Hierarchical ZnS-In_2S_3-CuS Nanospheres with Nanoporous Structure: Facile Synthesis, Growth Mechanism, and Excellent Photocatalytic Activity[J]. Advanced Functional Materials, 2010, 20(19): 3390-3398..

[7] Wang W, Germanenko I, El-Shall M S. Room-temperature synthesis and characterization of nanocrystalline CdS, ZnS, and $Cd_xZn_{1-x}S$[J]. Chemistry of Materials, 2002, 14(7): 3028-3033.

[8] Xing CJ, Zhang YJ, Yan W, et al. Band structure-controlled solid solution of $Cd_{1-x}Zn_xS$ photocatalyst for hydrogen production by water splitting[J]. International Journal of Hydrogen Energy, 2006, 31(14): 2018-2024.

[9] Xu X, Lu RJ, Zhao XF, et al. Novel mesoporous $Zn_xCd_{1-x}S$ nanoparticles as highly efficient photocatalysts[J]. Applied Catalysis B: Environmental, 2012, 125: 11-20.

[10] Wu HQ, Yao YZ, Li WT, et al. Microwave-assisted synthesis of $Zn_xCd_{1-x}S$ -MWCNT heterostructures and their photocatalytic properties[J]. Journal of Nanoparticle Research, 2011, 13(5): 2225-2234.

[11] Li WJ, Li DZ, Meng SG, et al. Novel Approach To Enhance Photosensitized Degradation of Rhodamine B under Visible Light Irradiation by the $Zn_xCd_{1-x}S$ /TiO_2 Nanocomposites[J]. Environmental science & technology, 2011, 45(7): 2987-2993.

[12] Novoselov KS, Geim AK. The rise of graphene[J]. Nat. Mater, 2007, 6(3): 183-191.

[13] Xiang Q, Yu J, Jaroniec M. Graphene-based semiconductor photocatalysts[J]. Chemical Society Reviews, 2012, 41(2): 782-796.

[14] Ping JF, Fan ZX, Sindoro M, et al. Recent advances in sensing applications of two - dimensional transition metal dichalcogenide nanosheets and their composites[J]. Advanced Functional Materials, 2017, 27(19): 1605817.

[15] Lu QP, Yu YF, Ma QL, et al. 2D Transition- metal- dichalcogenide- nanosheet- based composites for photocatalytic and electrocatalytic hydrogen evolution reactions[J]. Advanced Materials, 2016, 28(10): 1917-1933.

[16] An X, Jimmy C Y. Graphene-based photocatalytic composites[J]. Rsc Advances, 2011, 1(8): 1426-1434.

[17] Lou SY, Wang YQ, Zhou SM, et al. A facile method to immobilize $Zn_xCd_{1-x}S$ nanocrystals on graphene nanoribbons[J]. Materials Letters, 2012, 67(1): 169-172.

[18] Zhang J, Yu JG, Jaroniec M, et al. Noble metal-free reduced graphene oxide -$Zn_xCd_{1-x}S$ nanocomposite with enhanced solar photocatalytic H_2-production performance[J]. Nano letters, 2012, 12(9): 4584-4589.

[19] Wang XW., Tian HW., Cui XQ., Zheng W.T., Liu Y.C., "One-pot hydrothermal synthesis of mesoporous $Zn_xCd_{1-x}S$/reduced graphene oxide hybrid material and its enhanced photocatalytic activity", Dalton Trans., 2014,43:12894-12903.

[20] Zhou MH, Yu JG. Preparation and enhanced daylight -induced photocatalytic activity of C, N, S- tridoped titanium dioxide powders[J]. Journal of Hazardous Materials, 2008, 152: 1229–1236

[21] Kubelka, P. J. New contributions to the optics of intensely light-scattering materials. Part I Paul Kubelka [J]. Journal of the Optical Society of America, 1948, 38(5): 448-457.

[22] Zhang J, Qi LF, Ran JR, Yu JG, Qiao SZ. Ternary NiS/$Zn_xCd_{1-x}S$/reduced graphene oxide nanocomposites for enhanced solar photocatalytic H_2-production activity [J]. Advanced Energy Materials., 2014, 4: 1301925-1301930.

Viser Technology Pte. Ltd.
Research and Application of Materials Science
https://doi.org/10.33142/msra.v1i1.672

Research Article Open Access

One Novel Zn(II) Nitro-containing Metal Organic Framework for Dye-Adsorption and Photo Degradation

Weiqi Li[1], Xieao Du[1], Haiyan He[1*]

[1] College of Mechanics and Materials, Hohai University, Nanjing, Jiangsu, 210098, China

***Corresponding Author:** H.Y. He; West Focheng Road No. 8, Hohai University, Nanjing, Jiangsu, 210098, China; email address: he.haiyan@hhu.edu.cn*

Abstract:
A novel metal-organic framework [$Zn_{0.5}(L_1)(4,4'\text{-Bpy})_{0.5}$], (**HU21**, HU for Hohai University, L_1 = 4-hydroxy-3-nitrobenzoic acid, 4,4'-bipyridine = 4,4'-Bpy), has been isolated through hydro-thermal reaction. Single-crystal X-ray diffraction reveals the compound features a 1D fishbone-like chain. A fast adsorption rate of methylene blue with **HU21** was observed in the dark, but under irritation the degradation rate of the dye was obviously increased. The degradation of methylene blue dye reached 248 mg/g under light irritation, and the photocatalytic activity reached 96.1%.

Keywords: *Metal organic frameworks; Hydrothermal reaction; Photocatalyst; Dye adsorption;*

Citation: W.Q. Li, X.A. Du, H.Y. He, One Novel Zn(II) Nitro-containing Metal Organic Framework for Dye-Adsorption and Photo Degradation. *Res Appl Mat Sci*, 2019,1(1): 39-44. https://doi.org/10.33142/msra.v1i1.672

1. Introduction

In the past decades, environmental pollution has become more and more serious, especially the pollution of water resources. If it is allowed to continue to develop, it will endanger the survival of human beings, so the treatment of water pollution must arouse human attention. In the past, there were mainly physical, chemical and biological methods in water pollution treatment. Physical method is cheaper, but the treatment effect is poor. Chemical treatment is effective, but the price is high. Biological process usually takes a lot of time and other microorganisms to treat wastewater, and the space occupied in the process of treatment is also a waste of space. Therefore, in the treatment of sewage, it is often not a single method, but a combination of various methods. Recently, a new kind of material, metal-organic skeleton, has come into people's vision. Since the emergence of organometallic skeleton, it has attracted the attention of many researchers. Metal atoms and organic ligands in MOFs are bound by coordination bonds, and different ligands are bound by covalent bonds, so that metal atoms and organic ligands can be linked into chains and finally form skeleton structures. Because of its large specific surface area, adjustable pore size and structure, MOFs can also have various properties by replacing metal ions.[1-3] At present, MOFs have good applications in gas adsorption, drug sustained release and supercapacitors.[4-7] The pore size of MOFs can be adjusted by replacing larger similar ligands or using structural regulators when materials with smaller pore size are obtained.[8, 9] Because of this property of MOFs, MOFs can be used as dye adsorbents. Luo et al. constructed a kind of Zn-MOFs, which can absorb anodic dyes.[10] Chen et al. has constructed a series of MOFs based on lanthanide metals, which have high adsorption rates for dye molecules.[11] Yan et al. constructed three kinds of Co-MOF for adsorbing cationic dyes, and the integrity of the skeleton was not destroyed after adsorption. [12] ZN-MOF constructed by Zhang et al. has good adsorption capacity for MB because of its suitable pore size.[13]By adjusting their structure, they can absorb larger or different dyes. Zha et al. By introducing highly branched alkanes, the modified MOFs adsorbed 99% Rhodamine 6G, while the original MOFs only adsorbed 52%.[14] Xu et al. synthesized a composite material on the basis of ZIF-8, and its adsorption rate of methyl violet was greatly improved. [15]However, not all MOFs have large channels, so the adsorption of organic dyes by these MOFs mainly makes them immobilized on the surface of MOFs. Han et al. constructed a new type of MOFs, which adsorbed Congo red by hydrogen bond and electrostatic interaction. [16] But this way of adsorbing organic dyes will face the problem of easy desorption. Later, it was found that MOFs exhibited good photocatalytic activity under ultraviolet and LED light. Luo et al. constructed two kinds of Zn-MOF, which showed excellent catalytic activity for methyl orange, methylene blue and Rhodamine B under UV irradiation.[17] A binuclear Co-MOF constructed by Xiao et al. has photocatalytic activity on RhB under UV irradia-

tion.[18] The porous structure of MOFs enables active sites to be exposed to a greater extent, thus making the contact between reactants and active sites easier. MOFs have properties similar to semiconductors, so under the action of light, MOFs can produce electrons and holes, which can catalyze redox reaction. When MOFs are used to adsorb photocatalytic dyes, the essence is that MOFs generate electrons and holes under photocatalytic conditions. These electrons and holes catalyze the reduction of O_2 to $\cdot O^{2-}$, then $\cdot O^{2-}$ is converted to ·OH, and ·OH can decompose organic dyes into CO_2 and H_2.[19-21] Based on this principle, Xiao et al. studied the effect of external catalyst H_2O_2 on photocatalysis, and made good progress.[22]

In this paper, we present the synthesis of one novel zinc-based metal organic framework **HU21** $[Zn_{0.5}(L_1)(4,4'\text{-Bpy})_{0.5}]$, single-crystal X-ray diffraction reveals that the complex features one-dimensional fishbone chains and finally three-dimensional superamolecular structure. This Zn-MOF compound displays interesting dye adsorption and photocatalytic performance. The degradation of methylene blue dye reached 248 mg/g under light irritation, and the photocatalytic activity reached 96.1%.

2. Experimental section

2.1 Materials and Synthesis

All medicines were used directly after commercial purchase without further purification.

Synthesis of HU21 $[Zn_{0.5}(L_1)(4,4'\text{-Bpy})_{0.5}]$:A mixture of 20mg of $Zn(NO_3)_2{\cdot}6H_2O$, 10 mg of 4-hydroxy-3-nitrobenzoic acid (L_1) and 5 mg of 4,4'-bipyridine (4,4'-Bpy) was suspended in 5 ml distilled water, and heated in a teflon-lined steel bomb at120°C for 48 hours. The resulting colorless crystals were collected and dried at 50℃(yield: 57%).The synthesis of HU21 formula is :

2.2 Adsorption Test of Organic Dyes

$$\frac{1}{2}Zn(NO_3)_2\cdot 6H_2O+\frac{1}{2}4,4'-Bpy+L_1=[(Zn_{0.5}(L_1)(4,4'-Bpy)_{0.5})]+3H_2O+2HNO_3 \quad (a)$$

2.2.1Adsorption performance test of methyl orange dyes

Firstly, the standard curve of methyl orange was established, and then 5 mg HU21 crystal was weighed, 40 mg/L methyl orange dye solution was collocated, 50 mL solution was taken for adsorption test, HU21 was put under visible light for adsorption performance test, and the absorbance test was carried out every 30 minutes with ultraviolet spectrophotometer, and the amount of adsorption was calculated. According to the relationship between dye concentration and absorbance, the absorbance can be expressed by adsorbent.[23]The calculation formula is as follows:

$$Q=\frac{V(C_0-C_e)}{m} \quad (b)$$

Among them, Q is the amount of adsorption to be calculated, V is the volume of organic dye solution, C_0 is the initial concentration of dye solution, C_e is the concentration of dye solution after a certain time, and M is the mass of MOFs.

After that, the same volume of methyl orange dye solution was taken and put into 5 mg HU21 crystal. Photocatalysis was carried out under xenon lamp. Absorption was measured after a certain time interval. The amount of adsorption was calculated. At the same time, the photocatalytic activity under xenon lamp was calculated. The calculation formula was as follows:

$$D=\frac{C_0-C_e}{C_0}\times 100\% \quad (c)$$

Among them, D is the catalytic rate to be calculated, C_0 is the initial concentration of dye solution, C_e is the concentration of dye solution after a certain time.

2.2.2Adsorption Performance Test of Methylene Blue

Firstly, the standard curve of methylene blue was established, then the HU21 crystal was weighed 5 mg, the methylene blue dye solution was 25 mg/L, the solution was 50 mL for adsorption test, the adsorption performance was tested under visible light, and the absorbance was tested with ultraviolet spectrophotometer every 30 minutes, and the amount of adsorption was calculated.

After that, methylene blue dye solution of the same volume was taken, and 5 mg HU21 crystal was put into it. Photocatalysis was carried out under xenon lamp. Absorption test was carried out after a certain period of time. The amount of adsorption was calculated, and the photocatalytic efficiency under xenon lamp was calculated.

3.Results and discussion

3.1 Crystal structure of HU21

Single-crystal X-ray diffraction analysis revealed that HU21 crystallizes in monoclinic space group and a one-dimensional structure. The asymmetric unit consists of one half zinc ion, one L_1 ligand, and one half 4,4'-Bpy molecule, as shown in Figure 1. The central metal Zn is 4-coordinated as a square by two oxygen atoms from two L_1 ligand and two nitrogen from two 4,4'-bipyridine ligands, respectively. Both the nito- and hydroxyl- functional groups of L_1 ligands do not involve the coordination, thus L_1 acts as the stick of the fishbone structure and prevent the vertical extension of the whole configuration.

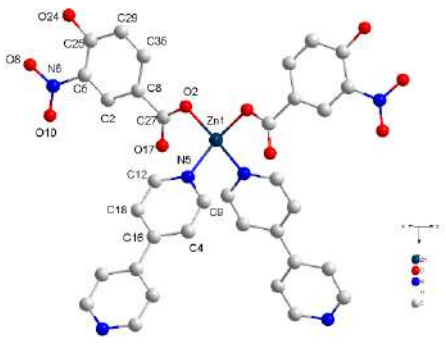

Figure 1 The asymmetric unit

Figure 2 shows the chain structure of HU21. It can be seen that HU21 forms a chain structure through the alternate connection of asymmetric units.

Shown in Figure 3, the final superamolecular structure is formed by the π-π stacking interaction of benzene rings between L_1 ligands.

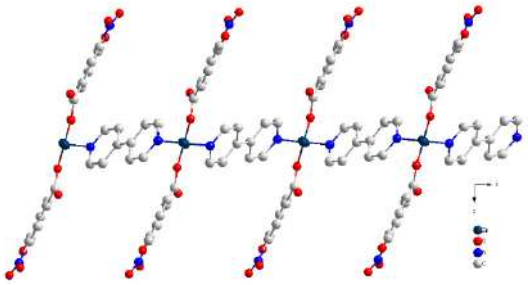

Figure 2 The chain structure of HU21

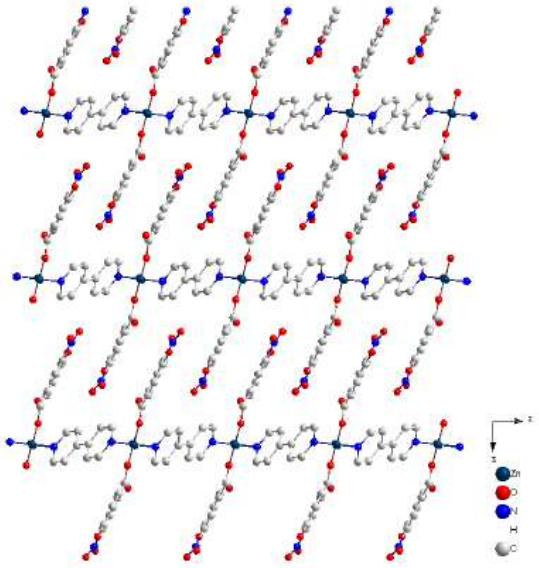

Figure 3 The three-dimensional structure of HU21

Table 1 shows the Crystallographic data of HU21.

Conpound	$[Zn_{0.5}(L1)(4,4'\text{-}Bpy)_{0.5}]$
Formula sum	C24 H16 N4 O10 Zn
Formula weight	585.78 g/mol
Crystal system	monoclinic
Space-group	I 1 2/c 1 (15)
a(Å)	14.0304(4)
b(Å)	7.2705(2)
c(Å)	22.4588(6)
α(°)	90
β(°)	92.46(0)
γ(°)	90
Cell volume(Å^3)	2288.86(23)
z	4
Calc. density	1.6998 g/cm^3
F(000)	1192
2θmax(°)	70.457
index ranges (h, k, l)	-16/16
	-7/8
	-16/26
reflections collected	4184
R_{int}	0.0293
data/restraints/parameters	2031/0/178
GOF (F^2)	1.086
R_1, wR_2 [I ≥2σ (I)]	0.0565/0.1866
R_1, wR_2 (all date)	0.0598/0.1910

3.2 Characterization of Adsorption Property

3.2.1Characterization of adsorption properties of methyl orange

Shown as Fig 4, the adsorption of methyl orange by **HU21** under visible light and under xenon lamp irradiation. It can be seen that there is no adsorption effect when under visible light. Compared with visible light, HU21 adsorbs methyl orange better, but it can not absorb it completely.

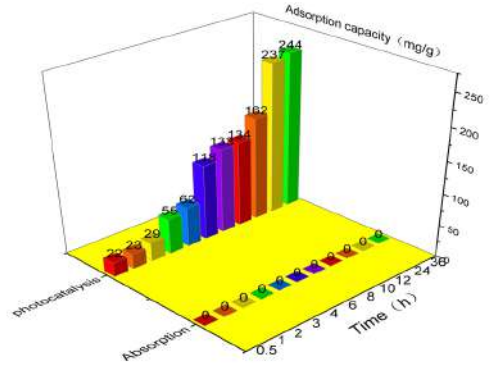

Figure.4(a)The adsorption capacity of **HU21** to methyl orange.

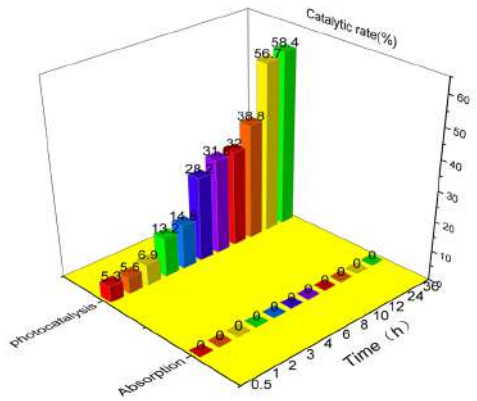

Figure .4(b)The catalytic rate of **HU21** to methyl orange.

Figure 5 (a) is a change in the absorbance of methyl orange after HU21 adsorbs methyl orange under xenon lamp irradiation.

Figure 5 (b) shows the catalytic activity of HU21 for methyl orange adsorption under xenon lamp irradiation. At 24 hours, the catalytic rate reached 56%. Methyl orange is mainly decomposed into CO_2 and hydrogen peroxide by OH produced by MOFs catalysis under the strong illumination of xenon lamp, which makes dye catalytic degradation.It can be seen that the absorption wavelength of the chromogenic group of methyl orange in the figure is 460 nm. With the progress of photocatalysis, the absorption peak of the chromogenic group widens gradually, and the absorption wavelength moves to the left gradually. It shows that the chromogenic group is degraded by HU21 catalysis, while the absorption near 300 nm rises because the decomposition product CO_2 dissolves in water. It can be seen from the figure that the slope transformation of the catalytic rate curve of methyl orange is more frequent, which reflects the variation of the rate of holes and electrons produced by **HU21**.

3.2.2Characterization of Adsorption Properties of Methylene Blue

Figure 6 shows the adsorption of methylene blue by HU21 under visible light and under xenon lamp irradiation. It can be seen that there is no adsorption effect when under visible light.

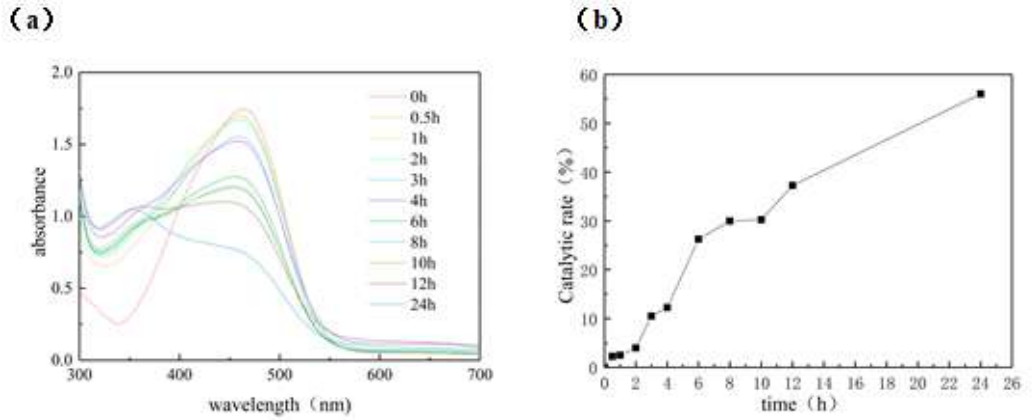

Figure 5 The absorbance of methyl orange after HU21 adsorbs methyl orange under xenon lamp irradiation(a).the catalytic activity of HU21 for methyl orange adsorption under xenon lamp irradiation. (b)

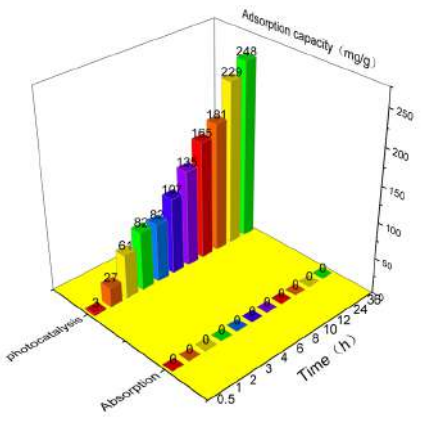

Figure .6(a) The adsorption capacity of **HU21** to methylene blue.

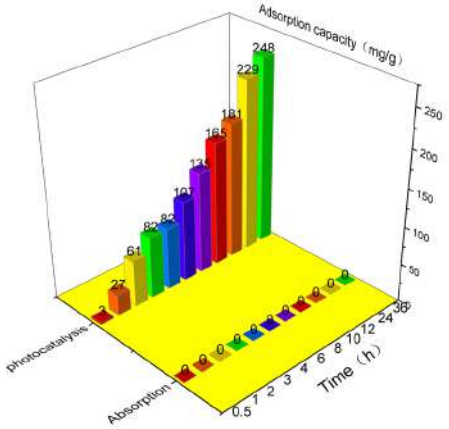

Figure .6(b) The catalytic rate of **HU21** to methylene blue.

Figure 7(a) is the change of absorbance of methylene blue after HU21 adsorbs methylene blue under xenon lamp irradiation. It can be seen that with the photocatalysis, the maximum absorption peak becomes wider and the absorption wavelength moves to the left gradually, which indicates that the chromogenic group of methylene blue is photocatalytically degraded by HU21, and the absorption wavelength shifts to the left with the gradual photocatalytic degradation. The increase of absorbance near 300 nm is due to the dissolution of decomposition product CO_2 in water.

Figure 7(b) shows the catalytic activity of HU21 for methylene blue adsorption under xenon lamp irradiation. It can be seen that compared with the adsorption under visible light, the adsorption effect is greatly improved, the catalytic rate reaches 50% in only 8 hours, and after 32 hours, the catalytic rate is close to 100%, showing superior photocatalytic performance. At the same time, we can also see that the slope of photocatalytic curve of methylene blue is larger in the early stage, and decreases grad-

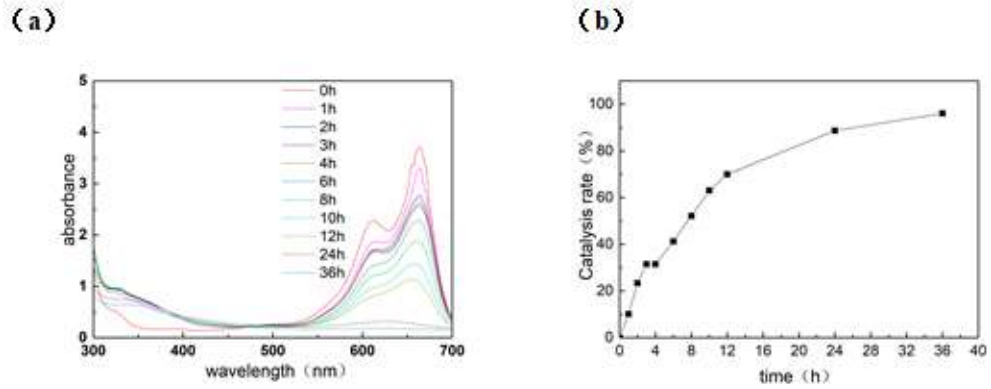

Figure 7 the absorbance of methylene blue after HU21 adsorbs methylene blue under xenon lamp irradiation.(a) the catalytic activity of **HU21** for methylene blue adsorption under xenon lamp irradiation. (b)

ually with the time of photocatalysis.

Compared with the adsorption of methylene orange and methylene blue, it can be seen that although the photocatalytic rate of methylene blue dyes is higher, the adsorption amount of methylene blue and methylene orange is equal.

4.Conclusions

In this paper, we present a new structure of a MOFs **HU21** $[Zn_{0.5}(L_1)(4,4'\text{-Bpy})_{0.5}]$ based on 4-hydroxy-3-nitrobenzoic acid and 4,4'-bipyridine skeleton, and characterize its dye adsorption and photocatalytic activity. Due to the poor porosity of **HU21**, hardly dye adsorption of methyl orange and methylene blue can be investigated in the dark. Under the strong illumination of xenon lamp, Zn-MOF depredates dye molecules to small molecules CO_2 and H_2O. Although the adsorption amount of methylene blue and methyl orange were almost the same, **HU21** displays a high photocatalytic rate on methylene blue.

References

[1]. Eddaoudi M, Kim J, Rosi N, Vodak D, Wachter J, O'Keeffe M, Yaghi OM: Systematic design of pore size and functionality in isoreticular MOFs and their application in methane storage. *Science* 2002, 295(5554):469-472.

[2]. Furukawa H, Ko N, Go YB, Aratani N, Choi SB, Choi E, Yazaydin AO, Snurr RQ, O'Keeffe M, Kim J *et al*: Ultrahigh Porosity in Metal-Organic Frameworks. *Science* 2010, 329(5990):424-428.

[3]. Millward AR, Yaghi OM: Metal-organic frameworks with exceptionally high capacity for storage of carbon dioxide at room temperature. *Journal of the American Chemical Society* 2005, 127(51):17998-17999.

[4]. Jin J-C, Wu J, Liu W-C, Ma A-Q, Liu J-Q, Singh A, Kumar A: A new Zn(II) metal-organic framework having 3D CdSO4 topology as luminescent sensor and photocatalyst for degradation of organic dyes. *New Journal of Chemistry* 2018, 42(4):2767-2775.

[5]. Liu K, Deng L, Li H, Bao Y, Xiao Z, Li B, Zhou Q, Geng Y, Wang L: Two isostructural Co/Ni fluorine-containing metal-organic frameworks for dye adsorption and supercapacitor. *Journal of Solid State Chemistry* 2019, 275:1-7.

[6]. Wu Y, Wu J, Luo Z, Wang J, Li Y, Han Y, Liu J: Fluorescence detection of Mn2+, Cr2O72- and nitroexplosives and photocatalytic degradation of methyl violet and rhodamine B based on two stable metal-organic frameworks. *Rsc Advances* 2017, 7(17):10415-10423.

[7]. Xue Z, Zhu M, Dong Y, Feng T, Chen Z, Feng Y, Shan Z, Xu J, Meng S: An integrated targeting drug delivery system based on the hybridization of graphdiyne and MOFs for visualized cancer therapy. *Nanoscale* 2019.

[8]. Rowsell JLC, Yaghi OM: Effects of functionalization, catenation, and variation of the metal oxide and organic linking units on the low-pressure hydrogen adsorption properties of metal-organic frameworks. *Journal of the American Chemical Society* 2006, 128(4):1304-1315.

[9]. Li Z-X, Hu T-L, Ma H, Zeng Y-F, Li C-J, Tong M-L, Bu X-H: Adjusting the Porosity and Interpenetration of Cadmium(II) Coordination Polymers by Ligand Modification: Syntheses, Structures, and Adsorption Properties. *Crystal Growth & Design* 2010, 10(3):1138-1144.

[10]. Luo X, Mai Z, Lei H: A bifunctional luminescent Zn(II)-organic framework: Ionothermal synthesis, selective Fe(III) detection and cationic dye adsorption. *Inorganic Chemistry Communications* 2019, 102:215-220.

[11]. Chen W, Fan R, Wang P, Dong Y, Yang Y: Multifunctional Lanthanide-Based Metal-Organic Frameworks with a Polyheterotopic Ligand: Doped with Ytterbium(III) for Luminescence Enhancement and Selective Dye Adsorption. *Chemistry-an Asian Journal* 2018, 13(16):2126-2134.

[12]. Yan W, Han L-J, Jia H-L, Shen K, Wang T, Zheng H-G: Three Highly Stable Cobalt MOFs Based on "Y"-Shaped Carboxylic Acid: Synthesis and Absorption of Anionic Dyes. *Inorganic Chemistry* 2016, 55(17):8816-8821.

[13]. Zhang J, Li F, Sun Q: Rapid and selective adsorption of cationic dyes by a unique metal-organic framework with decorated pore surface. *Applied Surface Science* 2018, 440:1219-1226.

[14]. Zha Q, Sang X, Liu D, Wang D, Shi G, Ni C: Modification of hydrophilic amine-functionalized metal-organic frameworks to hydrophobic for dye adsorption. *Journal of Solid State Chemistry* 2019, 275:23-29.

[15]. Xu W, Chen Y, Kang J, Li B: Fabrication of ZIF-8 based on lignin with high yield for dye removal from water. *Journal of the Iranian Chemical Society* 2019, 16(2):385-392.

[16]. Han L-J, Ge F-Y, Sun G-H, Gao X-J, Zheng H-G: Effective adsorption of Congo red by a MOF-based magnetic material. *Dalton Transactions* 2019, 48(14):4650-4656.

[17]. Luo Q, Zhu Z, Fan C, Zong Za, Xu C, Bi C, Fan Y: Two dia isomorphic Zn-MOFs based on two isomeric semi-rigid aromatic tetracarboxylate acids: Syntheses and properties. *Journal of Molecular Structure* 2019, 1188:57-61.

[18]. Xiao GB, Yao XQ, Xie H, Ma HC, Yan PJ, Qin DD: Dinuclear cobalt-based pillar-layered-like MOF as an electrode material for supercapacitor and photocatalysis activity. *Polyhedron* 2019, 162:39-44.

[19]. Qian L-L, Blatov VA, Wang Z-X, Ding J-G, Zhu L-M, Li K, Li B-L, Wu B: Sonochemical synthesis and characterization of four nanostructural nickel coordination polymers and photocatalytic degradation of methylene blue. *Ultrasonics Sonochemistry* 2019, 56:213-228.

[20]. Yu D, Li L, Wu M, Crittenden JC: Enhanced photocatalytic ozonation of organic pollutants using an iron-based metal-organic framework. *Applied Catalysis B-Environmental* 2019, 251:66-75.

[21]. Zhu H, Liu D, Li Y-H, Cui G-H: Syntheses, crystal structures, and photocatalytic properties of two zinc(II) coordination polymers based on dicarboxylates and flexible bis(benzimidazole) ligands. *Polyhedron* 2019, 167:44-50.

[22]. Xiao J-D, Shang Q, Xiong Y, Zhang Q, Luo Y, Yu S-H, Jiang H-L: Boosting Photocatalytic Hydrogen Production of a Metal-Organic Framework Decorated with Platinum Nanoparticles: The Platinum Location Matters. *Angewandte Chemie-International Edition* 2016, 55(32):9389-9393.

[23]. Huo M, Yang W, Zhang H, Zhang L, Liao J, Lin L, Lu C: A new POM-MOF hybrid microporous material with ultrahigh thermal stability and selective adsorption of organic dyes. *Rsc Advances* 2016, 6(112):111549-111555.

Viser Technology Pte. Ltd.
Research and Application of Materials Science
https://doi.org/10.33142/msra.v1i1.667

Review Article Open Access

Tannin Resins for Wood Preservatives: A Review

Jinxing Li[1], Bin Li[1], Jun Zhang[1], Xiaojian Zhou[1,2,3,*]

[1] Yunnan Provincial Key Laboratory of Wood Adhesives and Glued Products, Southwest Forestry University, Kunming, 650224, China
[2] Key Lab for Forest Resources Conservation and Utilisation in the Southwest Mountains of China, Southwest Forestry University, Ministry of Education, Kunming 650224, China

***Corresponding Author:** Xiaojian Zhou, No. 300, Bailongsi, Panlong district, Kunming, 650224, Yunnan Province, China, xiaojianzhou@hotmail.com*

Abstract:
Tannins and wood preservatives, in this article, are briefly introduced at beginning. The research and application progress on tannin resins for wood preservatives at home and abroad are reviewed. The significance and development prospects of research on tannins for wood preservatives are prospected.

Keywords: *Wood preservatives; Tannin resins; Research progress*

Citation: J.X. Li et al., Tannin Resins for Wood Preservatives: A Review. *Res Appl Mat Sci*, 2019,1(1): 45-47. https://doi.org/10.33142/msra.v1i1.667

1. Introduction

Wood is one of the popular building materials at home and abroad at all times. In the era of steel and concrete, wood structure has a special charm. However, wood products are vulnerable to microbial damage during storage and use; cause a serious waste of resources, affecting their service life. It is reported that 40% of the planned wood used in the world every year is vulnerable to decay and damage by insects, with a loss of billions of US dollars. Therefore, the preservative, anti-mildew and anti-insect treatment for wood plays a key role in prolonging the service life of wood products and protecting forests.

Common wood preservatives are divided into fumigant type, tar type, oil-soluble type and water-soluble type. At present, water-soluble preservatives are one of the most widely used preservatives with various types in the world, accounting for 75% of the total amount of preservatives used. Commonly used water-soluble preservatives include chromium-copper-arsenic (CCA), ammoniacal copper quats (ACQ-B, ACQ-D), copper citrate (CC) and copper azole (CopperTriazole, RNCuAz). Although CCA preservatives have a good preservative effect, they contain heavy metals such as chromium and arsenic, which affect human health and ecological environment. It has been banned in developed countries in Europe and America. Currently, ACQ is widely used in the antiseptic industry of wood and bamboo, but the leaching resistance of ACQ is poor, and it is likely to cause certain heavy metal pollution to the environment. Moreover, the surface of wood treated with ACQ presents dark green, affecting its appearance. Therefore, it is very important to select suitable wood preservatives, which should take the damaging factors and application fields of wood into account. In this paper, the research on tannin resins, a natural and environmentally protective wood preservative, is reviewed in order to arouse the mutual encouragement of this industry and realize the development of wood preservatives towards renewable raw materials and environmental protection.

2. Tannins

Vegetable tannins, also known as a plant polyphenol, are a class of polyphenolic compounds widely existing in plants. Its yield is second only to cellulose, lignin and hemicellulose. Tannins can be divided into condensed tannins and hydrolysable tannins according to their chemical structure [1-4], as shown in Figure 1. Condensed tannins account for more than 90% of the total tannins [4,5].

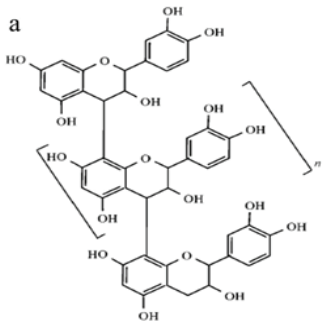

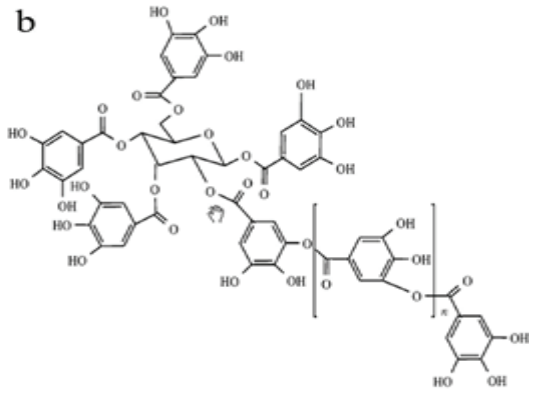

Figure 1. Molecular structure of tannins
a. condensed tannins, **b**. hydrolysable tannins

The chemical properties of condensed and hydrolysable tannins are quite different because of their completely different skeletons. The ester bonds in hydrolysable tannins are easily hydrolyzed by acids, bases or enzymes to produce polyols and phenol carboxylic acids, such as gallotannins. Condensed tannins are condensates of flavanol monomers, which are linked by C-C bonds and are difficult to decompose in aqueous solutions. The tannins contained in the bark of Larix gmelini and Acacia mearnsii are condensed tannins, which are the main raw materials for wood preservatives based on tannin resins. Although condensed tannins differ greatly from hydrolysable tannins, they also have similarities. Their two prominent common properties are complexation with proteins and metal ions and interaction with inorganic salts. The complexation characteristics of Acacia mearnsii tannins and their derivatives with metal ions (Fe^{3+}, Cu^{2+}, Zn^{2+}, Ni^{2+}) from the perspective of coordination chemistry was investigated, which provided a theoretical basis for further development and utilization of tannins [6]. In addition, tannins have certain bacteriostatic and preservative effects, and present significant inhibitory effects on many bacteria, fungi and yeasts.

3. Research review on tannin resins used for wood preservatives

3. 1 Research on antibacterial and preservative properties of tannin resins

Tannins can be directly applied for wood preservatives because of their bacteriostatic and preservative effects. Tannins belong to plant-based preservatives. Although these biological wood preservatives are green and environmentally friendly, their preservative effect is not very ideal. They need to be mixed with boron and metal salts to achieve the optimal preservative effect.

Some approaches [7-8] effectively prevented the growth of microorganisms in wood by soaking with tannin extract and treating with fixative containing c-SAA. In addition, after soaking pine wood with 4% tannin extract, 1% lead sulfate and 1% C9APE9-10, its preservative property was obviously enhanced. The antimicrobial property and its mechanism of Acacia mearnsii tannin, and concluded that Acacia mearnsii tannin had inhibitory effects on Penicillium, poplar anthracnose, canker and decay was explored. The tannins existed in alcohol-benzene extractives and had inhibitory effects on filamentous fungi was pointed out. Some specific substances (such as tannins) contained in wood itself could contribute to natural decay resistance of wood [8], but this preservative effect was weak.

Tannin resin-based wood preservatives were studied abroad in the 1970s. Hart [9] found a large number of antimicrobial components such as tannins and flavonoids in bark extracts. Subsequently, Lotz et al [10] impregnated wood with aqueous solution of vegetable tannin extract, which was treated with fixative or halogen to prevent tannin loss. When the concentration of bromine in the extract was 4-5%, it had better weather resistance, decay resistance and insect resistance [11]. Laks [12] found that condensed tannins could react directly with wood, contributing to the preservative property of wood [13]. Mitchell et al [14]. impregnated wood with 5% ethanol and tannic acid under certain conditions, and then impregnated wood with metal salt solution (40% ferric chloride) twice to resist the damage caused by fungi and termites, so as to achieve wood protection. Peter and Scalbert et al. [15-17] studied condensed tannins and found that the wood treated with additional copper, zinc, boron atoms and ammonia water had better preservative effect, which could meet the European standards for wood preservation. Moreover, Yamaguchi et al. [18,19] revealed that condensed tannin-resorcinol adducts and condensed tannin-catechol adducts could prevent decay caused by fungi. These chemically modified tannins could inhibit the growth of white-rot fungi and brown-rot fungi, and their effect was better when mixed with cuprammonium.

3.2 Research progress on tannins for fixing other preservatives

Boride has bactericidal and insecticidal properties and is harmless to human beings and animals, with good permeability and low price. Therefore, boride has long been recorded as a wood preservative. However, boride is highly water-soluble and easily lost. The research on this aspect focuses on the fixation of boride. Yu Liping [20] treated wood with the mixture of boric acid aqueous solution, gelatin and tannic acid, and found that partial boron was fixed in wood after anti-loss experiment. In addition, tannins reacted with proteins in boric acid solution to form covalent bonds under high temperature, which improved the quality of the gel and reduced the loss of boron. Patachia [21] found that metal salts (zinc, copper, aluminum, iron, etc.) also had a fixing effect on tannins.

Pizzi and Baecker [22] believed that boric acid could be used to induce the self-condensation of flavonoids and tannic acid, so that some boric acid could be stably fixed in the wood network. Thevenon et al. [23] further revealed that tannins binding to proteins could better fixe boric acid or at least significantly delay its leaching. Mazela et al. [24] found that 95% boric acid could be fixed by treating wood with protein preservatives and then tannic acid, and that wood treated with a mixture of boric acid and tannic acid could resist the attack of brown-rot fungi [25]. Tondi et al. found that tannin-hexamethylenetetramine preparation not only was a good wood preservative, but also could reduce the loss of boron. The loss of tannin-boron preparations and the preservative effect of the corresponding products were further investigated. It was found that the loss rate of boron in wood preservation based on tannins was less than 30% after a

complete leaching cycle, while the loss rate of boron preparation without tannins reached 80% [26-29]. Different tree species and tannin sources also affect the fixation of preservatives. Sen et al. [30] found that using lacquer tree tannins to treat pine wood caused a low loss rate of preservatives, and the fixation of preservatives was better after adding with 1% metal saline solution.

4. Prospects

Although plant-based preservatives are a class of green and environmentally friendly biological wood preservatives with great research value and application prospects, there are still some problems to be urgently solved, such as difficult purification, unsustainable preservative effect, high production cost, low industrial productivity and low comprehensive performance. At present, the research on wood preservatives in China still mainly focuses on the application of chemical wood preservatives, but rarely on tannin-based wood preservatives. However, with the increasing awareness of environmental protection worldwide, natural wood preservatives with non-toxicity, harmlessness, good durability, no impact on bonding properties, wide range of raw materials and low price will be paid increasing attention to, and the research on wood preservatives based on tannin resins will also become the focus of future research.

Author Contributions : Xiaojian Zhou contributed to the frame structure building and editing the whole manuscript, Jun Zhang revised the whole manuscript and gave the suggestions, Bin Li and Jinxing Li contributed to the references collection.

Conflict of Interest : No conflict of interest was reported by the authors.

Acknowledgments : This work was supported by the Programs of the Yunnan Provincial Natural Science Foundation (2017FB060), Key research and development plan of the 13th five-year plan (2017YFD0600803) and National Natural Science Foundation of China (NSFC) (31760187). The authors also highly appreciate "Yunnan Provincial Reserve Talents for Middle & Young Academic and Technical Leaders (2019HB026)" and "Ten-thousand Program"-youth talent support program.

References

[1] Dunky M, Pizzi A. Chapter 23–Wood adhesives. In: Adhesion Science & Engineering, 2002. 1039-1103

[2] Tondi G. Tannin-based copolymer resins: Synthesis and characterization by solid state 13C NMR and FT-IR spectroscopy. Polymers 2017; 9: 223.

[3] Pasch H, Pizzi A, Rode K. MALDI-TOF mass spectrometry of polyflavonoid tannins. Polymer 2001; 42: 7531-7539.

[4] Zhou X, Du G. Applications of Tannin Resin Adhesives in the Wood Industry, Tannins-Structural Properties, Biological Properties and Current Knowledge. IntechOpen, 2019. 1-19.

[5] Laks PE, McKaig PA, Hemingway RW. Flavonoid biocides: Wood preservatives based on condensed tannins. Holzforschung-International Journal of the Biology, Chemistry, Physics and Technology of Wood 1988; 42: 299-306.

[6] Bacelo HAM, Santos SCR, Botelho CMS. Tannin-based biosorbents for environmental applications–a review. Chemical Engineering Journal 2016; 303: 575-587.

[7] Jiang XH, Cao JZ. Review on development and utilization of new wood preservatives. China forest products industry 2008; 02: 44-46.

[8] Jiang XH, Cao JZ. Review on development and utilization of new wood preservatives (Continued). China forest products industry 2008; 03: 9-13.

[9] Hart JH, Inhibition of Wood-Rotting Fungi by Stilbenes and Other Polyphenols in Eucaly ptus sideroxylon. Phytopath-ology 1974; 64: 939.

[10] Lotz RW, Hollaway DF. Wood preservation. US: 1988-1282.

[11] Lotz WR. Wood preservation systems including halogenated tannin extracts: U.S. Patent 5,270,083. Google Patents, 1993.

[12] Laks PE. Condensed Tannins as a Source of Novel Biocides. Springer US, 1989.

[13] Zucker WV. Tannins: Does Structure Determine Function? An Ecological Perspective. The American Naturalist 1983; 121: 335-365.

[14] Mitchell R, Sleeter TD. Protecting wood from wood degrading organisms. US: 1980.

[15] Peter E, Laks PA, McKaig HRW. Flavonoid Biocides: Wood Preservatives Based on Condensed Tannins. Holzforschung 1988; 42: 299-306.

[16] Yamaguchi H, Okamura T. Environmental safeguards and wood preservatives. Utilization of tannin-metal complex (in Japanese). Wood Industry (Mokuzai Kougyo) 1995; 50: 155-159.

[17] Scalbert A, Cahill D, Dirol D. A tannin/copper preservation treatment for wood. Holzforschung 2009; 52: 133-138.

[18] Yamaguchi H, Okuda KI. Chemically Modified Tannin and Tannin-Copper Complexes as Wood Preservatives. Holzforschung 1998; 52: 596-602.

[19] Yamaguchi H, Yoshino K, Kido A. Termite resistance and wood-penetrability of chemically modified tannin and tannin-copper complexes as wood preservatives. Journal of Wood Science 2002; 48: 331.

[20] Yu LP, Xia YF, Cheng SW. Methods and suggestions for improving leaching resistanceof boron-based wood preservatives. China wood industry 2012; 02: 29-33.

[21] Patachia S. Biopolymers for wood preservation, biopolymers and Biotech Admixtures for Eco-Efficient Construction Materials. Woodhead Publishing 2016: 305-332.

[22] Pizzi A, Baecker A. A New Boron Fixation Mechanism for Environment Friendly Wood Preservatives. Holzforschung - International Journal of the Biology, Chemistry, Physics and Technology of Wood 1996; 50: 507-510.

[23] Thevenon MF, Pizzi A, Haluk JP. One-step tannin fixation of non-toxic protein borates wood preservatives. European Journal of Wood and Wood Products 1998; 56: 90.

[24] Mazela B, Ratajczak I, Bartkowiak M. Reduction of preservatives leaching from wood by the application of animal proteins Reduction of preservatives leaching from wood by the application of animal proteins. IRG/WP, 2005; 5.

[25] Ratajczak I, Mazela B. The boron fixation to the cellulose, lignin and wood matrix through its reaction with protein.

European Journal of Wood and Wood Products 2007; 65: 231-237.

[26] Tondi G, Wieland S, Lemenager N, et al. Efficacy of tannin in fixing boron in wood. BioResources 2012; 7: 1238-1252.

[27] Thévenon MF, Tondi G, Pizzi A. Friendly wood preservative system based on polymerized tannin resin-boric acid for outdoor applications. Maderas Ciencia Y Tecnologia 2010; 12: 253-257.

[28] Thevenon MF, Tondi G, Pizzi A. High performance tannin resin-boron wood preservatives for outdoor end-uses. European Journal of Wood and Wood Products 2009; 67: 89-93.

[29] Tondi G, Palanti S, Wieland S, et al. Durability of tannin-boron-treated timber. Bioresources 2012; 7: 5138-5151.

[30] Sen S, Tascioglu C, Tirak K. Fixation, leachability, and decay resistance of wood treated with some commercial extracts and wood preservative salts. International Biodeterioration & Biodegradation 2009; 63: 135-141.

Publisher: Viser Technology Pte. Ltd.

URL: www.viserdata.com

Add.:21 Woodlands Close, #08-18,

Primz Bizhub SINGAPORE (737854)